Active Polar suspensions: Stability and Turbulence

A Thesis submitted to

Tata Institute of Fundamental Research, Mumbai, India

for the degree of

Doctor of Philosophy

by

Rayan Chatterjee

Tata Institute of Fundamental Research

TIFR Centre for Interdisciplinary Sciences, Hyderabad

Hyderabad – 500 107, India.

August 2019

DECLARATION

This thesis is a presentation of my original research work. Wherever contributions of others are involved, every effort is made to indicate this clearly, with due reference to the literature, and acknowledgement of collaborative research and discussions.
The work was done under the guidance of Dr. Prasad Perlekar and Professor Sriram Ramaswamy, at the Tata Institute of Fundamental Research, Mumbai.

Name: RAYAN CHATTERJEE
Rayan Chatterjee

[candidate's name and signature]

In my capacity as supervisor of the candidate's thesis, I certify that the above statements are true to the best of my knowledge.

Prasad Perlekar

SRIRAM RAMASWAMY
28 Aug 2019

[guide's name and signature]
Date:

Acknowledgement

I am deeply grateful to my thesis supervisors Dr. Prasad Perlekar and Prof. Sriram Ramaswamy for guiding my work over the last five years. It is a pleasure learning from and working with them. I thank Prof. Mustansir Barma, Prof. Smarajit Karmakar, Dr. Kabir Ramola and Prof. Surajit Sengupta for helpful discussions. My special thanks to Mr. Ananyo Maitra for the fruitful discussions. My sincere thanks to the TCIS office staff for their efficient help over the years. I thank my colleagues in TCIS for making my pastimes interesting. Finally I thank my parents for their constant support and unwavering faith in all my endeavors.

Publications Relevant to this thesis:

1. Rayan Chatterjee, Abhijeet A. Joshi & Prasad Perlekar, Front structure and dynamics in dense colonies of motile bacteria : Role of active turbulence, Phys. Rev. E **94**, 022406 (2016).
2. Rayan Chatterjee, Navdeep Rana, R. Aditi Simha, Prasad Perlekar & Sriram Ramaswamy, Fluid flocks with inertia (arXiv:1907.03492).
3. Rayan Chatterjee, Sriram Ramaswamy & Prasad Perlekar, Topology of defect turbulence in polar active suspensions (in preparation).
4. Navdeep Rana, Rayan Chatterjee, Sriram Ramaswamy & Prasad Perlekar, Turbulence in incompressible polar active fluids (in preparation).

Division of labor

I have done the linear stability analysis described in Chapter 2. In Chapter 3 I have developed the 3D solver for active polar fluid starting from an established Navier-Stokes solver, calibrated it with the linear and non-linear results available in literature, made the observations on defect-turbulence with growing inter-defect distance and the phase-turbulence, and compared the statistics of active turbulence in extensile and contractile swimmer suspensions. In Chapter 4 I have done the full analysis for the turbulent front-speed, the hull fractal dimension, and interpreted the results on the multi-valued nature of the front.

Contents

Chapter 1

Introduction

Active matter is associated with the scientific study of the collective dynamics of self-propelled particles (SPP) - entities which can spontaneously transduce an energy input, usually but not necessarily chemical, into autonomous mechanical motion. All living systems are active matter; popular natural examples are fish-schools, bird-flocks, insect-swarms, bacterial suspensions. As these examples indicate, such systems range in size from micrometers to several hundred metres. The dynamics of the individual particles being self-driven, their collective dynamics is strongly out of equilibrium, and exhibit novel phenomena which run counter to expectations from similar equilibrium systems [1, 2] or even nonequilibrium boundary-driven systems [3, 4, 5]. Some examples of such activity-driven collective phenomena are:

(a) Flocking: the spontaneous ordering of particle velocities with respect to a medium. In particular, the prediction of stable long range order in two dimensions [6, 7, 8] through long-range effects caused by the self-advection of the order-parameter, thus thus evading the fate of the equilibrium 2D XY model (Mermin Wagner theorem).

(b) Giant number fluctutations(GNF): in a region containing N particles on average in the statistically steady state, the standard deviation in the number scales as N^{Δ} where $\Delta > 1/2$ in stark contrast to equilibrium systems where this scaling goes as $\sqrt{N}$. This theoretical conclusion [9, 10] has also been confirmed in experiments on vibrated systems of granular rods [11, 12] and mutant bacterial suspensions [13].

(c) Liquid-gas like phase transition in a one-component system of particles having only repulsive interactions, which is not feasible in a passive system. This phenomena called motility induced phase separation (MIPS) is caused by a tendency of the particles to slow-down in regions of enhanced density. The rich theory behind this phenomena have been described in [14, 15, 16, 17] and also recently reported in simulations [18] and experiments [19].

(d) Mesoscopic turbulence at low Reynolds numbers ($\sim 10^{-1}$) observed in bacterial suspensions [20] and motorized biofilament extracts [21]; which is distinct from traditional fluid-turbulence [3] which occurs at high Reynolds numbers($\sim 10^2$ or more) and the nonequilibrium dynamics is sustained by driving forces coming mainly from the boundaries.

The study of active matter is inspired by the various collective phenomena observed in living systems. As a first step to understand the fundamental governing principles behind these complex dynamics, one writes down simplified theoretical models considering the basic symmetries and conservation laws followed by the original system. The analytical understanding of these minimalistic models gives ideas on the collective properties which are then tested through simulations and experiments on biological systems or their artificial analogues.

This work focuses on active suspensions, or wet active matter, both terms being used synonymously for describing the properties observed in systems of self-propelled motile entities in a bulk fluid, capable of directional motion. Common examples are fish-schools, bacterial suspensions, cell-membrane extracts. The hydrodynamics of active suspensions involves study of the slow variables, whose length and time scales of variation are much larger than those for particle level dynamics. These are [22]:
Coarse-grained active-particle number c defined as

$$c(\boldsymbol{x}, t) = \sum_j \delta(\boldsymbol{x} - \boldsymbol{x}_j(t)), \tag{1.1}$$

the hydrodynamic velocity field $\boldsymbol{u}$ defined as the weighted average of the fluid velocity $\boldsymbol{v}_f$ and the particle velocity $\boldsymbol{v}_p$:

$$\boldsymbol{u}(\boldsymbol{x}, t) = f\boldsymbol{v}_f(\boldsymbol{x}, t) + (1 - f)\boldsymbol{v}_p(\boldsymbol{x}, t), \tag{1.2}$$

and the polar order parameter $\boldsymbol{p}$ which is the instantanous velocity of the particles relative to the fluid :

$$\boldsymbol{p}(\boldsymbol{x}, t) = \boldsymbol{v}_p(\boldsymbol{x}, t) - \boldsymbol{v}_f(\boldsymbol{x}, t). \tag{1.3}$$

Here j denotes particle index in Equation (1.1), the summation being taken over all particles within the coarse-graining volume. f denotes a coarse-grained measure for the number fraction of active particles, and is defined as $f = c_0/\rho$, where c_0 is the mean concentration and ρ is the suspension number density, assumed constant.

In systems where the particles cannot locomote, or there are equal number of particles propagating along opposite directions, the system does not have a macroscopic drift velocity (further discussed in chapter 2 introduction). For such systems the macroscopic order is described in terms of the nematic order tensor $\mathbf{Q}$, defined as

$$\mathbf{Q}(\boldsymbol{x}, t) = \frac{1}{c(\boldsymbol{x}, t)} \sum_i (\hat{\mathrm{n}}\hat{\mathrm{n}} - \frac{\mathbf{I}}{\mathrm{d}})\delta(\mathrm{x} - \mathrm{x_i}(\mathbf{t})) \tag{1.4}$$

where the nematic order parameter $\mathbf{Q}$, unlike the polar order parameter, is fore-aft symmetric, i.e. the equations for $\mathbf{Q}$ remain unchanged under the transformation $\boldsymbol{n} \leftrightarrow -\boldsymbol{n}$. The directionality of the vectorial polar order parameter is implemented in the governing equations by including the $\boldsymbol{p} \leftrightarrow -\boldsymbol{p}$ asymmetric term $\sim \boldsymbol{p} \cdot \nabla \boldsymbol{p}$.

1.1 Governing Equations

1.1.1 Hydrodynamic equations

We begin by recalling for the reader the equations of motion for the hydrodynamic velocity field $\boldsymbol{u}$, the polar order parameter field $\boldsymbol{p}$, and the active particle concentration c, as functions of position r and time t, for bulk active suspensions [9]. Note that $\boldsymbol{p}$ is not the nematic director [23], and not a unit vector: its magnitude measures the degree of polar, i.e., vectorial, order, and $\boldsymbol{p} \to -\boldsymbol{p}$ is not a symmetry unless r and $\boldsymbol{u}$ are reversed as well. At this stage we therefore include for completeness all leading-order polar terms [24, 25, 26, 27]. The equations are:

$$\begin{aligned}
\rho(\partial_t \boldsymbol{u} + \boldsymbol{u}\cdot\nabla\boldsymbol{u}) &= -\nabla P + \mu\nabla^2\boldsymbol{u} + \nabla\cdot(\boldsymbol{\Sigma}^a + \boldsymbol{\Sigma}^r), && (1.5)\\
\partial_t \boldsymbol{p} + (\boldsymbol{u} + v_0\boldsymbol{p})\cdot\nabla\boldsymbol{p} &= \lambda\mathsf{S}\cdot\boldsymbol{p} + \boldsymbol{\Omega}\cdot\boldsymbol{p} + \Gamma\boldsymbol{h} + \ell\nabla^2\boldsymbol{u}, \text{ and} && (1.6)\\
\partial_t c + \nabla\cdot[(\boldsymbol{u} + v_1\boldsymbol{p})c] &= 0. && (1.7)
\end{aligned}$$

Here, the hydrodynamic pressure P enforces incompressibility $\nabla\cdot\boldsymbol{u} = 0$, S and $\boldsymbol{\Omega}$ are the symmetric and the antisymmetric parts of the velocity gradient tensor $\nabla\boldsymbol{u}$,

$$\boldsymbol{\Sigma}^a \equiv \sigma_a(c)\boldsymbol{pp} - \gamma(\nabla\boldsymbol{p} + \nabla\boldsymbol{p}^T) \tag{1.8}$$

is the intrinsic stress associated with swimming activity, where $\sigma_a > (<)0$ for extensile (contractile) swimmers [9, 24] is the familiar force-dipole density. We use it here to describe the flow fields created by force-free motion even when suspension inertia is included. In Equations (1.5)-(1.8), the superscript T denotes matrix transpose, and γ, with units of surface tension and presumably of order σ_0 times an active-particle size, controls the lowest-order *polar* contribution to the active stress. In principle all parameters should be functions of the local concentration c; we have made this dependence explicit in the case of σ_a. We further define the mean strength of active stress

$$\sigma_0 \equiv \sigma(c_0), \tag{1.9}$$

where c_0 is the mean concentration.

$$\boldsymbol{\Sigma}^r = \frac{\lambda+1}{2}\boldsymbol{hp} + \frac{\lambda-1}{2}\boldsymbol{ph} - \ell(\nabla\boldsymbol{h} + \nabla\boldsymbol{h}^T) \tag{1.10}$$

is the reversible thermodynamic stress [28], $\boldsymbol{h} = -\delta F/\delta\boldsymbol{p}$ is the molecular field conjugate to $\boldsymbol{p}$, derived from a free-energy functional

$$F = \int d^3r[(1/4)(\boldsymbol{p}\cdot\boldsymbol{p} - 1)^2 + (K/2)(\nabla\boldsymbol{p})^2 - E\boldsymbol{p}\cdot\nabla c] \tag{1.11}$$

favouring a $\boldsymbol{p}$-field of uniform unit magnitude [29] which we have rescaled to unity in Equation (1.11). A Frank constant [30] K penalizes gradients in $\boldsymbol{p}$, and E promotes alignment of $\boldsymbol{p}$ up or down gradients of c, according to its sign. μ is the shear viscosity of the suspension, and Γ, dimensionally an inverse viscosity and therefore expected to be of order $1/\mu$, is a collective rotational mobility for the relaxation of the polar order parameter field. λ is the conventional nematic flow-alignment parameter [31, 32] and ℓ, with units of length, govern the lowest-order *polar* flow-coupling term [27, 12, 33]. For simplicity of analysis, we will present results for $|\lambda| < 1$ unless otherwise stated. Polarity enters through the speeds v_0 and v_1 with which $\boldsymbol{p}$ advects itself and the concentration respectively, the coefficient γ in the polar part of the stress 1.8, and the polar flow-coupling length-scale ℓ. v_1 will drop out of our analysis as we will ignore the concentration field. To keep the analysis simple, and without any loss of essential physics, we set γ and ℓ to zero. These quantities enter a more detailed analysis through the dimensionless combinations $\mu v_0/\gamma$ and $K/\sigma_0\ell^2$; the present treatment sets these to infinity. Polar effects are then carried locally by v_0 alone. The vector nature of the order parameter will of course also be reflected globally in the nature of the allowed topological defects. Crucially, v_0 and σ_0 are independent quantities in our coarse-grained treatment, a point we will return to in chapter 2 Section 2.3.0.2 (in the subsection on large-q dynamics).

We remind the reader that Equations (1.5) to (1.7) constitute a symmetry-based effective description on length-scales much larger than a fish (as we shall call our self-propelled particles hereafter). The viscosity μ and other parameters are coarse-grained properties of this active suspension which we treat as phenomenological coefficients, not to be confused with the corresponding quantities entering a near-equilibrium hydrodynamic description of the ambient fluid. We do not attempt to estimate their magnitudes, which no doubt receive "eddy" contributions from flows on scales of a few fish. Our approach is applicable even if some interactions such the aligning tendency are partly or wholly behavioural rather than mechanical, as long as they are local in space and time.

1.2 Linear stability of polar active suspensions

Linear stability analysis is used to understand whether the perturbations to a homogeneous uniform state grows or decays in time; the state is called linearly stable (unstable) accordingly as to whether the peturbations decay (grow) in time. The hydrodynamic stability of active suspensions have been initiated in [9] where the authors have shown that, for a spatially unbounded suspension, the uniaxial ordered state when perturbed, spontaneously generates flows which go on to destabilize the nematic order in the viscosity dominated regime. For a polar suspension these perturbations propagate as waves as they amplify. The distinct role of suspension inertia on the hydrodynamic stability of the ordered state in an unbounded system, which has been mostly overlooked, is a central focus of this work. Nevertheless we review here some of the conclusions on linear stability analysis of active suspensions, as has been done for specific flow geometries like thin-films, channels, defect configurations which are pertinent to various biological systems like bacterial biofilms, cytoskeleton where the Reynolds numbers are typically low ($\simeq 10^{-2}$).

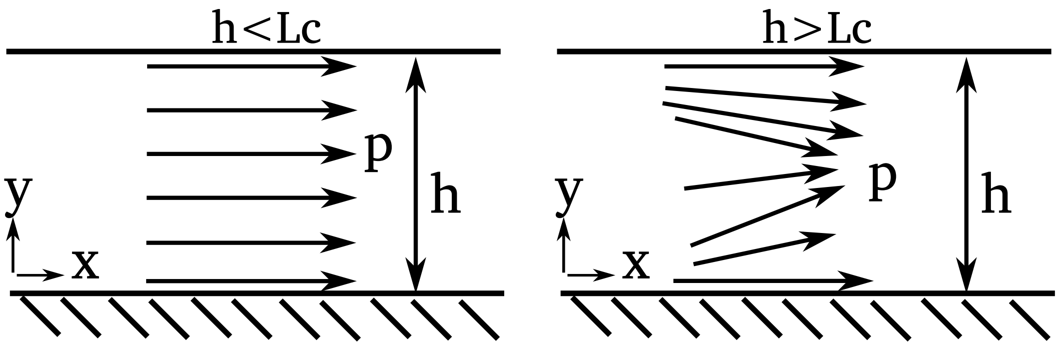

Figure 1.1: Schematic diagram of a laterally unbounded active film with a horizontal free surface when: (a) thickness h is less than L_c, and (b) thickness h exceeds L_c.

1.2.1 Stability of thin films

A model for an active thin films has been studied in [34] for a laterally unbounded geometry with a horizontal non-deformable free surface as shown in Figure 1.1. The mathematical description is the two-dimensional approximation of Equations (1.5) and (1.6), the concentration field being neglected for simplicity. The velocity field is assumed Stokesian, and is thus a balance between the viscous stresses with the active and elastic ones, thus leading to:

$$-P\mathbf{I} + \mu \boldsymbol{S} + \boldsymbol{\Sigma}^a + \boldsymbol{\Sigma}^r = 0 \tag{1.12}$$

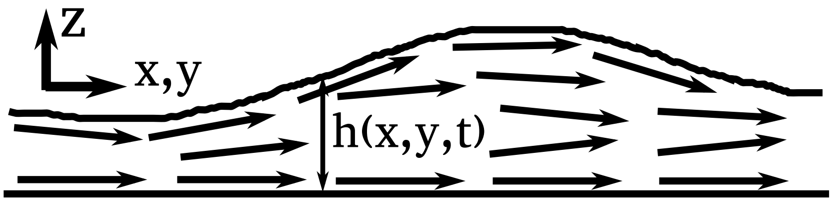

Figure 1.2: Schematic diagram of of an active thin film with a deformable surface.

Now by applying the thin-film approximation one assumes non-zero velocity only along the lateral direction x and negligible lateral gradients compared to wall-normal gradients, i.e. ($\partial_y >> \partial_x$). The velocity gradient tensor, under such assumption, boils down to a scalar $\partial_y v_x$. Further the horizontal undeformed free surface leads to the assumption of zero shear at the free surface, i.e. $\partial_y v_x = 0$ at $y = h$ whete h is the film thickness. Lastly the anchoring boundary condition on the polar order enforces the vertical component to be zero at the substrate and at the free surface. Under such assumptions, the governing dynamics can be represented by a single scalar variable θ which denotes angular distortions to an uniform horizontal profile. This is governed by the following equation:

$$\nabla^2\theta + \theta/L^2 = 0 \tag{1.13}$$

where the characteristic length L is given as:

$$L = \frac{-2\sigma_0(1+\lambda)}{K\left[4\mu/\gamma + (1+\lambda)^2\right]} \tag{1.14}$$

The fundamental solution of Equation (1.13) has the form $\theta = \theta_0 \sin(y/L)$. One can easily observe that real solutions for θ is possible only if the anchoring condition $\theta = 0$ is fulfilled at the substrate $y = 0$(which is obvious) and at the free surface $y = h$. This holds true only when $h = \pi L$. This gives the critical height $L_c = \pi L$ for the stability of the film. For $h < L_c$ there are no real solutions for θ, so the film is stable. But when $h > L_c$ the geometry permits solutions corresponding to spatially distorted solutions for the polar order, which generates destabilizing flows. This is the mechanism for activity induced Freedericksz-like transition which is observed in thin-films as its thickness exceeds a critical value. A more realistic model of the active film which incorporates the local deformations at the free surface in a three-dimensional setting, has been described in [35]. This description is

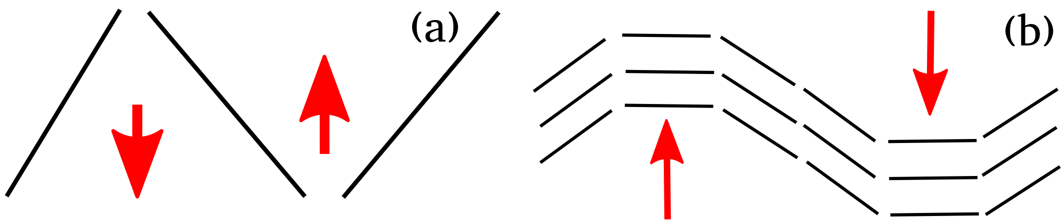

Figure 1.3: Schematic diagram of angular distortions and their generated flows, which are shown by red arrows: (a) unstable splay, and (b) unstable bend.

useful for understanding the mechanism of locomotion in living objects like lamellipodium [36]. Here the local deformations at the free-surface h are related to the velocity components $u_x, \boldsymbol{u}_\perp$ by using the incompressibility criterion [37]:

$$\partial_t h = u_x - \boldsymbol{u}_\perp \cdot \nabla_\perp h \tag{1.15}$$

The Stokes equation for the velocity can be solved exactly , giving the following expression for the velocity field:

$$\boldsymbol{u}_\perp(y) = \frac{hy - y^2/2}{\mu}\left(\gamma \nabla_\perp \nabla_\perp^2 h - \frac{1}{2}\sigma_0 h \partial_x^2 \nabla_\perp h - \boldsymbol{f}_\perp\right) \tag{1.16}$$

where $\boldsymbol{f}_\perp = \sigma_0 \left[(\partial_y \theta + \partial_x c/c_0 + h^{-1}\partial_x h)\hat{\boldsymbol{x}} + \partial_x \theta \hat{\boldsymbol{y}}\right]$ are the active forcing terms. The order parameter field has the uniform horizontal component $\hat{x} + \theta\hat{y}$; the vertical component is calculated by linear interpolation between its value at the free surface and the substrate, thus giving $p_y = (y/h)\partial_x h$. Using these conditions and local mass conservation, the equation for the film height can be obtained. In Fourier space this is

$$\partial_t \delta h_{\boldsymbol{q}} = -\frac{\sigma_0 h_0^2}{3\mu}\left[2h_0 q_x q_y \theta_{\boldsymbol{q}} + h_0 q_x^2 \frac{\delta c_{\boldsymbol{q}}}{c_0} + (1 - \frac{1}{2}h_0^2 q^2) q_x^2 \delta h_{\boldsymbol{q}}\right] - \frac{\gamma h_0^3}{3\mu} q^4 \delta h_{\boldsymbol{q}} \tag{1.17}$$

The four active terms under square brackets are the contributions of: (a) inplane-gradients in splay, (b) active osmosis, proportional to concentration gradients (c) gradients of height, and (d) anisotropic active analogue of surface tension. The last term outside braces is a passive surface tension term, which is always stabilizing for this system. Note that (a) and (c) are caused by splay-distortions lying in different planes (x-y plane for (a) and x-z plane for (c)), and (d) is induced by bend-like distortions of the free-surface. For contractile systems($\sigma_) < 0$) (a), (b) and (c) go unstable and (d) has stabilizing contribution. For extensile systems ($\sigma_0 > 0$) the contributions are exactly opposite. This demonstrates, in essence, one of the central results in the theory of wet active matter: Extensile systems are unstable to bend distortions, whereas contractile systems, are destabilized by splay distortions coupled with concentration currents. This is illustrated in Figure 1.3. Note that these results remain unchanged between nematic and polar suspensions, i.e. the flow directions remain same even when the black lines have arrowheads. In addition, this is the only work which demonstrates that motility, via the self-advection term $\sim v_0$ in Equation (1.6), competes with the destabilizing active stress at leading orders in gradients, thus suppressing the instability. This instabilities cannot be countered by polar active stresses since their contribution is next to leading order in gradients. Furthermore, this stabilization is bypassed in contractile films for purely splay-like distortions along x. An alternative way of having a stable order in suspension of flow aligning particles ($\lambda > 1$), as described by Muhuri et al. [38], is by applying a steady boundary shear. Thampi et al. [39] have demonstrated that deep in the Stokesian regime, where one can effectively ignore the contributions from the pressure and nematic elasicity, there is a direct relation between the active stress and the symmetric component of the velocity gradient tensor, which effectively alters the ordering depending on the sign of active stress and shape of particles (rod-like or disc like). Briefly their calculations are as follows: assuming negligible effects of inertia and pressure, the Stokes equation can be expressed as a balance of active and viscous stresses, so that $\nu S_{ij} \simeq \sigma_0 p_i p_j$, where S is the symmetric component of the velocity gradient tensor, as described before. This gives $S_{ij} = \sigma_0 p_i p_j / \nu$. Using this approximation for S_{ij} in the evolution equation Equation (1.6) for polar order parameter we see that the aligning term $\lambda S_{ij} p_j \simeq \lambda \sigma_0 |\boldsymbol{p}|^2 \boldsymbol{p}$, which alters the magnitude of the uniform polar order. Thus, depending on the relative magnitudes of σ_0 and λ one might expect a disordered state or a polar ordered state with enhanced magnitude of the polar order.

1.2.2 Stability of defect configurations

Defects are an outcome of the complex self-organization processes as observed in experiments on biological systems [21, 41]. This has motivated the study of the

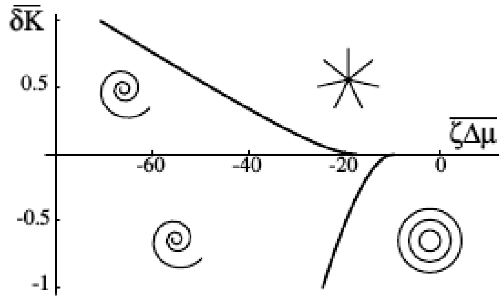

Figure 1.4: Schematic diagram of the various stable defect configurations in a polar active suspension (Kruse et al. [40]).

linear stability of the various integral defect configurations in the hydrodynamic description [40]. The phase diagram is shown in Figure 1.4, where the horizontal and vertical axis denote active stress and the relative stiffness of splay vs bend distortions. One observes that rotating spirals are the only stable configuration below a certain critical value of the active stress. For active stress values above this critical limit, asters are the stable configuration when the bend stiffness is higher than the splay stiffness, and vortices when the splay stiffness is relatively high.

In chapter 3 of this thesis we re-explore the system of Equations (1.5), (1.6) and (1.7) in the three dimensional unbounded setup, with an exhaustive analysis of all leading order polar terms and destabilizing contributions. Here we show that the inertial effects of motility has an intrinsic stabilizing effect on the polar order in a spatially unbounded system. We present a complete stability diagram for polar active suspensions. We also highlight the distinct roles of three-dimensional perturbations in the destabilization of extensile systems, a phenomenon which provides a comprehensive analytical explanation for the numerical observations in [42]. Here we also study the hydrodynamic stability of incompressible polar active suspensions (i.e. in which the solute concentration is fixed and hence the polar order parameter is divergence-free). The order-disorder phenomena in such systems has been studied in the dry limit [43, 44, 45], but, to the best of our knowledge, the hydrodynamics of the polar ordered state in the wet system has not been looked at. We find that the incompressibility constraint rules out the presence of pure splay distortions along the ordering axis; as a result, contractile suspensions for which these are the principal instability modes, are always linearly stable. We also highlight the consequences on the destabilization of two vs three dimensional extensile systems. In the next section we review the key results on the turbulence-like nonequilibrium steady states which is obtained through simulations of the linearly unstable configurations, and connect these understandings with similar features observed in experiments on biological systems.

1.3 Turbulence in polar active suspensions

The current state of the art on active turbulence is mostly focused on exploring the structures observed in bacterial suspensions or cytoskeletal extracts. These systems are mostly viscosity dominated (Re $<<$ 1), and can be studied conveniently in a two-dimensional setting. The current literature on active turbulence is thus focused almost entirely on two-dimensional apolar systems in the viscosity-dominated regime. We therefore emphasize to the reader that our conclusions on the roles of polarity and suspension inertia, and their manifestation in the statistically steady states of active turbulence are a fundamentally new addition to the field.

1.3.1 Numerical studies on turbulence in active nematics

The onset and steady state of turbulence in active nematic suspensions have been explored in [46, 47, 48]. The saturation of instabilities leading to turbulence in active nematic suspensions take place via the following stages: Initially the dominant disturbance amplitudes exhibit spatio-temporal growth.In accordance to the linear-stability picture, one observes growth of bend distortions in extensile systems and splay distortions in contractile systems. This continues till the formation of walls - regions of sharp angular distortions of the order parameter. These walls then release elastic strain energy by the formation of oppositely charged defect-pairs. For apolar systems these defects carry half-integer charges, whereas for polar systems they are of integral charge (we will further explain this in brief later in this chapter and in detail in chapter 3 while discussing defect turbulence). For an apolar system the +1/2 defect has a radial asymmetry whereas the -1/2 defect doesn't. Thus the +1/2 defect is intrinsically motile whereas the -1/2 defect is fairly static, and moves only because of advections by the velocity. Oppositely charged defects originating from different walls then annihilate in pairs, and the fairly ordered regions again spontaneously undergo distortions and release defect pairs. The turbulence is maintained as a result of this dynamic balance between the creation and annihilation of defects. The wall-spacing can be roughly estimated by the characteristic length scale $\ell_K \simeq \sqrt{K/\sigma_0}$, which is the ratio between the stabilizing nematic elasticity to the destabilizing active force; its significance is discussed in a greater detail in chapters 2 and 3. This length scale is also seen to be a good estimate for the inter-defect spacing [47, 49, 50]. The number of defects in the steady state n in both extensile and contractile systems has been seen to scale linearly with activity as [49]. The rate of creation and annihilation of defects follows a quadratic scaling with the activity strength. The same work has also reported the kinematics of the defects, treating them as Brownian particles, and shown that the root-mean-square displacement Δ of the defects indeed scales with time as $\Delta \sim \sqrt{t}$, and the mean free path $\Lambda \sim \sqrt{L^2/n}$ which scales with activity as $\Lambda \sim \sigma_0^{-1/2}$, n being the number of defects and L is the simulation box length. The dependence of the spatial correlation functions for the velocity and order parameter have been discussed in [47, 48], where it has been observed that the scaled correlation length is seen to remain almost independent of the active stress, but is seen to diverge as the elastic constant K is increased. They follow collapse on scaling the spatial distance with the defect number, which the authors explain by the fact that the velocity correlation length is strongly determined by the defect density, which is again dictated by the elastic constant K but not the active stress.

An alternate perspective to the onset of turbulence in apolar active systems in a channel have been described in [51], where it is shown that the transition to turbulence in apolar active systems belongs to the universality class of directed percolation. The authors define a turbulence fraction, which is the height averaged enstrophy (i.e. rotational kinetic energy), as a function of an activity number A,

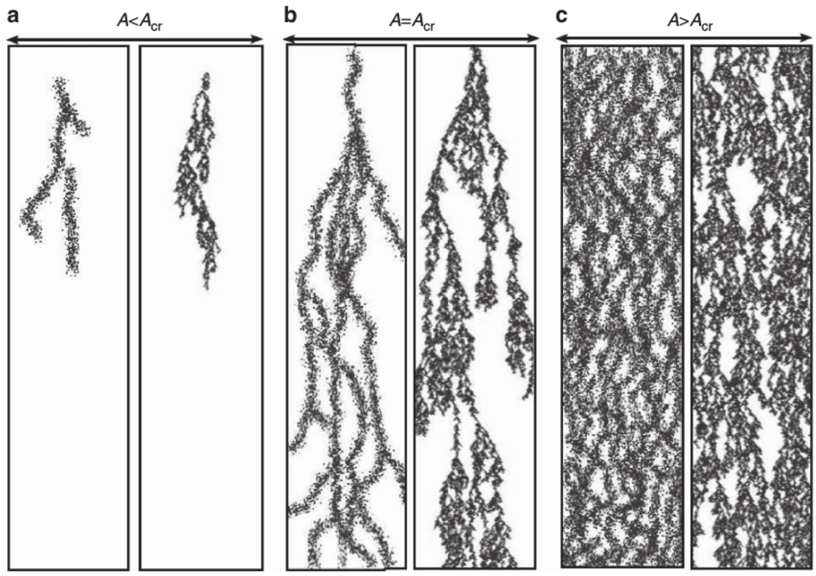

Figure 1.5: Temporal evolution of turbulence fraction in active suspension vs. number of active sites obtained from simulations on Domany-Kinzel model of directed percolation (Doostmohammadi et al.) for (a) below critcality, (b) at criticality, and (c) above criticality. The turbulence fractions are showed in left columns, whereas the right columns show the simulations from Domany Kinzel model.

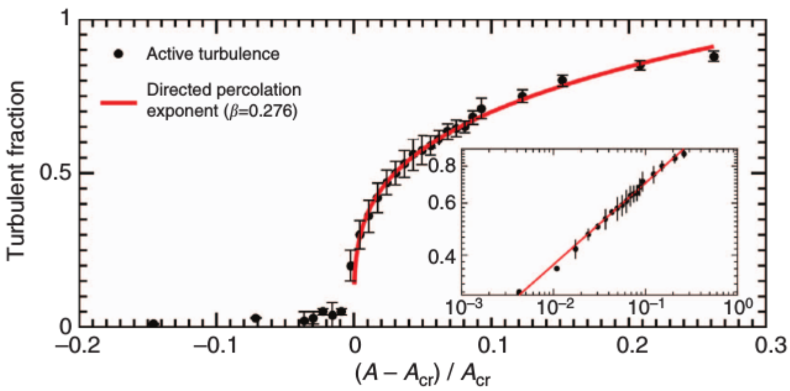

Figure 1.6: Critical behavior of active suspension vs. directed percolation(Doostmohammadi et al.). Black dots indicate turbulence fraction, and red line indicates directed percolation critical coefficient ($\beta = 0.276$).

which is taken the ratio between the channel height and the characteristic length $\ell_K \sim \sqrt{K/\sigma_0}$. Quite obviously the activity number A is the critical parameter for the active system, because it transitions from a stable state of an array of vortices to an unsteady chaotic state, due to the instability mechanism described in [34] (also discussed here above). The onset of the turbulence fraction from near-zero values to non-zero values near the critical value of the activity parameter is compared with the simulations on Domany-Kinzel cellular automata model for directed percolation, where the critical parameter is the transition probability P_c (same for backward and forward), on crossing which, the system transitions from a stable absorbing phase of entirely inactive states to one in which the stationary density of active sites is non-zero. The comparison of the temporal evolution of the two systems is shown in Figure 1.5. Near criticality the exponent for growth of the turbulence fraction in the active suspension shows a close match with the directed percolation model, as illustrated in Figure 1.6, thus confirming the claim.

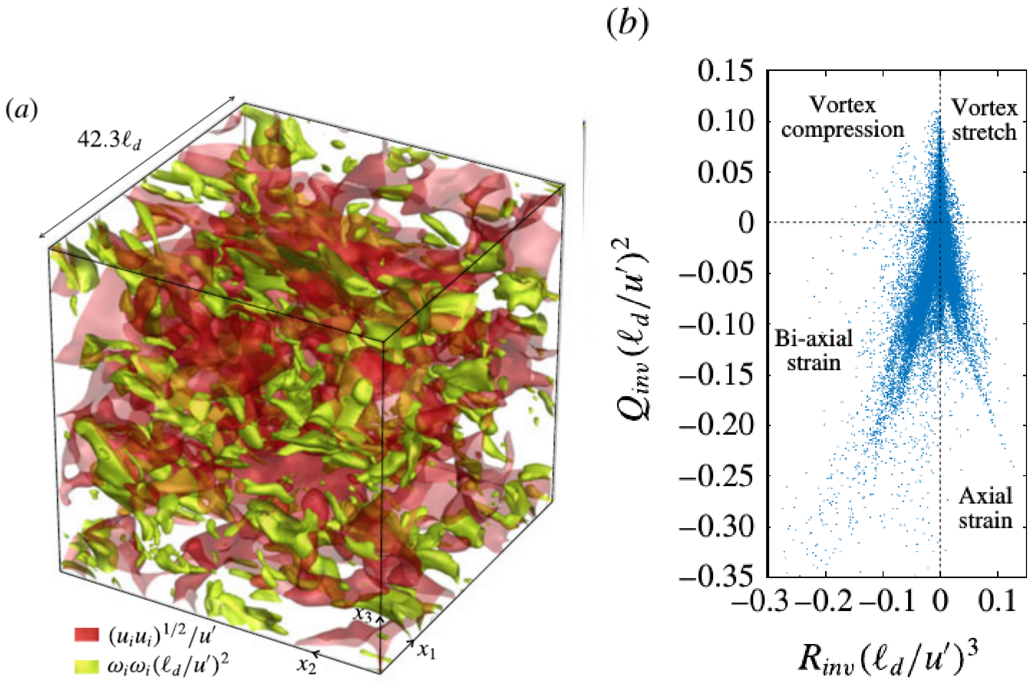

Figure 1.7: Simulations on 3D turbulence in active nematics(Urzay et al.)(a) Snapshot of isocontours of magnitudes of velocity (red) and vorticity (green),(b)Joint PDF for the invariants of the velocity gradient.

The turbulence in apolar systems in a three-dimensional unbounded setting is studied by Urzay et al. [52]. Figure 1.7 show a sample snapshot of the vorticity field and the joint probability distribution of the invariants of the velocity gradient. They observe that the distribution function is skewed mostly towards the bottom-left, indicating biaxially strained (sheet-like) structures, which can also be observed in the isocontours of the velocity magnitude. This, as they explain, is due to the stresslet-kind of flow generated by the individual extensile swimmers. The K.E. and enstrophy spectra for the velocity and KE spectra for the director fields are all seen to peak near the wave-number corresponding to the length-scale $\ell \sim \sqrt{K/\sigma_0}$. Following the peak the decay rate towards the higher wavenumbers follows the power-law $\sim q^{-4}$, which is steeper than the traditional Reynolds-number driven turbulence, where the power law is $\sim q^{-5/3}$, from which the authors conclude that the energy content of the smaller scales in active turbulence is lesser than that in conventional fluid-turbulence.

Shendruk et al. [42] have numerically explored the distinct role of three-dimensional twist perturbations and disinclination loops in the turbulence in extensile active nematic suspensions. Their simulation setup is a laterally unconfined channel with adjustable distance between top and bottom walls. The activity number A is the ratio of the channel thickness H to the characteristic length ℓ_K as defined before. They define a disinclination angle α as a measure of the three dimensionality of the distortions, its value being zero for two-dimensional distortions (pure splay/bend), and is equal to $\pi/2$ for a three-dimensional distortion (twist). Their results show that as the activity number is increased by increasing H, the turbulence crosses over from a two-dimensional to three-dimentional configuration, the indications of three-dimensionality are the onset of non-zero values of the disinclination angle α and the total amount of twist-distortions, both of which are seen to be strongly related. Further, the disinclination angle α is also seen to be constrained to near-zero values (indicating two-dimensionality) on increasing the relative stiffness of the twist distortions over bend and splay distortions in the free-energy functional of the order parameter. All these results go on to establish the special role of twist distortions in sustaining the three-dimensionality of active turbulence.

1.3.2 Numerical studies on turbulence in active polar suspensions

The fore-aft asymmetry of the order parameter causes propagating disturbance waves in polar active suspensions [9]. It is thus interesting to investigate its role in the turbulence, right from the onset. This is essentially the guiding motivation behind most of the the studies on turbulence in polar active suspensions. We now discuss the current state of the art. The coupled dynamics of advection of concentration fluctuations by flows generated by local splay distortions in contractile polar active films has been investigated in [53] in the stokesian limit. The polarity is imposed mainly via the polar active stress term as demonstrated in Equation (1.8).They observe that the transition to spontaneous flow is accompanied by the formation of concentration bands, sharp gradients in concentation across the film, which is generated by the fore-aft asymmetric nature of the polar active stresses. With futher increase in the magnitude of polar stress, the bands start to oscillate and finally starts driving the system to a multicolored state. In a subsequent work [54] the authors have investigated the dynamics of the polar active system in a two-dimensionally unbounded domain. The control parameter here is the coefficient σ_0 of the apolar stress. For extensile system, they observe, gradually upon increasing σ_0, that there are travelling bend-waves, which gradually transition into two oscillating vortices and finally a turbulent-like chaotic state. For the contractile system, the initial destabilization occurs via the formation of splay waves. Further, in the extensile case the fluctuations in concentation and the polar order component along the initial ordering direction are seen to be orders of magnitude smaller than the transverse components. They support their finding on the wave-speed by harmonic-balance analysis, which is, in essence, same as the linear-stability analysis for calculating the frequency and growth rate of perturbation signals. Elgeti et al. [55] have investigated the role of the nematic aligning parameter λ and the relative role of bend and splay stiffness on the structure of the defects in the steady state. In accordance with the linear stability calculations of Kruse [40] they find that the stable structures change from asters to rotating spirals as the value of the active stress decreases below a critical value, and the asters continue to remain stable when the splay stiffness is lower than the bend stiffness, which gives way to stable vortices when the the splay stiffness is higher than the bend stiffness. Further, for flow tumbling systems ($0 < \lambda < 1$) for which one cannot define a finite angle, they observe transient non-stationary solutions, such as moving asters which transform into other different structures. As the polarity is increased by increasing the coefficient of the self-advection, they observe an enhanced range of parameters for which vortices are the stable structures.

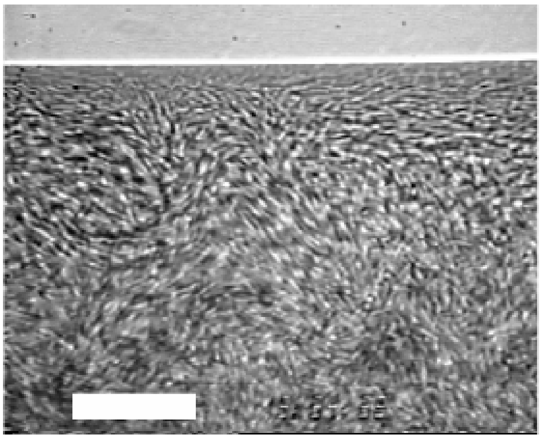

Figure 1.8: Experiment to illustrate large-scale coherent motion in bacteria (Dombrowski et al. [56]).

1.3.3 Experimental observations on active turbulence

The various features of active turbulence, i.e. the locally ordered but globally chaotic pattern consisting of motile vortical structures and defects have also been observed experimentally in a wide variety of experiments. The turbulent-like collective motion in motile bacteria *B. subtilis* has been explored in [56]. In an aqueous suspension of cell-concentration $10^9/cm^3$ the authors report that the bacteria inside a suspension drop first accumulate to form regions of high concentrations by means of chemotaxis/quorum sensing. In the highly concentrated regions the velocity field exhibits coherent vortical structures resembling fluid turbulence, a sample visualization is shown in Figure 1.8. The size of these structures are $\sim 50\mu m$ and their velocities are $\sim 35\mu m/s$, both of which are roughly around 10 times that of that of an individual bacterium. This confirms that the collective motion occurs at scales much larger than that of individual particles, thus

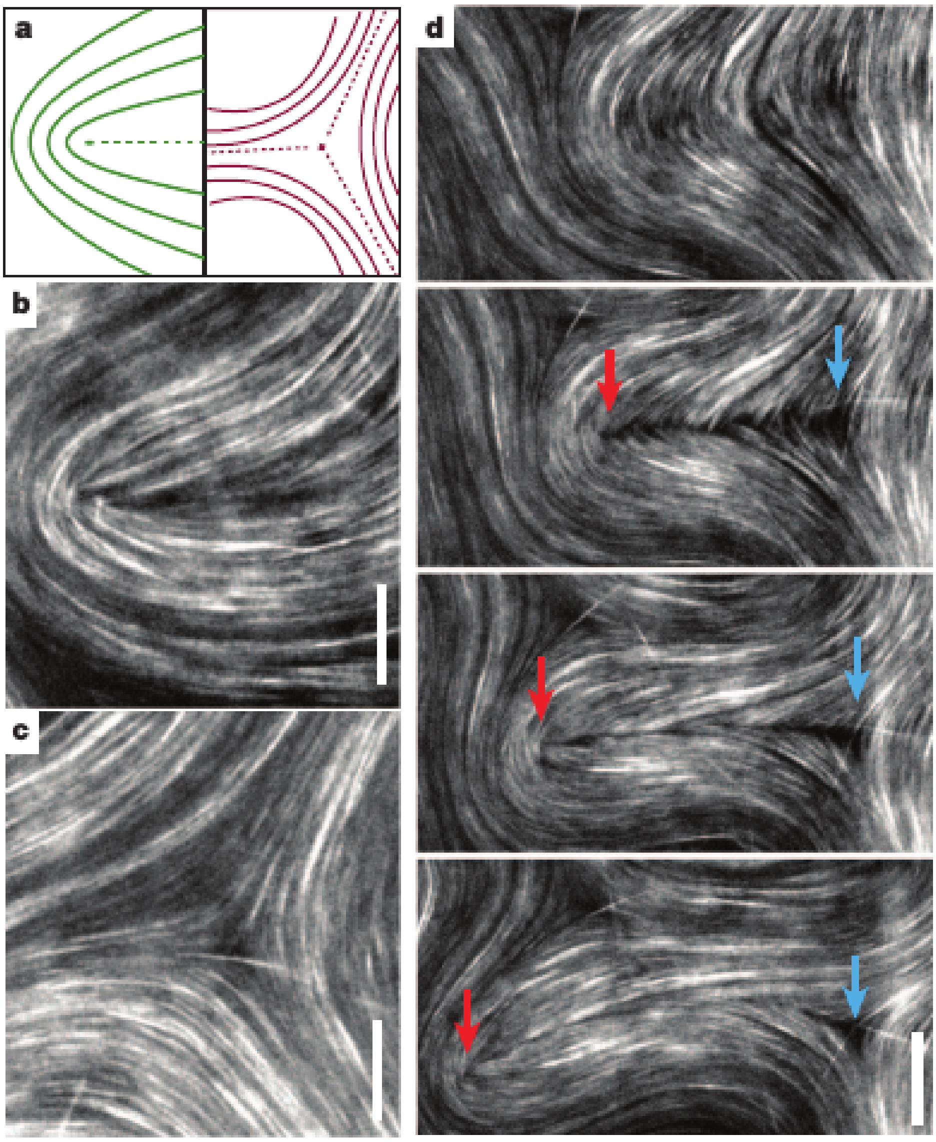

Figure 1.9: +1/2 and -1/2 defects in a suspension of microtubule bundles (Sanchez et al. [21]).

amenable to a hydrodynamic description. Detailed observations on bacterial turbulence together with a simplified mathematical model is proposed in [20], which we will describe in greater detail in chapter 4. The presence of half-integer defects, their generation from distortion walls and creation-annihilation dynamics is observed in [21] in a suspension of microtubule bundles, which suggests the presence of nematic order. A sample defect structure is shown in Figure 1.9. [41] have reported the observation of integral defects in a suspension of unbundled microtubule–motor mixtures, which behave as polar active suspensions. A sample

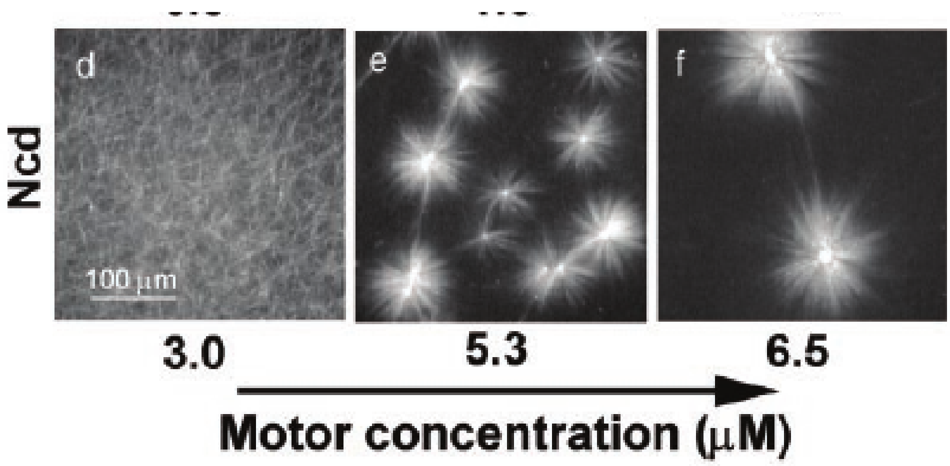

Figure 1.10: Aster defects in a suspension of microtubule bundles (Surrey et al. [41]).

result is shown in Figure 1.10.

In chapter 3 of this thesis we explain our numerical results on the turbulence in polar active suspensions with inertia. We numerically integrate Equations (1.5) and (1.6) in the linearly unstable configurations. We find that the statistically steady state is a hedgehog defect dominated turbulence when activity is dominant over inertia. As the relative strength of inertia over activity is progressively increased, we observe that a new phase turbulence emerges, where the system remains in a fluctuating but aligned state. The onset of the phase turbulence from defect turbulence occurs through a nonequilibrium phase transition, which we characterize using standard tools of statistical mechanics. We finally show that the turbulent kinetic spectrum displays interesting power-law behaviors in the critical region characterizing the phase transition.

1.4 Role of active turbulence on colony spreading

This work is motivated by the observation on the spectacular patterns of colony growth in motile bacteria undergoing swarming motion on a petri dish [57, 58, 59, 60]. A new phase of collective motion in motile bacteria, the ”turbulent” phase, has been recently discovered by experiments [56], and has also been modeled [20] using a simplified version of the Equations (1.5), (1.6) and (1.7). We intend to explore, using numerical simulations, the dynamics of colony growth of motile bacteria in this relatively newly found regime of bacterial turbulence. The dynamics of colony growth in non-motile bacteria is efficiently modeled [61, 62, 63, 64, 65] using the Fisher-Kolmogorov-Petrovsky-Piscounoff (FKPP) equation. We model the colony growth in a turbulent bacterial colony by solving the FKPP equation with an advective coupling to the velocity field obtained by solving the model proposed in [20]. We find that, similar to swarming colonies, here also the population growth front gets crumpled by the turbulent-like collective motion, which we characterize using various statistical tools, namely the hull width and hull-fractal dimension. Most importantly, we find that turbulence always enhances the front-propagation speed; when the turbulence is homogeneous and isotropic, the increase in font speed can be analytically calculated with reasonable accuracy using eddy-diffusivity techniques applied in the analysis of fluid-turbulence.

The remainder of this thesis is organized as follows: In chapter 2 we conduct an exhaustive linear stability analysis of the hydrodynamic equations [9] in order to examine the polar ordered state. We define the non-dimensional number R denoting the relative strength of the inertial effects of self-propulsion vs active forces. In terms of R we define stability thresholds for spontaneous distortion of polar order-ed state in response to external perturbations. In chapter 3 we present our results which we obtain by numerical time-integration of the governing equations. We show the various turbulent-like states and their statistics and illustrate a novel flocking transition as the non-dimensional parameter R crosses one of the critical thresholds defined in our linear stability analysis. In chapter 4 we describe the effects of turbulent-like collective motion in motile bacteria on the dynamics of colony growth. We explain two models which are relevant two physically relevant systems. Using numerical calculations and tools from turbulent modeling techniques we show that, in one of these systems, where the collective motion is homogeneous and isotropic, the smaller scales of turbulent motion effectively act like a diffusive stirring to the colony propagation front. We also explain the interesting similarities/differences in the statistical properties of the front structure for these two systems. In chapter 5 we summarize our essential conclusions and discuss the relevant directions for further studies.

Bibliography

[1] P. M. Chaikin and T. C. Lubensky, *Principles of Condensed Matter Physics* (Cambridge University Press, Cambridge, 1995).

[2] N. Goldenfeld, *Lectures on phase transitions and the renormalization group* (Perseus Books Publishing, L. L. C., NY, 1992).

[3] U. Frisch, *Turbulence: The Legacy of A. N. Kolmogorov* (Cambridge University Press, Cambridge, 1995).

[4] P. G. Drazin and W. H. Reid, *Hydrodynamic Stability*, *Cambridge Mathematical Library*, 2 ed. (Cambridge University Press, Cambridge, 2004).

[5] G. F. Mazenko, *Nonequilibrium Statistical Mechanics* (Wiley-VCH Verlag GmbH and Co. KGaA, Weinheim, 2006).

[6] T. Vicsek *et al.*, Phys. Rev. Lett. **75**, 1226 (1995).

[7] J. Toner and Y. Tu, Phys. Rev. Lett. **75**, 4326 (1995).

[8] J. Toner, Y. Tu, and S. Ramaswamy, Ann. Physics **318**, 170 (2005).

[9] R. A. Simha and S. Ramaswamy, Phys. Rev. Lett. **89**, 058101 (2002).

[10] S. Ramaswamy, R. A. Simha, and J. Toner, Europhys. Lett. **62**, 196 (2003).

[11] V. Narayan, S. Ramaswamy, and N. M. Menon, Science **317 5834**, 105 (2007).

[12] N. Kumar, H. Soni, S. Ramaswamy, and A. Sood, Nat. Commun. **5**, 4688 (2014).

[13] D. Nishiguchi, K. H. Nagai, H. Chaté, and M. Sano, Phys. Rev. E **95**, 020601 (2017).

[14] J. Tailleur and M. E Cates, Physical review letters **100**, 218103 (2008).

[15] Y. Fily and M. C. Marchetti, Phys. Rev. Lett. **108**, 235702 (2012).

[16] M. J. Schnitzer, Phys. Rev. E **48**, 2553 (1993).

[17] M. E. Cates and J. Tailleur, Annual Review of Condensed Matter Physics **6**, 219 (2015).

[18] J. Schwarz-Linek *et al.*, Proceedings of the National Academy of Sciences **109**, 4052 (2012).

[19] A. Suma, G. Gonnella, D. Marenduzzo, and E. Orlandini, EPL (Europhysics Letters) **108**, 56004 (2014).

[20] H. H. Wensink *et al.*, Proc. Natl. Acad. Sci. U. S. A. **109**, 14308 (2012).

[21] T. Sanchez *et al.*, Nature **491**, 431–434 (2012).

[22] R. A. Simha, *PhD Thesis* (Department of Physics, IISc Bangalore, 2002).

[23] P. de Gennes and J. Prost, *The Physics of Liquid Crystals*, *International series of monographs on physics* (Clarendon Press, Oxford, 1993).

[24] M. C. Marchetti *et al.*, Rev. Mod. Phys. **85**, 1143 (2013).

[25] W. Kung, M. Cristina Marchetti, and K. Saunders, Phys. Rev. E **73**, 031708 (2006).

[26] M. C. Marchetti and T. B. Liverpool, in *Cell Motility*, edited by P. Lenz (Springer-Verlag, Berlin, 2007).

[27] A. Maitra *et al.*, arXiv:1901.01069 .

[28] K. Kruse *et al.*, Eur. Phys. J. E **16**, 5–16 (2005).

[29] We assume concentrations are high enough that F globally favours a nonzero magnitude for $\boldsymbol{p}$. We therefore ignore c-dependence in the polynomial part of F.

[30] F. C. Frank, Discuss. Faraday Soc. **25**, 19 (1958).

[31] D. Forster, Phys. Rev. Lett. **32**, 1161 (1974).

[32] H. Stark and T. C. Lubensky, Phys. Rev. E **67**, 061709 (2003).

[33] M. C. Marchetti, personal communication .

[34] R. Voituriez, J. F. Joanny, and J. Prost, Europhys Lett. **70**, 404 (2005).

[35] S. Sankararaman and S. Ramaswamy, Phys. Rev. Lett. **102**, 118107 (2009).

[36] J.F. Joanny, F. Jülicher, and J. Prost, Phys. Rev. Lett. **90**, 168102 (2003).

[37] H. Stone, Chemical Engineering Science **60**, 4838 (2005).

[38] S. Muhuri, M. Rao, and S. Ramaswamy, Europhysics Letters (EPL) **78**, 48002 (2007).

[39] S. P. Thampi, A. Doostmohammadi, R. Golestanian, and J. M. Yeomans, EPL (Europhysics Letters) **112**, 28004 (2015).

[40] K. Kruse *et al.*, Phys. Rev. Lett. **92**, 078101 (2004).

[41] T. Surrey, F. Nedelec, S. Leibler, and E. Karsenti, Science **292**, 1167 (2001).

[42] T. N. Shendruk, K. Thijssen, J. M. Yeomans, and A. Doostmohammadi, Phys. Rev. E **98**, 010601 (2018).

[43] L. Chen, J. Toner, and C. F. Lee, New Journal of Physics **17**, 042002 (2015).

[44] L. Chen, C. F. Lee, and J. M. Toner, Nat. Commun. **7**, 12215 (2016).

[45] L. Chen, C. F. Lee, and J. Toner, New Journal of Physics **20**, 113035 (2018).

[46] S. P. Thampi, R. Golestanian, and J. M. Yeomans, Phys. Rev. Lett. **111**, 118101 (2013).

[47] S. P. Thampi, R. Golestanian, and J. M. Yeomans, EPL (Europhysics Letters) **105**, 18001 (2014).

[48] S. P. Thampi, R. Golestanian, and J. M. Yeomans, Phil. Trans. R. Soc. A **372**, 20130366 (2014).

[49] L. Giomi, Phys. Rev. X **5**, 031003 (2015).

[50] L. Giomi *et al.*, Phil. Trans. R. Soc. A **372**, 20130365 (2014).

[51] A. Doostmohammadi, T. N. Shendruk, K. Thijssen, and J. M. Yeomans, Nat. Commun. **8**, 15326 (2016).

[52] J. Urzay, A. Doostmohammadi, and J. Yeomans, J. Fluid Mech. **822**, 762–773 (2017).

[53] L. Giomi, M. C. Marchetti, and T. B. Liverpool, Phys. Rev. Lett. **101**, 198101 (2008).

[54] L. Giomi and M. C. Marchetti, Soft Matter **8**, 129 (2012).

[55] J. Elgeti, M. E. Cates, and D. Marenduzzo, Soft Matter **7**, 3177 (2011).

[56] C. Dombrowski *et al.*, Phys. Rev. Lett. **93**, 098103 (2004).

[57] M. Fauvart *et al.*, Soft Matter **8**, 70 (2012).

[58] D. Kearns, Nat. Rev. Microbiol. **8**, 634 (2010).

[59] A. Czirok, M. Matsushita, and T. Vicsek, Phys. Rev. E **63**, 031915 (2000).

[60] M. Copeland and D. Weibel, Soft Matter **5**, 1174 (2009).

[61] J.-i. Wakita *et al.*, J. Phys. Soc. Jpn. **63**, 1205 (1994).

[62] A. Beer *et al.*, Proc. Nat. Acad. Sci. **106**, 428 (2009).

[63] K. Korolev, M. Avlund, O. Hallatschek, and D. Nelson, Rev. Mod. Phys. **82**, 1691 (2010).

[64] I. Golding, Y. Kozlovsky, I. Cohen, and E. Ben-Jacob, Physica A **260**, 510 (1998).

[65] S. Pigolotti *et al.*, Theoretical Population Biology **84**, 72 (2013).

Chapter 2

Linear stability analysis of polar active suspensions

In this chapter we discuss our findings on how the hydrodynamic stability of a suspension of motile particles capable of directional motion is affected by the suspension inertia and fore-aft asymmetry. We use the governing hydrodynamic equations for the suspension velocity $\boldsymbol{u}$, the polar order of the active particles $\boldsymbol{p}$ and the active particle concentration c, which were first proposed in the Simha-Ramaswamy model of active suspensions [1]. The theory therein also delienates the temporal stability analysis of nematic order (one without fore-aft asymmetry) in the viscosity dominated regime and shows that it is always absolutely unstable for any non-zero activity. This instability has now been established to be the root cause behind the low Reynolds number active turbulence observed in systems like bacterial suspensions and motorized biofilament extracts. In nature, however one also observes many instances where collections of living entities coherently move together in a fluid; fish schools being a common example. The motivation of this chapter is to understand the the physics behind the stability of such systems by exploring the Simha-Ramaswamy model in greater detail, considering the effects of suspension inertia and directional motility of the active particles. Our complete analysis accounts for the dynamics of the velocity, polar order and concentration fields. However we have observed that our main conclusions are not significantly affected by concentration fluctuations for our current range of parameters. In the main section of this chapter therefore we present our results for the two limiting

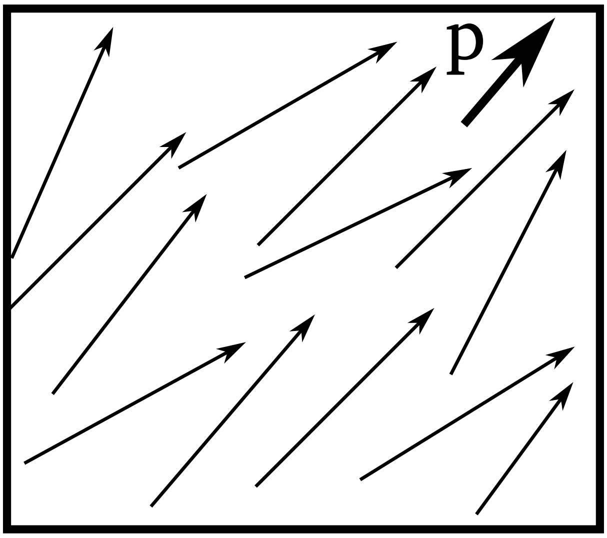

Figure 2.1: Schematic diagram illustrating polar order in a system

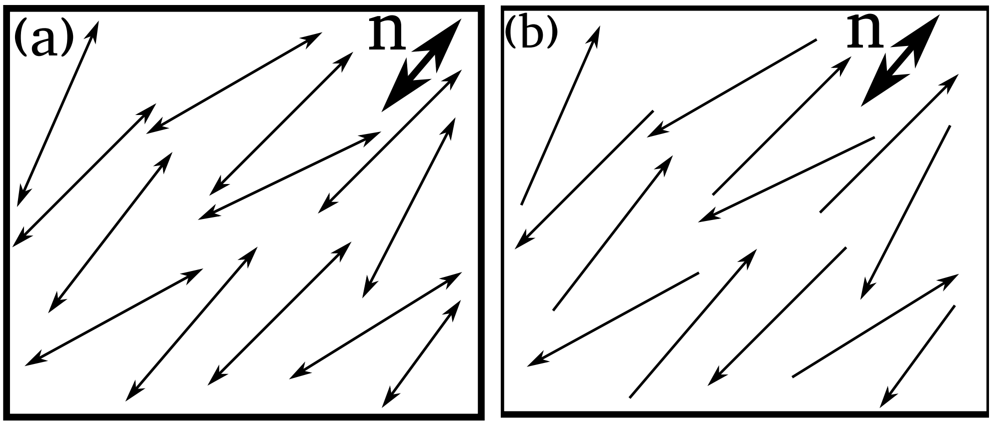

Figure 2.2: Schematic diagram illustrating nematic order in a system (a) where the individual particles are apolar, and (b) where the particles are polar.

situations: the case where concentration fluctuations are rendered fast by the dynamic balance of births and deaths [53], and the incompressible system where the local steric repulsions among the individuals at high particle densities rules out concentration fluctuations; making the polar order divergence-free. In our analysis we explore in detail the following: (a) suspension inertia, proportional to the suspension mass density ρ which would be otherwise ruled out in a purely stokesian suspension where the velocity field is mainly a balance between active and viscous forces; (b) fore-aft asymmetry of the hydrodynamic equations rooted in the directional motility of the swimmers. This manifests itself through the symmetry breaking terms, namely the self advection of the order parameter($\sim \mathrm{p} \cdot \nabla \mathrm{p}$), polar active forces ($\sim \nabla^2 \mathrm{p}$) on the velocity, and the alignment of the polar order parameter with the local flow gradients. Our findings indicate that for extensile systems, both compressible and incompressible, the suspension inertia coupled with directional motility stabilizes angular distortions to the polar order, leading to stable polar flocks when their dominance becomes higher than a critical value which depends on hydrodynamic parameters. Further we also find an unique low-wavenumber diffusive instability only in polar systems. This instability is characterized by traveling perturbation waves which grow in time, and is observed in the regime where the coupled effects of inertia and polarity start competing with activity. We highlight the significance of three dimensional perturbations in the destabilization of extensile systems. We also find that in the limit of a non-conserved concentration field, suspensions of contractile particles are always linearly unstable, whereas for a suspension with incompressible solute concentration they are always linearly stable.

2.1 Introduction

The theory of active matter [2, 3, 4] is the framework of choice for understanding the collective behaviour of motile particles. A familiar example of self-organization in active systems is flocking [5, 6, 7] – *polar* orientational order, with a *vector* order parameter characterizing the degree to which the constituents point and move in a common direction. An illustrative picture is shown in Figure 2.1. The other common type of uniaxial order, well-known from liquid crystals, is *apolar* or *nematic*: spontaneous alignment with an axis but no fore-aft distinction, encoded in a traceless symmetric *tensor* order parameter. Figures 2.2(a) and (b) illustrate the two possible ways in which a system can have nematic order. Similarly, it is natural to consider two ideal dynamical regimes [3]: *wet*, i.e., suspended in unbounded bulk fluid so that Galilean invariance and momentum conservation hold sway, and *dry*, where the active particles are typically in contact with a solid substrate which offers a preferred frame of reference, and whose internal dynamics we approximate by the damping and noise of a momentum sink. Microfluidic experiments on suspensions of active particles define a third "confined wet" [3] domain where motion is limited to one or two dimensions by momentum-absorbing walls but the fluid still exerts a long-range influence through the constraint of incompressibility. Unlike at thermal equilibrium, the steady-state phase diagrams of active systems are sensitive to which of these distinct dynamical ensembles is imposed.

Purely viscous aligned wet active matter in bulk is unstable without threshold [1]. In a finite geometry such as a channel, or on a substrate, the instability manifests itself as an active variant [8] of the Fréedericksz [9, 10] transition, with an onset threshold that scales to zero with increasing channel width or decreasing substrate friction. The instability and the ensuing spontaneous flow [8] and defect proliferation are widely observed [11, 12, 13, 14, 15, 16, 17, 18, 19, 20, 21, 22, 23, 24, 25, 26] and lie at the heart of "bacterial turbulence" [17, 27, 28, 29, 4, 30, 31]. This Stokesian instability can be understood by considering uniaxial active stresses within an *apolar* description [32].

Stable flocks in bulk fluid are, however, widely observed in the form of fish schools, which are far from Stokesian and overwhelmingly polar. Can our local hydrodynamic framework account for their stability? Only a limited early result [1] is available: a parameter domain exists over which the dynamic response of polar flocks in fluid, to first order in small wavenumbers q, is wavelike, that is, oscillatory rather than growing or decaying. Existing studies of self-propulsion at modest but nonzero Reynolds number examine, inter alia, pusher-puller differences in stability and efficiency [33] and hydrodynamic interaction [34, 35], and velocity reversal with frequency [36] in oscillating sphere-dimer swimmers [37, 38]. A phase diagram featuring fluid flocks as active liquid crystals, with inertial effects included, is to our knowledge unavailable.

In this chapter we examine the combined effects of fluid inertia and polarity, i.e., fore-aft asymmetry, and the distinctive characteristics of three dimensional perturbations, on the dynamics of an incompressible active suspension in a state of *vectorial* orientational order, characterized by a self-propelling speed v_0, a scale σ_0 of active stress, shear viscosity μ, a single Frank elastic constant K, and total mass density ρ. In order to highlight intrinsic chaotic properties, we do not add noise to our equations. Our results are most accessibly presented in the limit in which the polar nature of the system is encoded only in self-advection of the polar order parameter, with other polar terms set to zero. We summarise them here.

- For $\sigma_0 > 0$, the "pusher" or "extensile" case of Stokesian active hydrodynamics the dimensionless combination

$$R \equiv \rho v_0^2 / 2\sigma_0, \tag{2.1}$$

  which compares inertial effects of self-propulsion to active stresses, governs the dynamics of a polar fluid flock. Qualitative changes in behaviour as function of R take place across two thresholds, $R = R_1 = 1 + \lambda$, where λ is a flow-coupling parameter, and $R = R_2 \simeq R_1(1+\alpha)^2/4\alpha$ where

$$\alpha = K\rho/\mu^2 \tag{2.2}$$

  $R_2 \geq R_1$ for all α, with equality for $\alpha = 1$. If $\alpha \ll 1$, as is the case for molecular liquid crystals [39], then $R_2 \gg R_1$.

- For $R < R_1$ disturbances at small wavevector q along the ordering direction grow at a rate $q\sqrt{(R_1 - R)\sigma_0/\rho}$, connecting at larger q to the Stokesian instability [1] of active liquid crystals. In the next chapters we show numerically that the result of this instability on long timescales is a turbulent state dominated by hedgehog defects for the compressible system and spiral structures for the incompressible system.

- For $R_1 < R < R_2$ the state of uniform alignment is still linearly unstable, but instabilities grow more slowly at small q, as $q^2(\mu/\rho)[(1-\alpha)(1-R_1/R)^{-1/2} - (1+\alpha)]$. In the next chapter we will show our findings by direct numerical solution that nonlinearities limit the effect of this this $O(q^2)$ instability, and both the compressible and the incompressible system remains in a *phase-turbulent* but *aligned* state. This shows that at $R = R_1$ the system undergoes a nonequilibrium phase transition, driven by inertia, from a statistically isotropic defect-turbulent phase to a noisy but ordered flock.

- For $R > R_2$ the flock outruns the instability: small fluctuations decay at all wavevectors. Note however that in practice R_2 could be very large, as it goes to ∞ both for $\alpha \to 0$ and $\alpha \to \infty$.

- The regime of the $O(q^2)$ instability is completely eliminated in the special limit $\alpha = 1$, which corresponds to equal diffusivities for velocity gradients and director distortions. This limit corresponds to setting the Frank constant K equal to Purcell's [40] critical viscous force μ^2/ρ, inconceivable for equilibrium molecular systems [39] but not ruled out *a priori* for flocks.

- Contractile suspensions, $\sigma_0 < 0$, remain unstable even in presence of inertia ρ and motility v_0; disturbances with q normal to the ordering direction have small-q growth rate $\sim q\sqrt{|\sigma_0|(1+\lambda)/\rho}$. This mode is absent in incompressible suspensions where $\nabla \cdot \boldsymbol{p} = 0$. Thus they are always linearly stable.

- The instability modes for extensile systems are typically three dimensional, provoking twist as well as bend, whereas for contractile systems, the characteristic failure mode is splay, which is two dimensional. Distinct topological structures are observed in the two cases.

2.2 Governing equations and stability analysis of active suspensions

2.2.1 Hydrodynamic equations

We begin by recalling for the reader the equations of motion for the hydrodynamic velocity field $\boldsymbol{u}$, the polar order parameter field $\boldsymbol{p}$, and the active particle concentration c, as functions of position r and time t, for bulk active suspensions [1]. Note that p is not the nematic director [10], and not a unit vector: its magnitude measures the degree of polar, i.e., vectorial, order, and $\boldsymbol{p} \to -\boldsymbol{p}$ is not a symmetry unless r and $\boldsymbol{u}$ are reversed as well. At this stage we therefore include for completeness all leading-order polar terms [3, 41, 42, 43]. The equations are:

$$\rho(\partial_t \boldsymbol{u} + \boldsymbol{u} \cdot \nabla \boldsymbol{u}) = -\nabla P + \mu \nabla^2 \boldsymbol{u} + \nabla \cdot (\boldsymbol{\Sigma}^a + \boldsymbol{\Sigma}^r), \tag{2.3}$$

$$\partial_t \boldsymbol{p} + (\boldsymbol{u} + v_0 \boldsymbol{p}) \cdot \nabla \boldsymbol{p} = \lambda \mathrm{S} \cdot \boldsymbol{p} + \boldsymbol{\Omega} \cdot \boldsymbol{p} + \Gamma \boldsymbol{h} + \ell \nabla^2 \boldsymbol{u}, \text{ and} \tag{2.4}$$

$$\partial_t c + \nabla \cdot [(\boldsymbol{u} + v_1 \boldsymbol{p}) c] = 0. \tag{2.5}$$

Here, the hydrodynamic pressure P enforces incompressibility $\nabla \cdot \boldsymbol{u} = 0$, S and $\boldsymbol{\Omega}$ are the symmetric and the antisymmetric parts of the velocity gradient tensor $\nabla \boldsymbol{u}$,

$$\boldsymbol{\Sigma}^a \equiv \sigma_a(c)\boldsymbol{pp} - \gamma(\nabla \boldsymbol{p} + \nabla \boldsymbol{p}^T) \tag{2.6}$$

is the intrinsic stress associated with swimming activity, where $\sigma_a > (<)0$ for extensile (contractile) swimmers [1, 3] is the familiar force-dipole density. We use it here to describe the flow fields created by force-free motion even when suspension inertia is included. In Eq. (2.3)-Eq. (2.6), the superscript T denotes matrix transpose, and γ, with units of surface tension, control the lowest-order *polar* contribution to the active stress. In principle all parameters should be functions of the local concentration c; we have made this dependence explicit in the case of σ_a. We further define the mean strength of active stress

$$\sigma_0 \equiv \sigma(c_0), \tag{2.7}$$

where c_0 is the mean concentration.

$$\boldsymbol{\Sigma}^r = \frac{\lambda+1}{2}\boldsymbol{hp} + \frac{\lambda-1}{2}\boldsymbol{ph} - \ell(\nabla \boldsymbol{h} + \nabla \boldsymbol{h}^T) \tag{2.8}$$

is the reversible thermodynamic stress [44], $\boldsymbol{h} = -\delta F/\delta \boldsymbol{p}$ is the molecular field conjugate to p, derived from a free-energy functional

$$F = \int d^3r[(1/4)(\boldsymbol{p}\cdot\boldsymbol{p} - 1)^2 + (K/2)(\nabla \boldsymbol{p})^2 - E\boldsymbol{p}\cdot\nabla c] \tag{2.9}$$

favouring a $\boldsymbol{p}$-field of uniform unit magnitude [45] which we have rescaled to unity in Eq. (2.9). A Frank constant [46, 47, 48] K penalizes gradients in $\boldsymbol{p}$, and E promotes alignment of $\boldsymbol{p}$ up or down gradients of c, according to its sign. μ is the shear viscosity of the suspension, and Γ, dimensionally an inverse viscosity and therefore expected to be of order $1/\mu$, is a collective rotational mobility for the relaxation of the polar order parameter field. λ is the conventional nematic flow-alignment parameter [49, 50] and ℓ, with units of length, govern the lowest-order *polar* flow-coupling term [43, 51, 52]. For simplicity of analysis, we will present results for $|\lambda| < 1$ unless otherwise stated. Polarity enters through the speeds v_0 and v_1 with which $\boldsymbol{p}$ advects itself and the concentration respectively, the coefficients γ in the polar part of the stress in Eq. (2.6), and the polar flow-coupling length-scale ℓ. v_1

will drop out of our analysis as we will ignore the concentration field. To keep the analysis simple, and without any loss of essential physics, we set γ and ℓ to zero. These quantities enter a more detailed analysis through the dimensionless combinations $\mu v_0/\gamma$ and $K/\sigma_0\ell^2$ and the corresponding "barred" quantities; the present treatment sets these to infinity. Polar effects are then carried locally by v_0 alone. The vector nature of the order parameter will of course also be reflected globally in the nature of the allowed topological defects. Crucially, v_0 and σ_0 are independent quantities in our coarse-grained treatment, a point we will return to later in the chapter.

We remind the reader that Eqs. (2.3) to (2.5) constitute a symmetry-based effective description on length-scales much larger than a fish (as we shall call our self-propelled particles hereafter). The viscosity μ and other parameters are coarse-grained properties of this active suspension which we treat as phenomenological coefficients, not to be confused with the corresponding quantities entering a near-equilibrium hydrodynamic description of the ambient fluid. We do not attempt to estimate their magnitudes, which no doubt receive "eddy" contributions from flows on scales of a few fish. Our approach is applicable even if some interactions such the aligning tendency are partly or wholly behavioural rather than mechanical, as long as they are local in space and time.

2.2.2 Linear Stability analysis

Defining the ordering direction to be $\hat{\boldsymbol{x}}$ and directions in the yz plane as $\perp$, we have investigated the stability of a uniform ordered flock ($c = c_0, \boldsymbol{u} = \boldsymbol{0}$, and $\boldsymbol{p} = \hat{\mathrm{e}}_x$, which is a stationary solution of Eqs. (2.3)- (2.5) to small perturbations $(\delta\boldsymbol{u}_\perp, \delta\boldsymbol{p}_\perp, \delta c)$, where the presence of only the $\perp$ components is a result of incompressibility and the "fast" nature of p_x. Defining the projector

$$\mathsf{T}_q \equiv \mathsf{I} - \hat{q}\hat{q} \tag{2.10}$$

transverse to $\boldsymbol{q}$ and linearizing Eqs. (2.3), (2.4) and (2.5) about the ordered state we find

$$
\begin{aligned}
\left(\rho\partial_t + \mu q^2\right)\delta\boldsymbol{u}_{\perp\boldsymbol{q}} &= -i\mathbf{T}_{\boldsymbol{q}}\cdot\left[\left(\sigma_0 + \frac{\lambda-1}{2}Kq^2\right)\hat{\boldsymbol{x}}\boldsymbol{q}_\perp + q_x\left(\sigma_0 + \frac{\lambda+1}{2}Kq^2\right)\mathbf{I}\right]\cdot\delta\boldsymbol{p}_{\perp\boldsymbol{q}} \\
&\quad -i\mathbf{T}_{\boldsymbol{q}}\cdot\left(\sigma_0 c_0 q_x\hat{\boldsymbol{x}}\right)\delta c_{\boldsymbol{q}}, \qquad (2.11)\\
\partial_t\delta\boldsymbol{p}_{\perp\boldsymbol{q}} &= +i\left(\frac{\lambda+1}{2}q_x\mathbf{I} - \frac{\lambda-1}{2}\frac{\boldsymbol{q}_\perp\boldsymbol{q}_\perp}{q_x}\right)\cdot\delta\boldsymbol{u}_{\perp\boldsymbol{q}} - \left(iv_0q_x + \Gamma Kq^2\right)\delta\boldsymbol{p}_{\perp\boldsymbol{q}} \\
&\quad +i\boldsymbol{q}_\perp E\delta c_{\boldsymbol{q}}, \qquad (2.12)\\
\left(\partial_t + iv_1q_x\right)\delta c_{\boldsymbol{q}} &= -iv_1c_0\boldsymbol{q}_\perp\cdot\boldsymbol{\delta p}_{\perp\boldsymbol{q}}. \qquad (2.13)
\end{aligned}
$$

The five eigenvalues of the complete system are:

2.2.2.1 Matrix form

The system of Eqs. (2.11), (2.12) and (2.13) can be written as a 5×5 system:

$$AX = 0$$

where

$$
A = \begin{bmatrix}
\omega_\nu & 0 & b_1/\rho & b_2/\rho & b_4 \\
0 & \omega_\nu & b_2/\rho & b_3/\rho & b_5 \\
a_1 & a_2 & \omega_K & 0 & a_4 \\
a_2 & a_3 & 0 & \omega_K & a_5 \\
b_6 & b_7 & 0 & 0 & \omega_c
\end{bmatrix}
$$

$$
X^T = \begin{bmatrix}\delta u_{y\boldsymbol{q}} & \delta u_{z\boldsymbol{q}} & \delta p_{y\boldsymbol{q}} & \delta p_{z\boldsymbol{q}} & \delta c_{\boldsymbol{q}}\end{bmatrix}
$$

$$
\begin{aligned}
\omega_K &= -\omega + v_0 q_x - i\Gamma K q^2, \\
\omega_\nu &= -\omega - i\nu q^2, \\
a_1 &= \left[\frac{\lambda-1}{2}\frac{q_y^2}{q_x} - \frac{\lambda+1}{2} q_x\right], \\
a_2 &= \frac{\lambda-1}{2}\frac{q_y q_z}{q_x}, \\
a_3 &= \left[\frac{\lambda-1}{2}\frac{q_z^2}{q_x} - \frac{\lambda+1}{2} q_x\right], \\
a_4 &= q_y E, a_5 = q_z E, \\
b_1 &= \sigma_0 c_0 q_x \left(1 - \frac{2q_y^2}{q^2}\right) + \lambda K q_x q_y^2 - \frac{(\lambda+1)}{2} K q_x q^2, \\
b_2 &= -2\sigma_0 c_0 q_x q_y q_z / q^2 + \lambda K q_x q_y q_z, \\
b_3 &= \sigma_0 c_0 q_x \left(1 - \frac{2q_z^2}{q^2}\right) + \lambda K q_x q_z^2 - \frac{(\lambda+1)}{2} K q_x q^2, \\
b_4 &= -\sigma_0 q_x^2 q_y / q^2, b_5 = -\sigma_0 q_x^2 q_z / q^2, \\
b_6 &= c_0 v_0 q_y, b_7 = c_0 v_0 q_z.
\end{aligned}
$$

The terms coupling concentration fluctuations with that of velocity and director are :

- The eigen-frequency of concentration fluctuations $\omega_c = -\omega + v_1 q_x$,
- Osmotic terms proportional to the active osmotic pressure E, which are $a_4 = q_y E$ and $a_5 = q_z E$,
- Coupling of the active stress to concentration fluctuations: $b_4 = -\sigma_0 q_x^2 q_y / q^2$, $b_5 = -\sigma_0 q_x^2 q_z / q^2$.
- Concentration fluctuation currents $b_6 = c_0 v_1 q_y$, $b_7 = c_0 v_1 q_z$.

2.2.2.2 Eigenvalues and Eigenvectors

Following points describe the important properties of the eigenvalues and the eigenvectors:

- The matrix A has five eigenvalues and corresponding five eigenvectors. Out of these 5 eigenvectors, three are collinear with $\boldsymbol{q}_\perp$ and represent coupled

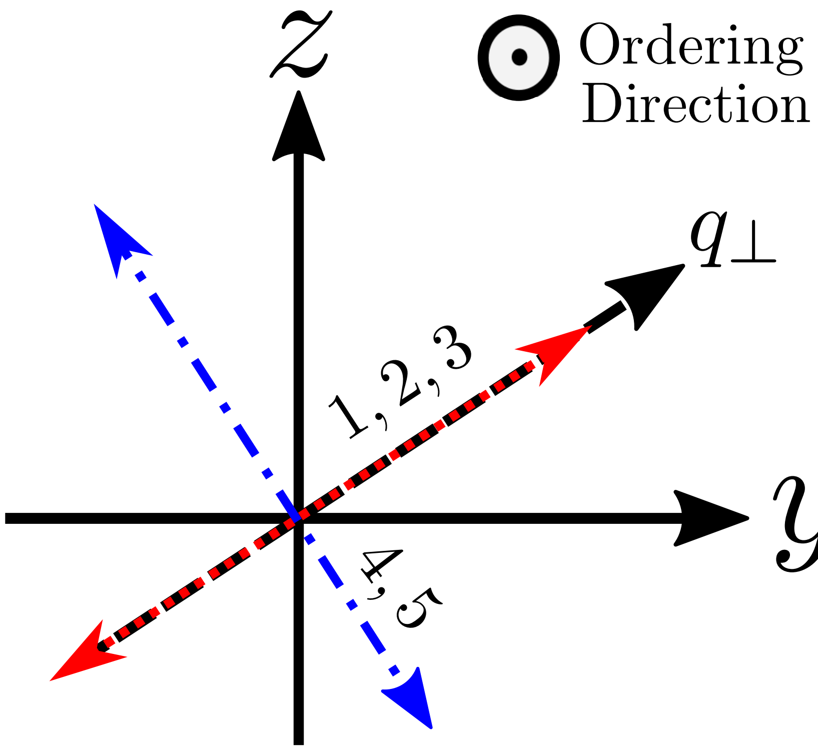

Figure 2.3: Schematic diagram showing the alignment of normal modes for transverse fluctuations in the 3D active suspension. The ordering direction (shown as dot) is perpendicular to the page. The subscript $\perp$ denotes the resultant component in the transverse plane. Thus $q_\perp = [q_y \;\; q_z]$, $N_\perp = [\delta p_{y\boldsymbol{q}} \;\; \delta p_{z\boldsymbol{q}}]$ and $U_\perp = [\delta u_{y\boldsymbol{q}} \;\; \delta u_{z\boldsymbol{q}}]$. The subscripts $1, 2, 3, 4$ denote the eigenvectors corresponding to characteristic frequencies given by Eqs. (2.21) and (2.22) in the main text. Note that the modes $1, 2$ having frequencies given by Eq. (2.21) are collinear to $q_\perp$ and are also present in 2D. On the other hand the modes $3, 4$ having frequencies given by Eq. (2.22) are orthogonal to $q_\perp$ and are present in a three dimensional system only.

splay-bend distortions and concentration fluctuations. Hereafter we call them as modes 1, 2, 3. Their alignment is explained in Figure 2.3, where the numbers 1, 2, 3 indicate that the eigenvectors of the splay-bend modes are aligned along either of the directions marked by the red dashed arrows.

- The two remaining eigenvectors of the system are always perpendicular to $\boldsymbol{q}_\perp$ and represent coupled twist-bend distortions. Their alignment is illustrated in Figure 2.3, where the numbers 4,5 indicate that the eigenvectors lie along either of the directions marked by the blue dash-dot arrows.

- The splay-bend modes 1,2,3 can be present both in two and three dimensional systems, whereas the twist-bend modes 4,5 can be present only in a three dimensional system when the perturbations are three dimensional.

- The eigen-frequencies for the modes 1,2,3 can be obtained by taking an in-plane divergence ($\nabla_\perp \cdot$) of the Eqs. (2.11), (2.12) and solving for the eigenvalues of the coupled system for $\nabla_\perp \cdot \boldsymbol{\delta p}_{\perp \boldsymbol{q}}$, $\nabla_\perp \cdot \boldsymbol{\delta u}_\perp$ and $\delta c_{\boldsymbol{q}}$.

  This leads to the 3×3 matrix equation

$$BY = 0$$

Where

$$B = \begin{bmatrix} \omega_K & b_{12} & b_{13} \\ b_{21} & -\rho\omega_\nu & b_{23} \\ b_{31} & 0 & \omega_c \end{bmatrix}$$

$$\begin{aligned}
b_{12} &= -q(1+\lambda\cos 2\phi)/2\cos\phi, \\
b_{13} &= Eq^2\sin^2\phi, \\
b_{21} &= \sigma_0 c_0 q\cos\phi\cos 2\phi + \lambda K q^3\cos\phi\sin^2\phi - \frac{\lambda+1}{2}Kq^3\cos\phi, \\
b_{23} &= \alpha q^2\sin^2\phi\cos^2\phi, \text{ and} \\
b_{31} &= c_0 v_0.
\end{aligned}$$

$$Y^T = \begin{bmatrix} \nabla_\perp \cdot \boldsymbol{\delta p}_{\perp \boldsymbol{q}} & \nabla_\perp \cdot \boldsymbol{\delta u}_\perp & \delta c_{\boldsymbol{q}} \end{bmatrix}$$

$$
\begin{aligned}
\omega_1 &= \frac{2}{3}v_0q\mathbf{cos}\phi - \frac{i}{3}(\nu+\Gamma K)q^2 + \frac{2^{1/3}F_1}{\left[3(F_2+\sqrt{4F_1^3+F_2^2})^{1/3}\right]} \\
&\quad -\frac{(F_2+\sqrt{4F_1^3+F_2^2})^{1/3}}{(3\times 2^{1/3})}, && (2.14)\\
\omega_2 &= \frac{2}{3}v_0q\mathbf{cos}\phi - \frac{i}{3}(\nu+\Gamma K)q^2 - \frac{(1+i\sqrt{3})F_1}{\left[3\times 2^{2/3}(F_2+\sqrt{4F_1^3+F_2^2})^{1/3}\right]} \\
&\quad +\frac{(1-i\sqrt{3})}{6\times 2^{1/3}}(F_2+\sqrt{4F_1^3+F_2^2})^{1/3}, && (2.15)\\
\omega_3 &= \frac{2}{3}v_0q\mathbf{cos}\phi - \frac{i}{3}(\nu+\Gamma K)q^2 - \frac{(1-i\sqrt{3})F_1}{\left[3\times 2^{2/3}(F_2+\sqrt{4F_1^3+F_2^2})^{1/3}\right]} \\
&\quad +\frac{(1+i\sqrt{3})}{6\times 2^{1/3}}(F_2+\sqrt{4F_1^3+F_2^2})^{1/3}, && (2.16)\\
\omega_4 &= \frac{1}{2}v_0q\cos\phi - i\frac{(\nu+\Gamma K)}{2}q^2 + \frac{F_3^{1/2}}{2}, && (2.17)\\
\omega_5 &= \frac{1}{2}v_0q\cos\phi - i\frac{(\nu+\Gamma K)}{2}q^2 - \frac{F_3^{1/2}}{2} && (2.18)
\end{aligned}
$$

where $\nu = \mu/\rho$, $F_1 = C_1q^2 + C_2q^3 + C_3q^4$, $F_2 = C_4q^3 + C_5q^4 + C_6q^5 + C_7q^6$ and $F_3 = C_8q^2 + C_9q^3 + C_{10}q^4$. The coefficient C_is are:

$$
\begin{aligned}
C_1 &= \frac{1}{2}\left[3\sigma_0c_0\mathbf{cos}2\phi(1+\lambda\mathbf{cos}2\phi) - 6Ec_0v_0\mathbf{sin}^2\phi - 2v_0^2\mathbf{cos}^2\phi\right], C_2 = iv_0(\Gamma K - 2\nu)\mathbf{cos}\phi,\\
C_3 &= \nu^2 + \Gamma K^2 - \nu\Gamma K - \frac{3K}{4}\left[1+\lambda\mathbf{cos}2\phi(2+\lambda\mathbf{cos}2\phi)\right],\\
C_4 &= \frac{1}{2}v_0\mathbf{cos}\phi\left[4v_0^2\mathbf{cos}^2\phi + 9c_0(-4Ev_0\mathbf{sin}^2\phi - 3\sigma_0\mathbf{sin}^2\phi(1+\lambda\mathbf{cos}2\phi) - \sigma_0\mathbf{cos}2\phi(1+\lambda\mathbf{cos}2\phi))\right]\\
C_5 &= \frac{-3i}{4}\left[4v_0^2\mathbf{cos}^2\phi(\Gamma K - 2\nu) + 3c_0(-4Ev_0\mathbf{sin}^2\phi(\Gamma K + 2\nu)\right]\\
&\quad \frac{-3i}{4}\left[\sigma_0(\nu+\Gamma K)(\lambda + 2\mathbf{cos}2\phi + \lambda\mathbf{cos}4\phi))\right],\\
C_6 &= \frac{-3v_0}{4}\mathbf{cos}\phi\left[8\nu^2 - 4\Gamma K^2 - 8\Gamma K\nu + 3K(\lambda^2+5+\lambda(7\mathbf{cos}2\phi + \lambda\mathbf{cos}4\phi))\right],\\
C_7 &= \frac{-i(\nu+\Gamma K)}{8}\left[16\nu^2 + 16\Gamma K^2 - 40\nu\Gamma K - 9K(\lambda^2+2+\lambda(4\mathbf{cos}2\phi+\lambda\mathbf{cos}4\phi))\right],\\
C_8 &= \left[v_0^2 - 2\frac{\sigma_0(1+\lambda)}{\rho}\right]\cos^2\phi,\\
C_9 &= 2iv_0(\nu - \Gamma K)\cos\phi, \text{ and}\\
C_{10} &= -(\nu-\Gamma K)^2 + \frac{K(1+\lambda)^2\cos^2\phi}{\rho}.
\end{aligned}
$$

Here the term $\sim \sigma_0\mathbf{sin}^2\phi(1+\lambda\mathbf{cos}2\phi)$ in the expression for C_4 denotes coupling between the active stress and the concentration fluctuations.

However, we present here the results for the case where the concentration field c is removed from the analysis. This is sufficient for our purposes, because c does not participate significantly in the linear instabilities of relevance, as we now argue. Taking the curl with respect to $\nabla_\perp$ eliminates c from the $\perp$ component of Eq. (2.4). A similar curl removes it from Eq. (2.3) as well, for $\boldsymbol{q}$ purely along or purely normal to $\hat{\boldsymbol{x}}$. Thus, it does not participate in the dynamics of pure bend or twist. Taking the divergence of Eq. (2.3) and Eq. (2.4) with respect to $\nabla_\perp$ reveals that c is present in the linearized dynamics only when $q_x \neq 0$, and is thus unimportant for considerations of pure splay. As a final standpoint we now show that our analysis results remain unaffected even by including concentration fluctuations. From Eqs. (2.14), (2.15), (2.16) we see tha the only modes ω_1, ω_2 and ω_3 have concentration fluctuation dependent terms (with coefficients depending on E and α). These are the two dimensional splay-bend modes. The remaining two modes $\omega_{4,5}$ are the three dimensional twist-bend modes, which do-not couple to concentration fluctuations. See subsection 2.2.2.2 for further details on these modes. In Figures 2.4 we compare the effects of concentration on most unstable splay-bend mode in extensile systems for $R < R_1$(a) and $R > R_1$(b). The dashed line shows the most unstable mode obtained from Eqs. (2.14), (2.15) and (2.16), whereas the dotted line shows the same without concentration dependence(by setting $E, \alpha = 0$). These two dispersion curves are essentially identical. Thus we conclude that the results from the linear stability analysis are qualitatively unaltered upon including the concentration.

The removal of the concentration can be formalized in two ways:

1. By introducing birth and death of particles so that c becomes “fast” [53] and can be eliminated in favour of the slow variables $\boldsymbol{p}_\perp$ and $\boldsymbol{u}_\perp$. From now on we will call these systems number non-conserved.

2. By assuming a constant and uniform concentration, which is a good approximation for dense suspensions having strong local steric repulsive interactions. This sets $\nabla \cdot \boldsymbol{p} = 0$, i.e. the director field is solenoidal. Thus we will call these suspensions ’incompressible’. We will discuss these suspensions in Section 2.4.

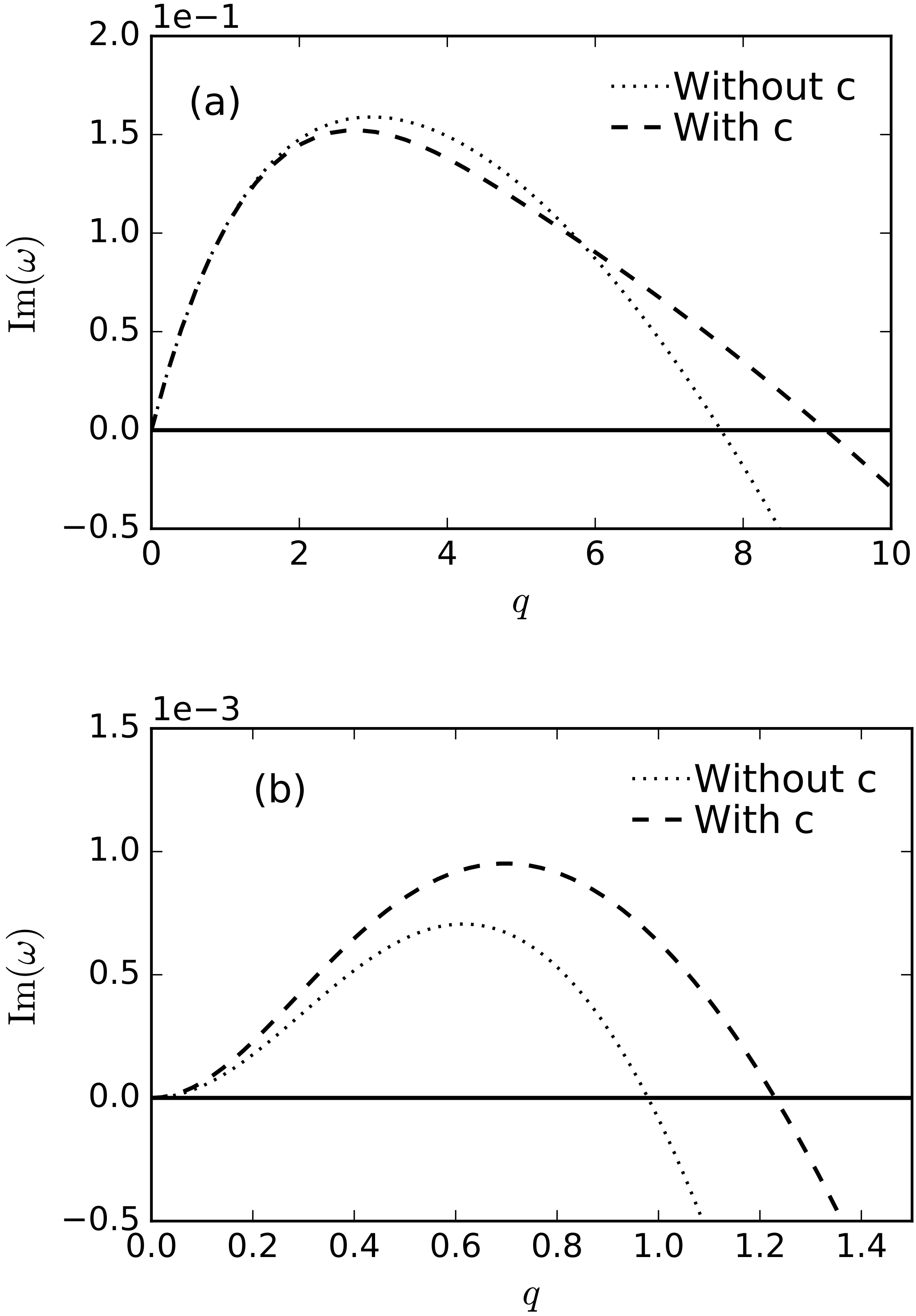

Figure 2.4: Comparison of the splay-bend growth rates with and without explicit concentration dependence for Extensile suspensions: (a) $O(q) : R = 0.1$, and (b) $O(q^2) : R = 5$ regimes. The other parameters are: $\phi = 15°$, $\nu = 10^{-1}$, $\Gamma K = 10^{-3}$, $\lambda = 0.1$, $E = 0.05$.

2.3 Stability analysis of compressible suspensions

On the grounds described above, the governing equations for the compressible polar active suspensions are thus Eqs. (2.3) and (2.4). Because the equations now are better tractable analytically, we perform a detailed analysis on the stability contributions of the various terms. The linearized Eqs. (2.3) and (2.4) are

$$\left(\rho\partial_t + \mu q^2\right)\delta\boldsymbol{u}_{\perp\boldsymbol{q}} = -i\mathsf{T}_{\boldsymbol{q}}\cdot\left[\left(\sigma_0 + \frac{\lambda-1}{2}Kq^2\right)\hat{\boldsymbol{x}}\boldsymbol{q}_\perp + q_x\left(\sigma_0 + \frac{\lambda+1}{2}Kq^2\right)\mathsf{I}\right]\cdot\delta\boldsymbol{p}_{\perp\boldsymbol{q}} \quad (2.19)$$

$$\partial_t\delta\boldsymbol{p}_{\perp\boldsymbol{q}} = +i\left(\frac{\lambda+1}{2}q_x\mathsf{I} - \frac{\lambda-1}{2}\frac{\boldsymbol{q}_\perp\boldsymbol{q}_\perp}{q_x}\right)\cdot\delta\boldsymbol{u}_{\perp\boldsymbol{q}} - \left(iv_0q_x + \Gamma Kq^2\right)\delta\boldsymbol{p}_{\perp\boldsymbol{q}} \quad (2.20)$$

where σ_0 is $\sigma_a(c)$ evaluated at the mean concentration c_0. As in [1], the divergence and curl of Eqs. (2.19) and (2.20) describe respectively the dynamics of splay and twist, with an admixture of bend in each case for $q_x \neq 0$. Defining ϕ to be the angle between the wavevector $\boldsymbol{q}$ and the alignment ($\hat{\boldsymbol{x}}$) direction, the resulting dispersion relations for the frequency ω, valid for all $\boldsymbol{q}$, for modes of the form $e^{i(\boldsymbol{q}\cdot\boldsymbol{x}-\omega t)}$, are

$$\omega = \omega^s_\pm = \frac{1}{2}v_0q\cos\phi - i\frac{\mu_+}{2\rho}q^2 \pm \left(\frac{\sigma_0}{2\rho}\right)^{1/2}\left[A(\phi)q^2 + 2iB(\phi)q^3 + G(\phi)q^4\right]^{1/2} \quad (2.21)$$

for the splay-bend modes and

$$\omega^t_\pm = \frac{1}{2}v_0q\cos\phi - i\frac{\mu_+}{2\rho}q^2 \pm \left(\frac{\sigma_0}{2\rho}\right)^{1/2}\left[A(0)\cos^2\phi q^2 + 2iB(0)\cos\phi q^3 + \bar{G}(\phi)q^4\right]^{1/2} \quad (2.22)$$

for the twist-bend modes. In Eq. (2.21) and Eq. (2.22) we have defined

$$A(\phi) = R\cos^2\phi - \cos 2\phi(1+\lambda\cos 2\phi), \quad (2.23)$$

where

$$R \equiv \rho v_0^2/2\sigma_0, \quad (2.24)$$

$B(\phi) = (v_0\mu_-/\sigma_0)\cos\phi$, $G(\phi) = -(\mu_-^2/2\rho\sigma_0) + (K/2\sigma_0)(1+\lambda\cos 2\phi)^2$, and $\bar{G}(\phi) = -(\mu_-^2/2\rho\sigma_0) + (K/2\sigma_0)(1+\lambda)^2\cos^2\phi$ [54] where

$$\mu_\pm = \mu(1\pm\beta), \quad (2.25)$$

with

$$\beta \equiv \rho\Gamma K/\mu, \quad (2.26)$$

which should be of the same order as α defined in Eq. (2.2) assuming $\Gamma \sim 1/\mu$. For conventional liquid crystals therefore $\beta \ll 1$ as well. Even before examining the asymptotic small- or large-q behaviour, we can read off the effects of competition between the inertia of motility and active stress, through the crucial parameter R defined in Eq. (2.24). From Eq. (2.21) and Eq. (2.22) instabilities driven by active stress clearly operate through a large negative $A(\phi)$, and a sufficiently large R can keep $A(\phi)$ positive. It is also clear that the contribution of R vanishes for pure splay, Eq. (2.21) at $\phi = \pi/2$, so motility cannot stabilize contractile ($\sigma_0 < 0$) flocks in fluid against the splay instability. In the remainder of this section we therefore discuss the stabilizing influence of the inertia of self-propulsion on extensile ($\sigma_0 > 0$) systems. We will return to the contractile case when we discuss active turbulence.

2.3.0.1 Small-q behaviour: the $O(q)$ and $O(q^2)$ instabilities

Let us first examine the small-q behaviour. Expanding Eq. (2.21) and Eq. (2.22) up to order q^2 we then find

$$\begin{aligned}\omega = \omega^s_\pm = \frac{q}{2}\left\{v_0\cos\phi \pm \left[\frac{2\sigma_0}{\rho}A(\phi)\right]^{1/2}\right\}\\ -\frac{i}{2}\frac{\mu}{\rho}q^2\left\{1+\beta m_{\rm p}(1-\beta)\left[\frac{R\cos^2\phi}{A(\phi)}\right]^{1/2}\right\}\end{aligned} \tag{2.27}$$

for the splay-bend modes and

$$\begin{aligned}\omega = \omega^t_\pm = \frac{q}{2}\cos\phi\left\{v_0 \pm \left[\frac{2\sigma_0}{\rho}A(0)\right]^{1/2}\right\}\\ -\frac{i}{2}\frac{\mu}{\rho}q^2\left\{1+\beta m_{\rm p}(1-\beta)\left[\frac{R}{A(0)}\right]^{1/2}\right\}\end{aligned} \tag{2.28}$$

for the twist-bend modes. Here $A(\phi)$ was defined in Eq. (2.23) and $A(0) = A(\phi = 0) = R - (1+\lambda)$. One note of caution: the small-q expansion that led to Eq. (2.28) assumes $v_0 q\cos\phi > q^2\mu/\rho$, which means that it does not apply for $\phi = \pi/2$, i.e., pure twist. It does however hold for any $\phi \in [0, \pi/2)$ but the closer ϕ is to $\pi/2$ the smaller q must be for the result to apply.

Two of our main results now follow. If $R < 1+\lambda$, Eq. (2.28) signals a bend instability with small-q growth rate $\sim q$. This was discussed in the strictly apolar case $v_0 = 0$ in [1], and can be viewed as the small-q extension of the Stokesian

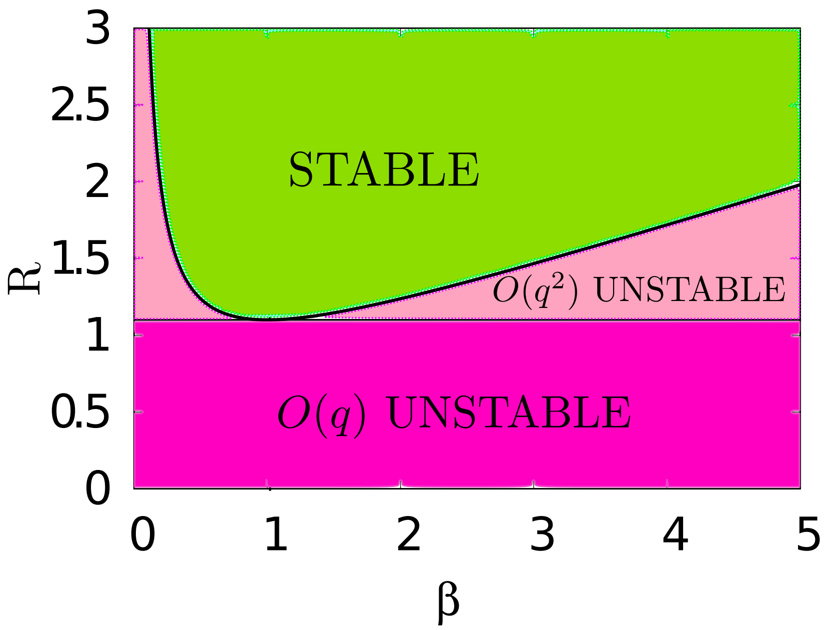

Figure 2.5: $R - \beta$ stability diagram for perturbations of the aligned state. In general, a parameter range where perturbations with small wavenumber q grow at a rate of $O(q^2)$ intervenes between the stable regime and the highly unstable regime of $O(q)$ growth, but is squeezed out of existence if $\beta = 1$, that is, orientation and vorticity have identical diffusivities.

bend instability [1]. However, if $R > 1 + \lambda$, so that the $O(q)$ instability is averted, $0 < 1 - (1 + \lambda)/R < 1$. If R is not too large, this means the coefficient of iq^2 in Eqs. (2.27) and (2.28) is positive, signalling a small-q instability with *diffusive* growth. This $O(q^2)$ instability exists for R between $R_1 = 1 + \lambda$ and

$$R_2 = \frac{\mu_+^2}{\mu_+^2 - \mu_-^2} R_1 = \frac{1 + \lambda}{4\beta}(1 + \beta)^2. \tag{2.29}$$

For $R > R_2$ the flock is linearly stable at all orders in q. If $\beta \ll 1$ as in molecular systems, $R_2 \gg R_1$, and the $O(q^2)$ instability occupies a large range of R. In the $\beta = 0$ limit the uniformly ordered flock is *always* linearly unstable, with small-q growth rate $\sim q$ for $R < 1 + \lambda$ and $\sim q^2$ for $R > 1 + \lambda$. Fig. 2.5 summarizes the small-q behavior.

Note that the $O(q^2)$ instability can be eliminated in the special case $\beta = 1$, i.e., $\mu/\rho = \Gamma K$. Noting that Γ should be roughly $1/\mu$, this condition implies $K = \mu^2/\rho$, an interesting condition that equates a Frank constant (which, recall, has units of force in three dimensions) to Purcell's intrinsic three dimensional force scale

[40] μ^2/ρ for viscous fluids. As we remarked above, β in molecular or colloidal systems is about 10^{-4} [39, 10], so requiring it to be order unity amounts to insisting that the fish have an exceptionally strong aligning interaction. This possibility cannot be ruled out a priori as alignment in living systems is likely to be active and behavioural, not a passive mechanical torque.

2.3.0.2 Large-q dynamics and the Stokesian limit

In order to relate the instabilities discussed above to the well-known Stokesian instability of aligned active suspensions, we define the lengths

$$\ell_v \equiv \mu/v_0\rho \text{ and } \ell_\sigma \equiv \mu/\sqrt{\rho\sigma_0} = R^{1/2}\ell_v \tag{2.30}$$

below which viscosity overwhelms the inertial effects of self-propulsion and

$$\ell_K \equiv \sqrt{K/\sigma_0} \tag{2.31}$$

below which Frank elasticity dominates active stresses. Note that

$$\frac{\ell_K}{\ell_v} = \sqrt{\alpha R} \tag{2.32}$$

can change substantially as R is varied. Expanding Eq. (2.21) and Eq. (2.22) for $q \gg \max(\ell_v^{-1}, \ell_\sigma^{-1})$, we find, to leading order in α and β, that the splay-bend mode that goes unstable at small R has the form

$$\omega^s = -i\frac{\sigma_0}{2\mu}A(\phi) + v_0 q\,\cos\phi - i\left[\Gamma\mu + \frac{1}{4}(1+\lambda\cos 2\phi)^2\right]\frac{K}{\mu}q^2. \tag{2.33}$$

and the corresponding twist-bend mode has frequency

$$\omega^t = -i\frac{\sigma_0}{2\mu}A(0)\cos^2\phi + v_0 q\,\cos\phi - i\left[\Gamma\mu + \frac{1}{4}(1+\lambda)^2\cos^2\phi\right]\frac{K}{\mu}q^2. \tag{2.34}$$

where $A(\phi)$ is as defined in Eq. (2.23).

Note that Eq. (2.33) and Eq. (2.34) are not Stokesian expressions but short-wavelength limits of the linearized dynamics of a polar active suspension *with inertia*, which enters through R. We see in particular that the stability criteria in this large-q regime are identical to those for the $O(q)$ mode at small q. Thus a twist-bend instability, with a growth rate $\sim \sigma_0/\mu$ for $\max(\ell_v^{-1}, \ell_\sigma^{-1}) \ll q \ll \ell_K^{-1}$ takes place if $R < 1+\lambda$. This establishes our claim that the $O(q)$ instability is the small-q extension of the Stokesian instability [1] of active suspensions. The $O(q^2)$ instability that intervenes at small q as R is increased does not reflect itself in the large-q dynamics.

It is important to keep in mind that the active stress σ_0 is a partial description of the mechanics of self-propulsion based on an estimate of the force-dipole concentration, and is not a priori determined by v_0. To take an extreme case, Stokesian swimmers with no force dipole exist, e.g., the pure quadrupole [40, 55]. Assuming a volume fraction of order unity, let us nonetheless try to estimate R for typical swimmers of speed v_0 and size a (although we must remember that this size is notional in our coarse-grained description). For Reynolds number Re small at the scale of the individual organism it is plausible that $\sigma_0 \sim \mu v_0/a$. In that case $R \equiv \rho v_0^2/2\sigma_0 \sim \rho v_0 a/\mu = \text{Re} \ll 1$, so we can replace Eq. (2.33) and Eq. (2.34) by their Stokesian approximations. For high-Re swimmers it is less obvious how to estimate σ_0. If we take it still to be a viscous stress then $R = \text{Re}$ continues to hold, so now R dominates in Eq. (2.33) and Eq. (2.34), or in Eq. (2.21), Eq. (2.22), guaranteeing stability. Even if $\sigma_0 \sim \rho v_0^2$, $R \sim 1$ and it is plausible that the instability is averted [56].

2.3.0.3 Dominance of twist in the three dimensional instability

A noteworthy feature, to our knowledge not discussed in the literature, emerges in our three dimensional analysis: there are two families of bend instability – mixed with splay as in Eq. (2.27) and Eq. (2.33) and twist as in Eq. (2.28) and Eq. (2.34). Interpolation with bend mitigates the instability in Eq. (2.27) and Eq. (2.33), crossing over to stability for large enough ϕ, but twist in Eq. (2.28) and Eq. (2.34) has no such effect. The twist-bend instability Eq. (2.28) and Eq. (2.34) should thus dominate, as it occurs for all ϕ except precisely $\pi/2$. This abundance of twisted unstable modes in Eq. (2.28) and Eq. (2.34), independent of the roles of polarity and inertia, is doubtless the explanation of the numerical observations of Shendruk *et al.* [57] in their study of three dimensional extensile active nematics. Figure 2.6 displays the growth or decay rates of the twist-bend mode as a function of wavenumber as v_0 is varied. We now turn to a comprehensive numerical study of the dynamics in the various regimes defined by our linear stability analysis.

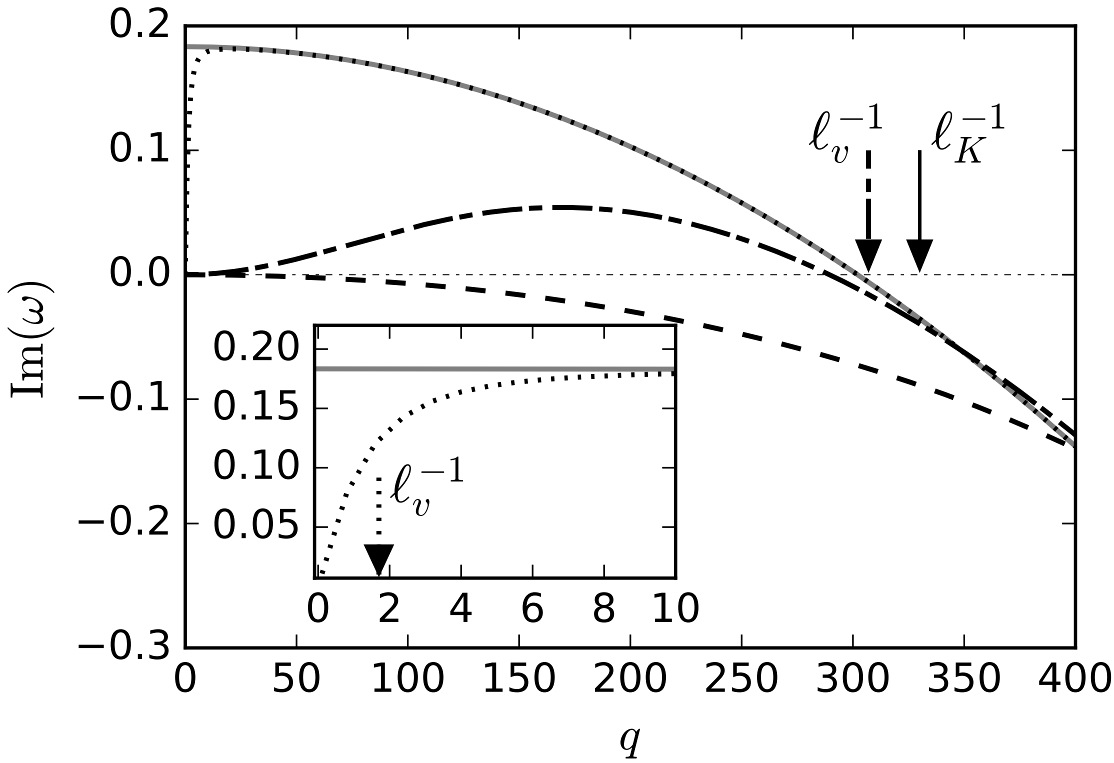

Figure 2.6: Growth rate versus wavenumber for Stokesian (gray line); $O(q)$ unstable: $\ell_v = 1$, $R = 5 \times 10^{-2}$ (black dotted line); $O(q^2)$ unstable: $\ell_v = 3 \times 10^{-3}$, $R = 4.5 \times 10^3$ (black dash-dotted); and stable: $\ell_v = 3 \times 10^{-4}$, $R = 4.5 \times 10^5$ (black dashed line) regime. Arrows indicate wavenumber corresponding to ℓ_v for the unstable cases. For all the dispersion curves we use $\phi = 55°$ and $K = 10^{-6}$ which sets $\ell_K = 3.2 \times 10^{-3}$

We summarise this section by noting that, when inertia is taken into account, orientable active suspensions can have two types of linear instability at small wavenumber q, governed by a control parameter R defined in Eq. (2.1). The instability growth-rates are of $O(q)$ for $R < R_1 = 1 + \lambda$ where λ is a flow-alignment parameter and $O(q^2)$ for $R_1 < R < R_2 \sim R_1/\beta$ where β is defined in Eq. (2.26). Linearly stable behaviour is found for $R > R_2$. As $\beta \sim 10^{-4}$ in molecular systems, the $O(q^2)$-unstable regime occupies a rather large range in parameter space. Indeed one could argue that the typical behaviour is that corresponding to the $\beta = 0$ limit, in which the aligned state is always linearly unstable, either at $O(q)$ or at $O(q^2)$. In the next chapter we gain insight beyond this linear analysis through a detailed numerical study to discover the long-time fate of the system in these unstable regimes.

2.3.1 Conclusions for suspensions with non-conserved concentration

1. We find a governing control parameter R which is the ratio of the inertial effects of self-propulsion to the scale of active stress as measured by the mean force-dipole density, and displays two thresholds R_1, R_2 obtained from linear stability analysis.

2. For $R < R_1$ we show a linear dependence of perturbation growth-rate on wavenumber q as $q \to 0$, which connects smoothly at higher wavenumbers to the classical Stokesian instability [1] of active suspensions.

3. Linear instability persists for $R_1 < R < R_2$, but the disturbance growth-rate at low wavenumbers is diffusive.

4. These thresholds are exclusively for *extensile* suspensions; we have shown that inertia cannot prevent the instability of *splay* distortions in *contractile* suspensions.

5. Finally we highlight the distinct role of three dimensional perturbations in the destabilization of extensile suspensions.

2.4 Stability analysis of incompressible active suspensions

2.4.1 Hydrodynamic equations

So far we have considered a number non-conserving system where the active particle concentration is maintained at a steady uniform value by the dynamic balance of births and deaths. The 'fast' relaxation of concentation fluctuations has enabled us to confine our system dynamics to that of velocity and polar order alone, without any further constraints. We now consider a dense number-conserving system of active particles in a fluid. The high particle concentration nullifies all spatial and temporal gradients of concentration fluctuations. Thus Eq. (2.5) reduces to $\nabla \cdot \boldsymbol{p} = 0$, i.e. the director field is solenoidal. The hydrodynamic model for an incompressible active suspension are thus Eqs. (2.3) and (2.4) with the additional constraint, namely divergence free director field, which is enforced by a pressure-like term Π in the director equation. Further, here also we find that the leading order stability behavior which affects all of our results is not affected by the polar active stress and the cross-coupling term aligning the polar orientation with the local flow gradients. We therefore refrain from using them in our subsequent discussions. Here we re-write the governing equations:

$$\begin{aligned}\rho(\partial_t \boldsymbol{u} + \boldsymbol{u} \cdot \nabla \boldsymbol{u}) &= -\nabla P + \mu \nabla^2 \boldsymbol{u} + \nabla \cdot (\boldsymbol{\Sigma}^a + \boldsymbol{\Sigma}^r), \text{ and} \\ \partial_t \boldsymbol{p} + (\boldsymbol{u} + v_0 \boldsymbol{p}) \cdot \nabla \boldsymbol{p} &= -\nabla \Pi + \lambda \mathrm{S} \cdot \boldsymbol{p} + \boldsymbol{\Omega} \cdot \boldsymbol{p} + \Gamma \boldsymbol{h}\end{aligned}$$

subjected to the constraints $\nabla \cdot \boldsymbol{u} = 0$, $\nabla \cdot \boldsymbol{p} = 0$ enforcing incompressibility of the velocity and polar order parameters respectively.

2.4.2 Linear Stability analysis

As described for compressible systems, here also study the stability of the ordered state ($c = c_0, \boldsymbol{u} = 0, \boldsymbol{p} = \hat{\boldsymbol{x}}$) to transverse perturbations. Here the concentration field value is a constant in space and time because of incompressibility of the director field. We thus study the dynamics of the perturbations $\boldsymbol{\delta u}_\perp, \boldsymbol{\delta p}_\perp$ to the velocity and the director fields respectively. Furthermore, here the perturbation component of the director field along the ordering axis is coupled to the transverse components by means of incompressibility; and thus cannot be rendered fast. The respective fields are thus decomposed as: $\boldsymbol{u} = \delta u_x \hat{\boldsymbol{x}} + \boldsymbol{\delta u}_\perp$ and $\boldsymbol{p} = (1 + \delta p_x)\hat{\boldsymbol{x}} + \boldsymbol{\delta p}_\perp$. The main differences in the linearization of various terms which distinguish the incompressible system from the compressible one are:

- The polar ordering term $(|\boldsymbol{p}|^2 - 1)\boldsymbol{p}$ leads to a contribution $2\delta p_x \hat{\boldsymbol{x}}$ to the molecular field $\boldsymbol{h}$, which is absent in the compressible system. As a result the reversible elastic restoration stresses on the velocity field of the incompressible system has an additional term $\sim \lambda \nabla \delta p_x$.

- The lowest order active force leads only to a term $\partial_x \boldsymbol{\delta p}_\perp$. The other term $\sim \nabla \cdot \boldsymbol{\delta p}$ is zero because of incompressibility.

The equations for the linearized transverse fluctuations are thus:

$$\rho \partial_t \boldsymbol{\delta u}_\perp = -\nabla_\perp P + \mu \nabla^2 \boldsymbol{\delta u}_\perp - \sigma_0 \partial_x \boldsymbol{\delta p}_\perp - (\lambda+1) K \nabla^2 \partial_x \boldsymbol{\delta p}_\perp / 2 + 2\lambda \nabla \delta p_x \tag{2.35}$$

for the hydrodynamic velocity and

$$\partial_t \boldsymbol{\delta p}_\perp + v_0 \partial_x \boldsymbol{\delta p}_\perp = -\nabla_\perp \Pi + (\lambda+1)\partial_x \boldsymbol{\delta u}/2 + (\lambda-1)\nabla_\perp \delta u_x/2 + \Gamma K \nabla^2 \boldsymbol{\delta p}_\perp - 2\delta p_x \hat{\boldsymbol{x}} \tag{2.36}$$

for the polar order parameter. Applying normal mode expansion of the perturbation quantities in the same way as described for the compressible system and substituting pressure terms using incompressibility we have the following dispersion relations for the Fourier amplitudes of perturbations:

$$\rho(\omega + i\nu q^2) \boldsymbol{\delta u}_{\perp \boldsymbol{q}} = \left[\sigma_0 - (\lambda+1) K q^2/2\right] q_x \boldsymbol{\delta p}_{\perp \boldsymbol{q}} \tag{2.37}$$

$$(\omega - v_0 q_x + i\Gamma K q^2) \boldsymbol{\delta p}_{\perp \boldsymbol{q}} = 2 i q_x \delta p_{xq} \boldsymbol{q}_\perp / q^2 - (\lambda+1) q_x \boldsymbol{\delta u}_{\perp \boldsymbol{q}}/2 \tag{2.38}$$

Here the hydrodynamic pressure terms are $\hat{P} = 2\lambda \delta p_{xq}$ and $\hat{\Pi} = (\lambda-1)\delta u_{xq}/2 + 2 i q_x \delta p_{xq}/q^2$.

In two dimensions Eqs. (2.37) and (2.38) lead to the dispersion relation

$$2\omega_{2d\pm} = v_0 q \cos\phi - i\nu_+ q^2 - 2i \sin^2\phi \pm \sqrt{A + Bq + Cq^2 + Dq^3 + Eq^4} \tag{2.39}$$

where $A = -4\sin^4\phi$, $B = -4 i v_0 \sin^2\phi \cos\phi$, $C = v_0^2 \cos^2\phi + 4\nu_- \sin^2\phi - 2(\lambda+1)\cos^2\phi(\sigma_0 - 2\lambda \sin^2\phi)/\rho$, $D = 2 i \nu_- v_0 \cos\phi$, $E = -\nu_-^2 + (\lambda+1)^2 K \cos^2\phi/\rho$.

One can easily check that $\phi = 0$ which corresponds to a pure bend is most unstable. Also it is readily observed that $\phi = \pi/2$ which corresponds to a pure splay along the ordering direction, doesnt exist because incompressibility always balances it out by an equal and opposite current of $\partial_x \delta p_x$. Any perturbation angle between 0 and $\pi/2$ is thus a bend perturbation with decreasing intensity; and thus an increasing propensity towards stability with ϕ being increasingly closer towards $\pi/2$. It should be further noted here that any non-zero splay locally induces an opposite gradient of the director field along the ordering direction to ensure incompressibility. Thus we see here that here the perturbation gradients along the ordering directions are coupled to the perpendicular ones, and thus cannot be rendered fast. Taylor expanding Eq. (2.39) for low wavenumbers[1] we have:

$$2\omega_{2d\pm} \simeq v_0 q_x - i\nu_+ q^2 - 2i\sin^2\phi \pm \left[\sqrt{A} + (Bq + Cq^2 + Dq^3 + Eq^4)/2\sqrt{A}\right] \tag{2.40}$$

For $|\lambda| < 1$ and in the limit $\nu >> \Gamma K$ one can see that the leading order destabilizing contribution is at $O(q^2)$ from the term $C/2\sqrt{A}$ which, on substitution, gives $i\left[2(\lambda+1)\sigma_0\cos^2\phi/\rho - 4\nu_-\sin^2\phi - v_0^2\cos^2\phi\right]/2\sin^2\phi$. This can go unstable for extensile systems when $\sigma_0 >> \rho\nu_- + \rho v_0^2$, and can never destabilize in contractile systems where $\sigma_0 < 0$. We thus arrive at the following conclusions: (a) The leading order instability in two dimensional incompressible extensile suspensions is always one order in wavenumber higher than the compressible one(recall Eq. (2.21)). Besides, the the coupled effects of viscosity and polar ordering $\sim \nu_-\sin^2\phi$ competes with the active stress and thus further adds to the stabilizing contribution for $\phi \neq 0$. Thus the two dimensional incompressible system where only these modes can be physically present, has a much lower threshold for instability than the compressible. (b) Two dimensional contractile suspensions are always linearly stable.

The three dimensional system, as we have already discussed in the previous section, has four eigenmodes. Two of them are the bend modes, whose dispersion relation can be obtained by taking in-plane divergence of Eqs. (2.37) and (2.38). The resulting expressions are same as Eq. (2.39). However, here are the two other modes which represent the coupled dynamics of bend and twist. Their dispersion relation can be obtained by taking in-plane curl on the Eqs. (2.37) and (2.38). The resulting expression is the same as Eq. (2.22) for the compressible system. As already discussed, these are the dominant failure modes for extensile system. Now one can again recall from this Equation that the leading order instability for these modes is at $O(q)$. Therefore the three dimensional system intrinsically has more

[1]Note that the small q expansion of Eq. (2.39) is not valid for $\phi = 0$, at which $A = 0$, which thus leads to blowing up of the bracketed terms in Eq. (2.40). Substituting $\phi = 0$ in Eq. (2.39) we see that the leading order imaginary contribution is $\sqrt{C}q$, which is unstable when $\rho v_0^2/2\sigma_0 < 1 + \lambda$, i.e. $R < R_1$. This is same as the $O(q)$ instability criterion for compressible system.

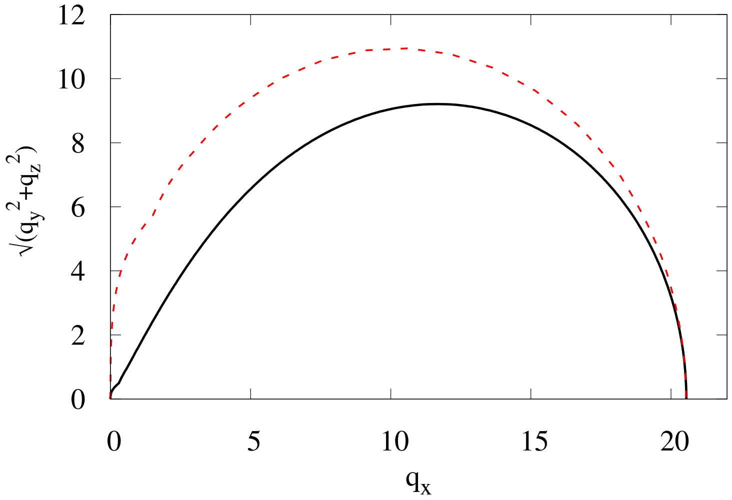

Figure 2.7: Stability of bend modes(black line) vs bend-twist modes(red dashed line) for $R = 5 \times 10^{-2}$. Note that the unstable region for the incompressible system is very close to the compressible.

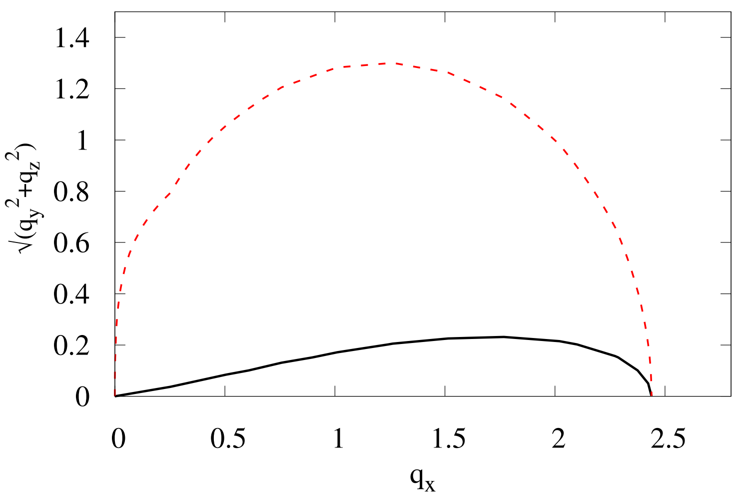

Figure 2.8: Stability of bend modes(black line) vs bend-twist modes(red dashed line) for $R = 0.35$. Here the unstable region for the incompressible system is significantly less than the compressible.

unstable modes than the two dimensional one. Further these modes are also stable in a contractile system as we have discussed in the previous section. Thus our

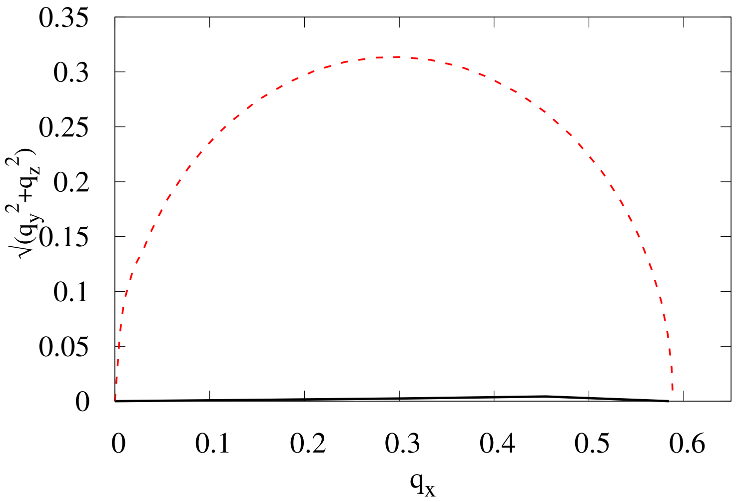

Figure 2.9: Stability of bend modes(black line) vs bend-twist modes(red dashed line) for $R = 2$. Here the unstable region for the incompressible system is barely visible, implying that the turbulence in the compressible and the incompressible systems should be grossly different.

findings are: (A) Contractile incompressible active suspensions are always linearly stable, and (B) two and three dimensional systems exhibit significant departure in the range of unstable modes. This is shown in Figures 2.7- 2.9, where one clearly sees the difference becomes more prominent as one increases R froom near zero to near R_1.

2.4.3 Conclusions for incompressible suspensions

1. We find that the linear stability behavior of extensile incompressible suspensions is same as compressible. The governing control parameter R, the thresholds R_1, R_2 remain unchanged.

2. Incompressibility supresses the pure splay mode along the ordering direction, thus contractile suspensions are always stable. This is a stark contrast to compressible suspensions where where inertia cannot stabilize contractile suspensions.

3. Over a certain range of R, two and three dimensional extensile systems are

seen to have drastically different stability zones. This should reflect in their turbulence.

Appendix

Effects of the concentration field

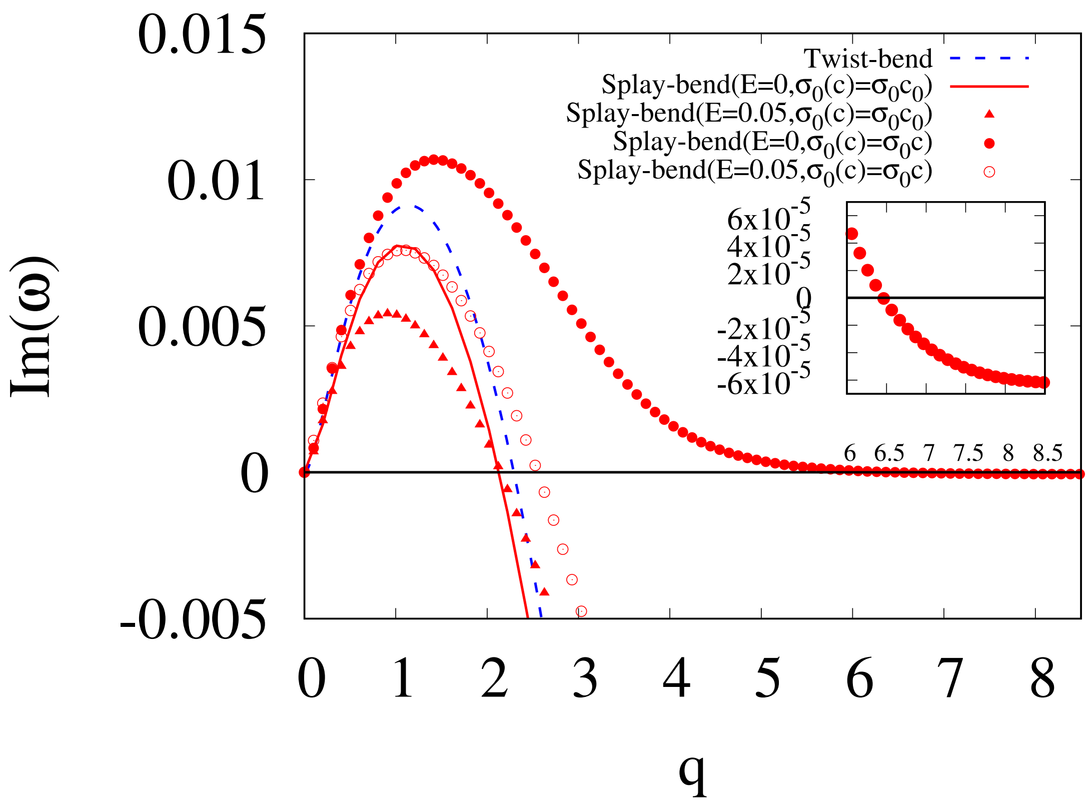

Figure 2.10: Concentration dependence on Growth rates: **Parameters:** $\phi = 15°, R = 1.25, \nu = 10^{-1}, \Gamma K = 10^{-3}, \lambda = 0.1$. Growth rate dependence on osmotic coefficient (σ_3) and active stress sensitivity to concentration fluctuations (α). Inset is a magnified view of the red-dotted curve at higher wavenumbers, showing that it is stable.

As described in main chapter, the concentration fluctuations are reflected in the osmotic term in the polar order equation and a multiplier of the active stress in the velocity equation. The comparison of these two terms on the growth rates of the most unstable modes are shown in Figure 2.10. The blue-dashed and red line curves are respectively for the twist-bend and splay-bend modes without concentration dependence(i.e. $E = 0$, $\sigma_0(c) = \sigma_0 c_0$). As discussed in the main section the bend-twist modes are insensitive to concentration fluctuations. The dispersion curve for the splay-bend mode considering only the effect of the osmotic term is shown by red triangles. From this we clearly understand that a positive osmotic coefficient E for concentration gradients has a stabilizing effect. Likewise, the dispersion curve considering the concentration fluctuation effects only on the active stress has been drawn with filled circles. It shows that the active stress sensitivity to concentration fluctuations has a destabilizing effect. However a realistic description of a physical system should include both these concentration couplings. The curve with open circles shows the most unstable splay-bend mode for a system having both osmotic and active-stress contributions from concentration fluctuations. We see that this is essentially not different from the one where both these effects are ignored. Thus we see that the mutually opposing effects of concentration fluctuations on the osmotic term and active-stress coefficients lead to negligibly small departure of the stability from one without concentation fluctuations. Thus we neglect the effects of concentration fluctuations in the major analyses.

Stability of Splay-bend vs twist-bend modes

We re-write the dispersion relation Eq. (2.21) for the splay-bend modes:

$$\omega = \omega^s_\pm = \frac{1}{2} v_0 q \cos\phi - i\frac{\mu_+}{2\rho} q^2 \pm \left(\frac{\sigma_0}{2\rho}\right)^{1/2} \left[A(\phi) q^2 + 2iB(\phi) q^3 + G(\phi) q^4\right]^{1/2}$$

and Eq. (2.22) for the twist-bend modes:

$$\omega^t_\pm = \frac{1}{2} v_0 q \cos\phi - i\frac{\mu_+}{2\rho} q^2 \pm \left(\frac{\sigma_0}{2\rho}\right)^{1/2} \left[A(0)\cos^2\phi q^2 + 2iB(0)\cos\phi q^3 + \bar{G}(\phi) q^4\right]^{1/2}$$

The growth-rates of the splay-bend modes vs twist-bend modes are shown in Figure 2.11 for an extensile system and Figure 2.12 for contractile systems. Specially note that here the extensile cases with $\nu = \Gamma K$ are unstable because of $O(q)$ instability. For both the black lines denote the neutral curves ($\mathrm{Im}(\omega) = 0$ isocontours) for the splay-bend modes for all possible angular orientations of the wavevector $\boldsymbol{q} = (q_x, \boldsymbol{q}_\perp)$, where $\boldsymbol{q}_\perp = \sqrt{q_y^2 + q_z^2}$. In Figure 2.11 the area enclosed within the neutral curve and the horizontal (q_x) axis is the zone of linearly unstable modes. Likewise in Figure 2.12 the area enclosed within the neutral curve and the vertical ($q_\perp$) axis is the zone of linearly unstable modes. Any wavevector lying outside this zone is linearly stable. The neutral curve for the twist-bend modes is shown by red circles in Figure 2.11. For the limits $\nu >> \Gamma K$ and $\nu = \Gamma K$ for the Stokesian $\partial_t \boldsymbol{u} = 0$ and inertial, i.e. unsteady Stokesian ($\partial_t \boldsymbol{u} \neq 0$) systems. For all we see that the neutral curve for the twist-bend modes always encloses the one for the splay-bend modes, implying that for extensile systems the twist-bend modes always contain more unstable wavenumbers than the splay-bed modes. These are thus the dominant instability modes for extensile systems. For contractile systems (Figure 2.12) the neutral curve for the bend-twist modes donot exist and hence are not visible. These systems are, therefore, only splay unstable.

General form of eigenvectors(without concentration)

Here we write the matrix representation for the dispersion relation without considering the effects of concentration fluctuations, i.e. Eqs. (2.19) and (2.20). These two can be written as the matrix equation:

$$AX = 0$$

where

$$A = \begin{bmatrix} \omega_\nu & 0 & b_1/\rho & b_2/\rho \\ 0 & \omega_\nu & b_2/\rho & b_3/\rho \\ a_1 & a_2 & \omega_K & 0 \\ a_2 & a_3 & 0 & \omega_K \end{bmatrix}$$

and

$$X^T = \begin{bmatrix} \delta \boldsymbol{u}_{yq} & \delta \boldsymbol{u}_{zq} & \delta \boldsymbol{p}_{yq} & \delta \boldsymbol{p}_{zq} \end{bmatrix}.$$

All symbols have same definitions as described in subsection 2.2.2 of the main chapter. The same subsection also contains detailed discussion on the eigenvalues and we dont repeat them here. The Eigenvectors have the general form:

$$V^T = \begin{bmatrix} n & 1 & l & m \end{bmatrix}$$

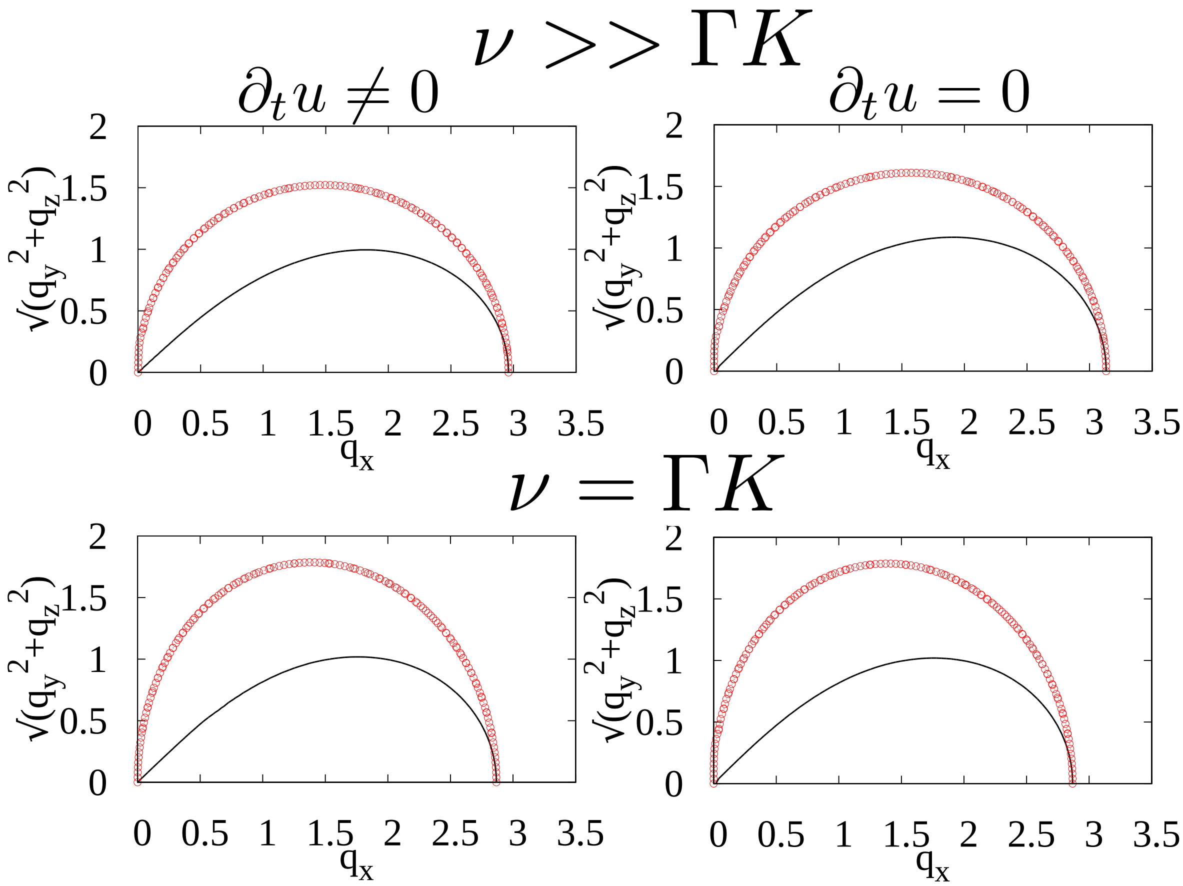

Figure 2.11: **Stability diagrams for an extensile system** ($\sigma_0 > 0$)**:** Neutral stability ($\mathrm{Im}(\omega) = 0$) curves for unsteady Stokes ($\partial_t u \neq 0$) system (Left column) vs Stokes system ($\partial_t u = 0$) (Right Column). A sample case is shown with $\nu >> \Gamma K$(Top Row) and $\nu = \Gamma K$(Bottom Row). The black lines are the neutral lines for modes 1,2 and red circles are for modes 3,4.

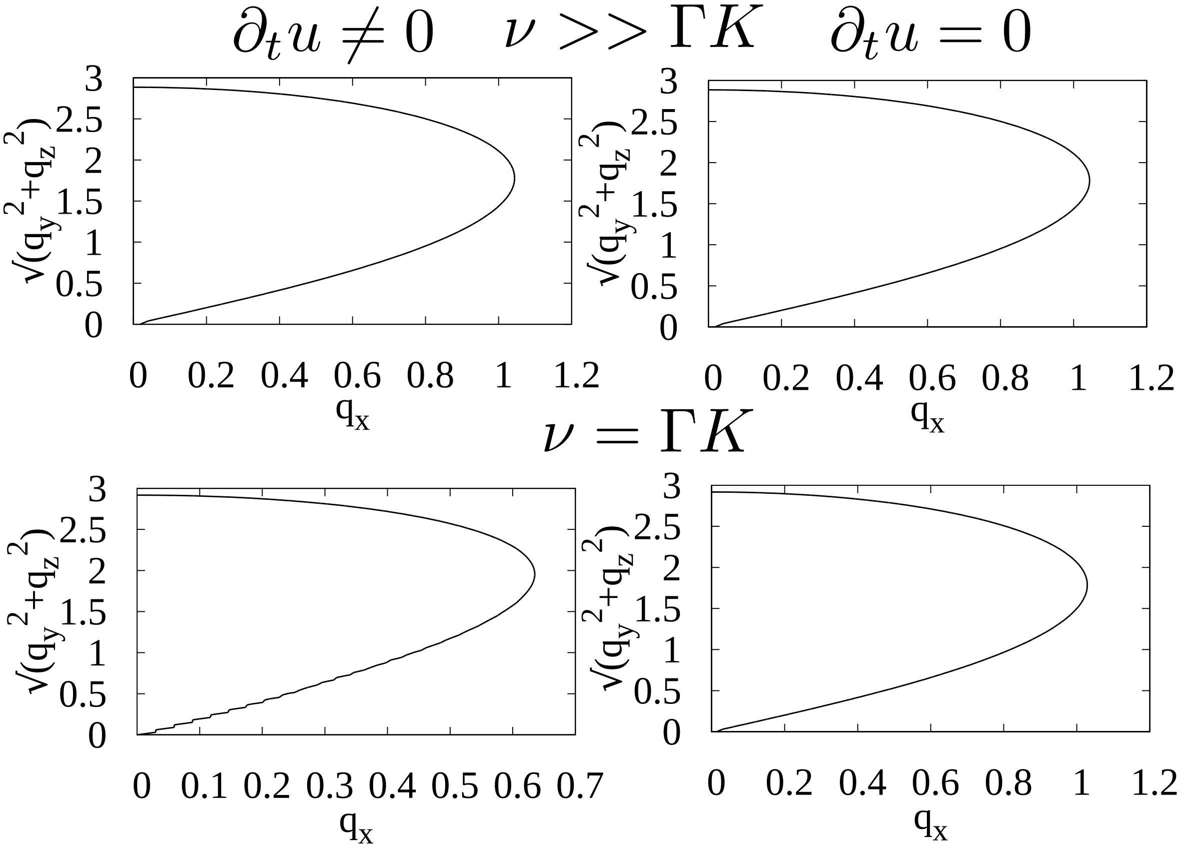

Figure 2.12: **Stability diagrams for a contractile system ($\sigma_0 < 0$):** Neutral stability ($\mathrm{Im}(\omega) = 0$)curves for unsteady Stokes ($\partial_t u \neq 0$) system(Left column) vs Stokes system($\partial_t u = 0$)(Right Column). A sample case is shown with $\nu >> \Gamma K$(Top Row) and $\nu = \Gamma K$(Bottom Row). The black lines are the Neutral lines for modes 1,2. Note that Red circles are absent because 3,4 modes are always stable.

where

$$
\begin{aligned}
n &= \frac{-a_2 b_2^2 + a_2 b_1 b_3 + \rho b_2 \omega_K \omega_\nu}{a_1(b_2^2 - b_1 b_3) + \rho b_3 \omega_K \omega_\nu}, \\
l &= -\frac{(a_1 b_2 + a_2 b_3)\rho\omega_\nu}{a_1(b_2^2 - b_1 b_3) + \rho b_3 \omega_K \omega_\nu}, \text{ and} \\
m &= \frac{(a_1 b_1 + a_2 b_2 - \rho\omega_K\omega_\nu)\rho\omega_\nu}{a_1(b_2^2 - b_1 b_3) + \rho b_3 \omega_K \omega_\nu}.
\end{aligned}
$$

As a check one can input the values of a_{1-3}, $b_{1,3}$, $\omega_{\nu,K}$ for all the eigenfrequencies ω_{1-4} and find that for two of these frequencies the vectors $[n\ \ 1]$ and $[l\ \ m]$ are both parallel to the vector $\boldsymbol{q}_\perp = [q_y\ \ q_z]$, and for the remaining two, both these vectors are perpendicular to $\boldsymbol{q}_\perp$. The former two frequencies are obviously the splay-bend modes and the later two are the twist-bend modes.

Effects of additional polar terms

We consider the effects of the polar active force $\gamma\nabla\cdot(\nabla\mathbf{p}+(\nabla\mathbf{p})^{\mathrm{T}})$ on the RHS of Eq. (2.3) and the flow-aligning term term $\ell\nabla^2\boldsymbol{u}$ on the RHS of Eq. (2.4). These in effect renormalizes the coefficients in Eqs. (2.21) and (2.22) as: $B(\phi) \to B(\phi) - \gamma(1 + \lambda\cos 2\phi) + 2\ell\sigma_0\cos 2\phi$ and $k(\phi) \to k(\phi) + 4\ell\gamma\cos^2\phi$, without affecting the leading order term in q. The essential conclusions thus remains unchanged. So these terms have been neglected in our analyses.

Bibliography

[1] R. A. Simha and S. Ramaswamy, Phys. Rev. Lett. **89**, 058101 (2002).

[2] S. Ramaswamy, Annu. Rev. Condens. Matter Phys. **1**, 323 (2010).

[3] M. C. Marchetti *et al.*, Rev. Mod. Phys. **85**, 1143 (2013).

[4] H. H. Wensink *et al.*, Proc. Natl. Acad. Sci. U. S. A. **109**, 14308 (2012).

[5] T. Vicsek *et al.*, Phys. Rev. Lett. **75**, 1226 (1995).

[6] J. Toner and Y. Tu, Phys. Rev. Lett. **75**, 4326 (1995).

[7] J. Toner, Y. Tu, and S. Ramaswamy, Ann. Physics **318**, 170 (2005).

[8] R. Voituriez, J. F. Joanny, and J. Prost, Europhys Lett. **70**, 404 (2005).

[9] V. V Fréedericksz and A. Repiewa, Z. Physik. **42**, 532 (1927).

[10] P. de Gennes and J. Prost, *The Physics of Liquid Crystals*, *International series of monographs on physics* (Clarendon Press, Oxford, 1993).

[11] B. Mart´inez-Prat, J. Ignés-Mullol, J. Casademunt, and F. Sagués, Nat. Phys. **15**, 362 (2019).

[12] G. Duclos *et al.*, Nat. Phys. **14**, 728 (2018).

[13] D. Saintillan, Annu. Rev. Fluid Mech. **50**, 563 (2018).

[14] L. Giomi and M. C. Marchetti, Soft Matter **8**, 129 (2012).

[15] L. Giomi, Phys. Rev. X **5**, 031003 (2015).

[16] J. Urzay, A. Doostmohammadi, and J. Yeomans, J. Fluid Mech. **822**, 762–773 (2017).

[17] E. Lauga and R. E. Goldstein, Phys. Today **65**, 30 (2012).

[18] K. Kruse *et al.*, Phys. Rev. Lett. **92**, 078101 (2004).

[19] L. Giomi, M. J. Bowick, X. Ma, and M. C. Marchetti, Phys. Rev. Lett. **110**, 228101 (2013).

[20] K. Gowrishankar and M. Rao, Soft Matter **12**, 2040 (2016).

[21] J. Elgeti, M. E. Cates, and D. Marenduzzo, Soft Matter **7**, 3177 (2011).

[22] A. Doostmohammadi, T. N. Shendruk, K. Thijssen, and J. Yeomans, Nat. Commun. (2016).

[23] S. P. Thampi, R. Golestanian, and J. M. Yeomans, Phil. Trans. R. Soc. A **372**, 20130366 (2014).

[24] L. Giomi *et al.*, Phil. Trans. R. Soc. A **372**, 20130365 (2014).

[25] T. Sanchez *et al.*, Nature **491**, 431-434 (2012).

[26] S. Decamp *et al.*, Nat. Mater. **14**, 1110–1115 (2015).

[27] C. Dombrowski *et al.*, Phys. Rev. Lett. **93**, 098103 (2004).

[28] T. Ishikawa *et al.*, Phys. Rev. Lett. **107**, 028102 (2011).

[29] A. Sokolov and I. S. Aranson, Phys. Rev. Lett. **109**, 248109 (2012).

[30] J. Dunkel *et al.*, Phys. Rev. Lett. **110**, 228102 (2013).

[31] V. Bratanov, F. Jenko, and E. Frey, Proc. Natl. Acad. Sci. **112**, 15048 (2015).

[32] Neither polar order [1] nor polar active stress [42, 58] alters the fundamental mechanism in the Stokesian limit.

[33] N. G. Chisholm, D. Legendre, E. Lauga, and A. S. Khair, J. Fluid Mech. **796**, 233–256 (2016).

[34] S. Wang and A. M. Ardekani, J. Fluid Mech. **702**, 286–297 (2012).

[35] G. Li, A. Ostace, and A. M. Ardekani, Phys. Rev. E **94**, 053104 (2016).

[36] T. Dombrowski *et al.*, Phys. Rev. Fluids **4**, 021101 (2019).

[37] D. Klotsa *et al.*, Phys. Rev. Lett. **115**, 248102 (2015).

[38] N. Riley, Quart. Journ. Mech. and Applied Math. **19**, 461 (1966).

[39] G. d'Etude des cristaux liquides Orsay, J. Chem. Phys. **51**, 816 (1969).

[40] E. M. Purcell, Am. J. Phys. **45**, 3 (1977).

[41] W. Kung, M. Cristina Marchetti, and K. Saunders, Phys. Rev. E **73**, 031708 (2006).

[42] M. C. Marchetti and T. N. Liverpool, in *Cell Motility*, edited by P. Lenz (Springer-Verlag, Berlin, 2007).

[43] A. Maitra *et al.*, arXiv:1901.01069 .

[44] K. Kruse *et al.*, Eur. Phys. J. E **16**, 5–16 (2005).

[45] We assume concentrations are high enough that F globally favours a nonzero magnitude for $\mathbf{p}$. We therefore ignore c-dependence in the polynomial part of F.

[46] F. C. Frank, Discuss. Faraday Soc. **25**, 19 (1958).

[47] H. Zocher, Trans. Faraday Soc. **29**, 945 (1933).

[48] C. W. Oseen, Trans. Faraday Soc. **29**, 883 (1933).

[49] D. Forster, Phys. Rev. Lett. **32**, 1161 (1974).

[50] H. Stark and T. C. Lubensky, Phys. Rev. E **67**, 061709 (2003).

[51] N. Kumar, H. Soni, S. Ramaswamy, and A. Sood, Nat. Commun. **5**, (2014).

[52] M. C. Marchetti, personal communication .

[53] Formally we could justify this neglect by introducing birth and death so that the concentration becomes a fast variable; see John Toner - *Birth, Death and Flight: A Theory of Malthusian Flocks*, Phys. Rev. Lett.,**108**,088102(2012).

[54] In molecular or colloidal systems $\mu/\rho \gg K/\mu$. Assuming this inequality holds for the systems of interest here as well, G and $\bar{G}$ are uniformly negative.

[55] A. M. Leshansky and O. Kenneth, Phys. Fluids **20**, 063104 (2008).

[56] Even for slow swimmers, one could imagine inertia, in the form of R, overcoming the force-dipole instability in the case of a swimmer with a small dipole (and hence a small σ_0), propelled mainly by its quadrupole force moment.

[57] T. N. Shendruk, K. Thijssen, J. M. Yeomans, and A. Doostmohammadi, Phys. Rev. E **98**, 010601 (2018).

[58] L. Giomi, M. C. Marchetti, and T. B. Liverpool, Phys. Rev. Lett. **101**, 198101 (2008).

Chapter 3

Turbulence in polar active suspensions

In the last chapter we have discussed the conditions under which the polar order in a wet active flock is linearly unstable. We now describe the long-time fate of the linearly unstable configurations, which we obtain through a detailed numerical study. Our non-dimensional control parameter is R which, as discussed in the last chapter, denotes the ratio of the inertial effects of polarity to the active forces. We first describe the numerical procedures and the parameter sets that we use in while performing direct numerical simulation(DNS) of our equations. We then demonstrate that our numerical solutions, at initial times, show excellent agreement with linear stability. After having a short discussion on the importance of ensuring grid convergence, we describe the statistically steady turbulent-like states which we obtain for $R < R_1$ and $R > R_1$; specifically we find that the turbulence for $R < R_1$ is characterised by the presence of hedgehog defects whereas for $R > R_1$ we observe a phase-turbulence characterized by a noisy but aligned flock. We then describe the nonequilibrium phase transition from the defect turbulence to phase turbulence on crossing the critical boundary $R = R_1$. This is followed by a discussion on the scaling behavior of the turbulent spectra for the power spectrum of the velocity and director fields for $R < R_1$, and the power-laws which we observe in the spectra for both $R < R_1$ and $R > R_1$. We finally conclude by highlighting the fundamental differences between the turbulence in extensile versus contractile suspensions.

3.0.1 Governing equations

Eqs. (3.1) and (3.2) describe the dynamics of the velocity and the polar order parameter fields in a polar active suspension. We re-write them for clarity.

$$\rho(\partial_t \boldsymbol{u} + \boldsymbol{u}\cdot\nabla\boldsymbol{u}) = -\nabla P + \mu\nabla^2\boldsymbol{u} + \nabla\cdot(\boldsymbol{\Sigma}^a + \boldsymbol{\Sigma}^r), \text{ and} \tag{3.1}$$

$$\partial_t \boldsymbol{p} + (\boldsymbol{u} + v_0\boldsymbol{p})\cdot\nabla\boldsymbol{p} = \lambda \mathsf{S}\cdot\boldsymbol{p} + \boldsymbol{\Omega}\cdot\boldsymbol{p} + \Gamma\boldsymbol{h} \tag{3.2}$$

The active stress $\boldsymbol{\Sigma}^a \equiv \sigma_a(c)\boldsymbol{pp}$, the (passive) elastic relaxation stress $\boldsymbol{\Sigma}^r = \frac{\lambda+1}{2}\boldsymbol{hp} + \frac{\lambda-1}{2}\boldsymbol{ph}$, and $\boldsymbol{h} = -\delta F/\delta\boldsymbol{p}$ is the molecular field conjugate to p, derived from a free-energy functional $F = \int d^3r[(1/4)(\boldsymbol{p}\cdot\boldsymbol{p}-1)^2 + (K/2)(\nabla\boldsymbol{p})^2 - E\boldsymbol{p}\cdot\nabla c]$. As shown in the last chapter, the ordered state is linearly unstable to splay-bend and twist-bend distortions. The corresponding dispersion relations are:

$$\omega = \omega_\pm^s = \frac{1}{2}v_0 q\cos\phi - i\frac{\mu_+}{2\rho}q^2 \pm \left(\frac{\sigma_0}{2\rho}\right)^{1/2}\left[A(\phi)q^2 + 2iB(\phi)q^3 + G(\phi)q^4\right]^{1/2} \tag{3.3}$$

for the splay-bend modes and

$$\omega_\pm^t = \frac{1}{2}v_0 q\cos\phi - i\frac{\mu_+}{2\rho}q^2 \pm \left(\frac{\sigma_0}{2\rho}\right)^{1/2}\left[A(0)\cos^2\phi q^2 + 2iB(0)\cos\phi q^3 + \bar{G}(\phi)q^4\right]^{1/2} \tag{3.4}$$

for the twist-bend modes. In Eqs. (3.3) and (3.4) we have defined $A(\phi) = R\cos^2\phi - \cos 2\phi(1 + \lambda\cos 2\phi)$ where $R \equiv \rho v_0^2/2\sigma_0$, $B(\phi) = (v_0\mu_-/\sigma_0)\cos\phi$, $G(\phi) = -(\mu_-^2/2\rho\sigma_0) + (K/2\sigma_0)(1+\lambda\cos 2\phi)^2$, and $\bar{G}(\phi) = -(\mu_-^2/2\rho\sigma_0) + (K/2\sigma_0)(1+\lambda)^2\cos^2\phi$ where $\mu_\pm = \mu(1\pm\beta)$ and $\beta \equiv \rho\Gamma K/\mu$.

3.0.2 Direct Numerical Simulations (DNS)

We numerically integrate Eqs. (3.1) and (3.2) in square and cubic domains of volume $\mathcal{L}^d$ and discretize it with N^d collocation points. In the last chapter we have discussed that the most unstable modes in two dimensional systems are the splay-bend distortions, whereas in three-dimensions they are the twist-bend. Nevertheless, for a fixed R we find almost identical turbulence statistics for the two and three-dimensional systems. The reason, we believe, is a close match between the range of unstable wavenumbers in both. We thus demonstrate most of our numerical results using 2D simulations and add 3D results to illustrate their agreement. We spatially discretize Eq. (3.1) using a pseudo-spectral method [1]; for Eq. (3.2)

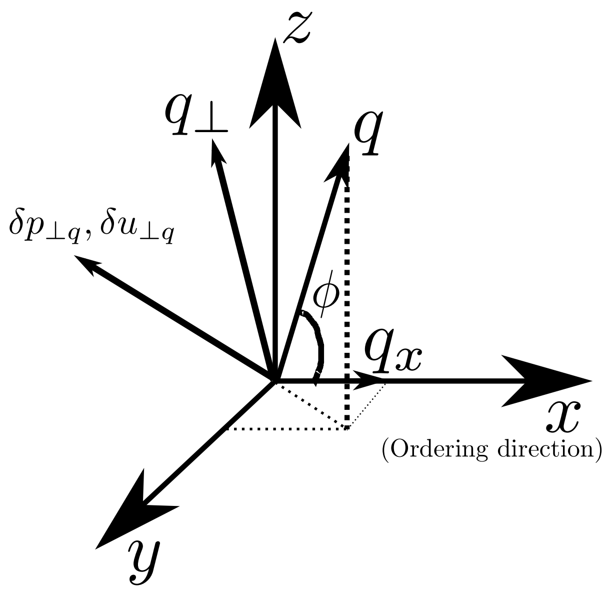

Figure 3.1: Propagation wave vector and amplitude vectors for perturbations to order parameter and velocity.

	D	$\mathcal{L}$	N	$v_0(\times 10^{-2})$	$K(\times 10^{-3})$	$R \equiv \rho v_0^2/2\sigma_0$
`SPP0`	3	2π	32	3×10^2	0	4.5
`SPP1`	3	2π	128	3.16	1	$0.005, 0.02, 0.0625$
`SPP2`	3	10π	160	0.7,13.4	2	$0.01, 4$
`SPP3`	3	10π	320	3.16	1	$0.1 - 2$
`SPP4`	2	20π	1024	3.16	1	$0.05 - 2.0$
`SPP5`	2	30π	1024	3.16	1	$0.15, 0.20$
`SPP6`	2	40π	2048	3.16	1	$0.25, 0.30, 0.35$
`SPP7`	2	60π	3072	3.16	1	$0.4 - 0.6$
`SPP8`	2	80π	4096	3.16	1	0.7

Table 3.1: Spatial dimension D of the domain and parameters $\mathcal{L},\ N,\ \nu,\ v_0,\ K$, and R used in our direct numerical simulations. The suspension density $\rho = 1$, $\lambda = 0.1$, $\mu = 0.1$ and the rotational mobility $\Gamma = 1$ are kept fixed for all the runs.

we use a fourth-order central finite-difference scheme. We use a second-order explicit Adams-Bashforth scheme [2] for time integration. Essentials of these numerical methods are described in the Appendix. Consistent with the linear stability analysis conducted earlier, we choose an uniform ordered state with transverse monochromatic perturbation as the initial condition, i.e. $\boldsymbol{u} = \boldsymbol{0} + A\hat{\boldsymbol{e}}_\perp \cos \boldsymbol{q}\cdot\boldsymbol{r}$, $\boldsymbol{p} = \hat{\boldsymbol{x}} + B\hat{\boldsymbol{e}}_\perp \cos \boldsymbol{q}\cdot\boldsymbol{r}$ where $\hat{\boldsymbol{e}}_\perp \equiv (\hat{\boldsymbol{y}}+\hat{\boldsymbol{z}})/\sqrt{2}$ is a unit vector in the plane perpendicular to the ordering direction, and we have made the arbitrary but acceptable choice $A = B = 10^{-3}$. We monitor the time evolution of perturbations in the initial stages and find that their propagation speeds and growth rates show good agreement with linear stability. We record our simulation results for long enough to ensure adequate number of snapshots for correct resolution of the statistics in the turbulent steady state. In Table 3.1, we summarize the parameters used in our DNS.

3.0.3 Benchmarks (Neutral limit)

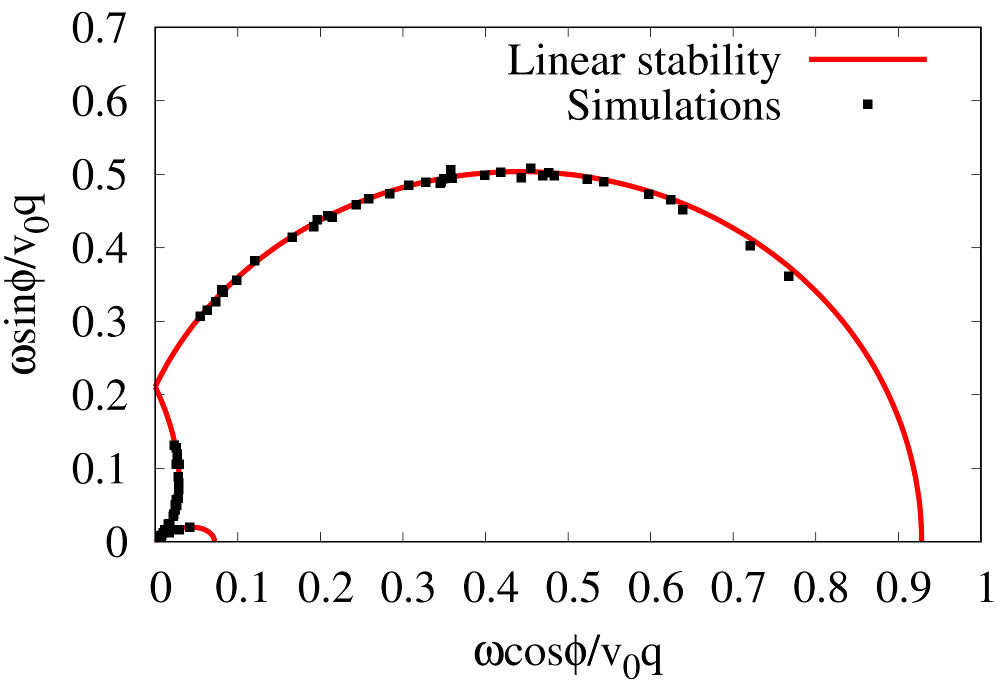

Figure 3.2: Polar plot for frequencies of splay waves at various angles (ϕ) w.r.t ordering direction. Red curve is obtained from linear stability theory black points are from analysis of simulation data.The simulations are done on 32^3 grid with time-step $dt = 10^{-3}$. The simulation parameters are $\nu = 0, K = 0, v_0 = 3, p_0 = 1, \sigma_0 = 1$ and all possible combinations of q_x, q_y and q_z where each one takes values between 1 to 4.

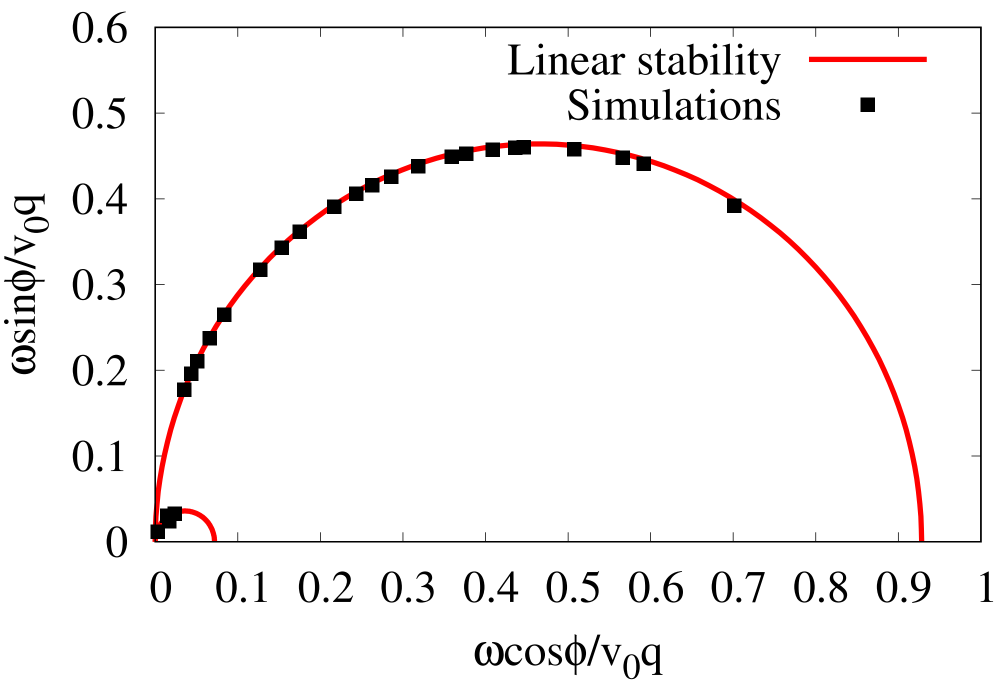

Figure 3.3: Polar plot for frequencies of bend waves at various angles (ϕ) w.r.t ordering direction. Red curve is obtained from linear stability theory black points are from analysis of simulation data.The simulations are done on 32^3 grid with time-step $dt = 10^{-3}$. The simulation parameters are $\nu = 0, K = 0, v_0 = 3, p_0 = 1, \sigma_0 = 1$ and all possible combinations of q_x, q_y and q_z where each one takes values between 1 to 4.

Here we describe the system in which the perturbation to the polar ordered state neither grow or decay, but rather propagate as waves by virtue of the fore-aft asymmetry of the governing equations. The analytical form of the dispersion relation for these waves have been discussed in [3], which is the case when the diffusive terms ν, K are zero, and also $R > 1 + \lambda$ so as to ensure that the inertial effects of self propulsion always dominates activity. Under these conditions the dispersion relations given by Eqs. (3.3) and (3.4) for the splay-twist and bend-twist waves respectively simplify to:

$$\omega_{\pm}^{sb} = \frac{1}{2} v_0 q \cos\phi \left(1 \pm \sqrt{1 - \frac{1}{R}(1 - \tan^2\phi)(1 + \lambda \cos 2\phi)} \right) \tag{3.5}$$

and

$$\omega_{\pm}^{tb} = \frac{1}{2} v_0 q \cos\phi \left(1 \pm \sqrt{1 - \frac{1+\lambda}{R}}\right) \tag{3.6}$$

In figure 3.1 we show the alignment of the propagation wave vector $\boldsymbol{q}$ and the Fourier amplitude vectors $\boldsymbol{\delta p}_{\perp \boldsymbol{q}}, \boldsymbol{\delta u}_{\perp \boldsymbol{q}}$ of the perturbation quantities. We study the perturbation signal dynamics in the neutrally stable limit for the parameters mentioned in the row SPP0 in Table 3.1. We perturb the polar ordered state at various angles ϕ and take FFT of the time signals for the in-plane splay-twist waves $(\nabla_\perp \cdot \boldsymbol{p}_\perp)$ and in-plane twist-bend waves $(\nabla_\perp \times \boldsymbol{p}_\perp)$ calculated from simulation data. We overlay these values over their respective dispersion curves obtained from the analytical solutions of Eqs. (3.5) and (3.6) for ϕ values between 0 to $\pi/2$. The polar plots for the propagation speed of the splay-bend waves are shown in figure 3.2 and those for the twist-bend waves are shown in figure 3.3. In both of these, the red lines indicate the analytical solutions and black dots denote numerically obtained results, both of which show excellent agreement.

3.1 Instability growth and turbulence

Now we discuss how the different instability mechanisms lead to spatio-temporal types of turbulence. The linear instability mechanisms for $R < R_1$ and $R_1 < R < R_2$ cause growth of perturbations and eventually turbulence. In this section we first describe the initial dynamics of perturbation signals and the steady-state turbulent properties for $R < R_1$ and $R > R_1$ and then unravel a inertia driven nonequilibrium phase transition which we observe on crossing the critical boundary $R = R_1$.

3.1.1 Initial growth of instabilities

We now present a comparison between the initial temporal growth rate obtained from the DNS with analytical prediction of the linear stability. The plot of the bend-twist dispersion curve given by Eq.(3.4) for $\phi = 55^\circ$ is shown in figure 3.4 for $R < R_1$ (continuous line) and $R > R_1$ (dashed line). Black dots indicate the the initial temporal growth rate of perturbations obtained from our DNS, which shows

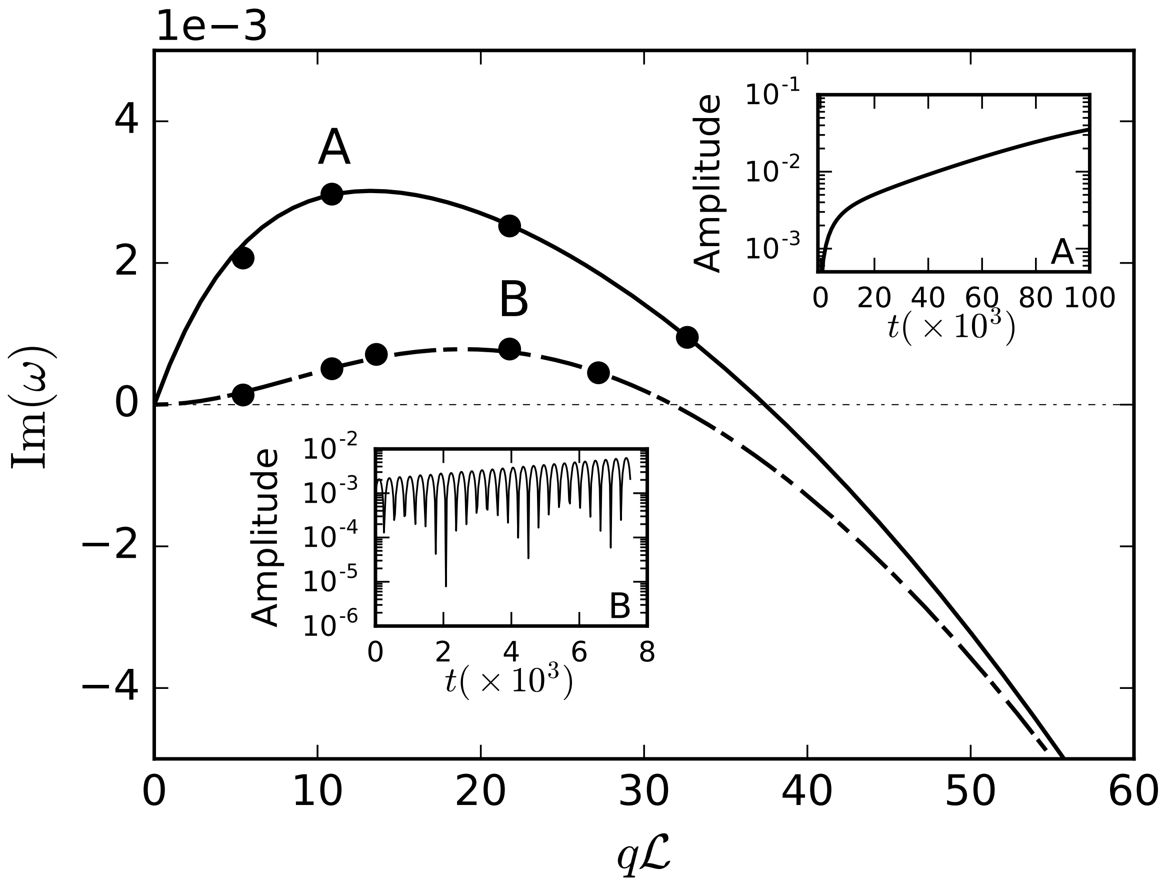

Figure 3.4: Comparison of the growth rates obtained from dispersion relation Eq. (3.4) with those from DNS (black dots). (Inset) Initial time-evolution of the perturbation amplitude $|\boldsymbol{q}_\perp \times \delta \boldsymbol{p}_{\perp q}|$ for $O(q)$: $R = 10^{-2}$ (A), and $O(q^2)$: $R = 4$ (B) growth rates (run SPP2). Note that we choose $\phi = 55°$ for the initial perturbations.

excellent agreement with the analytical results. Furthermore, our simulations correctly capture the exponential growth for $R < R_1$ and the oscillatory growth for $R_1 < R < R_2$.

3.1.2 Time asymptotic steady state

The perturbation amplitudes after initial growth are acted upon by the system nonlinearities, which distribute the energy among the various wavenumbers. Finally the system attains a nonequilibrium steady state, whose onset is shown by black-dashed line for the velocity field in figure 3.5(a) and for the polar order parameter field in figure 3.5(b).

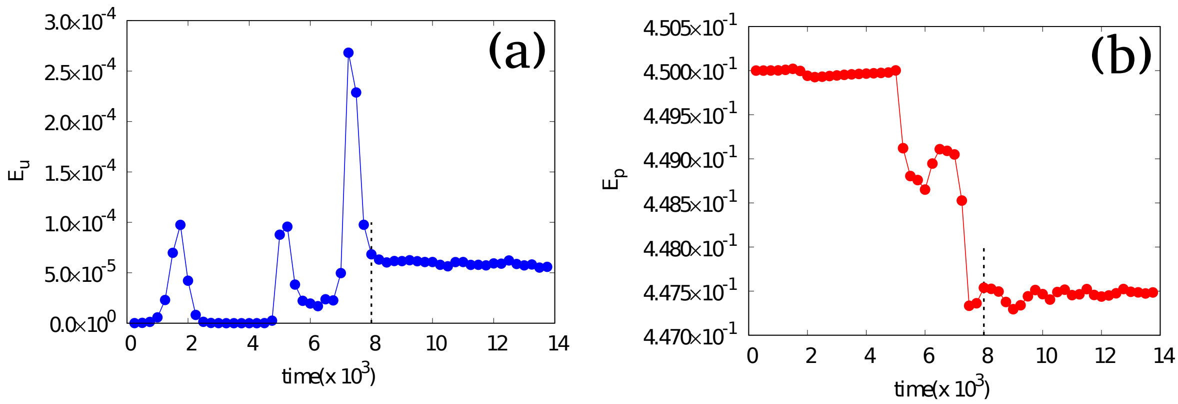

Figure 3.5: Time evolution of total kinetic energy of (a) the velocity field and (b) director field for $R = 0.02$ (SPP2 in Table 3.1). Dashed line indicates the time after which the system has attained nonequilibrium steady state.

3.1.3 Turbulence for $0 < R < R_1$

In figure 3.6(a) we plot a representative snapshot of the magnitude of the director vorticity $|\omega_p|$, where $\boldsymbol{\omega_p} = \nabla \times \boldsymbol{p}$, which shows that it consists of a range of structures of varying sizes without directional bias. This is further evidenced from figure 3.6(b) where we show the two-dimensional projection of the streamlines of the polar order parameter at the same instant. We observe $+1$ defects, marked by black circles and -1 defects marked by red squares. It is important to notify here that these defects are passively advected by the velocity and thus undergo collective dance. This is unlike the half-integer defects in active nematics [4], where the +1/2 defect is inherently motile because of its fore-aft asymmetry. The three dimensional snapshot for the velocity field is shown in figure 3.6(c), and the corresponding streamlines are shown in figure 3.6(d). We see that the turbulent structures are vortices and saddles, which are respectively marked by black circles and red squares similar to the director.

3.1.4 Turbulence for $R > R_1$

We now describe the turbulent structures for $R > R_1$, i.e. when the inertial effects of self-propulsion start competing with the active forces. Figure 3.7(a) shows a steady-state snapshot of the magnitude of the director vorticity. Unlike figure 3.6(a) here we observe large-scale ordered patches. The director streamlines

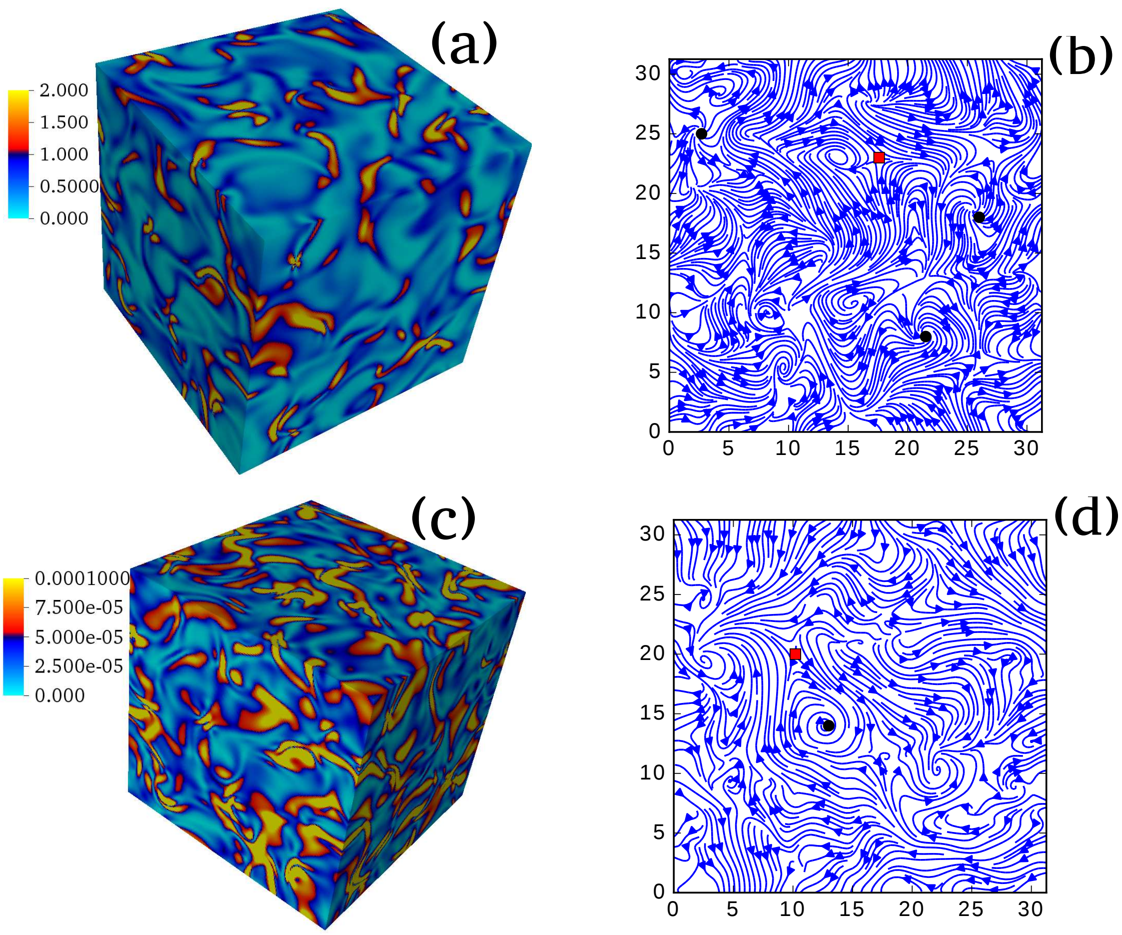

Figure 3.6: Steady-state snapshot of turbulence for $R < R_1$ ($R = 0.01$, run SPP2 in Table 3.1): (a) Pseudocolor plots of director-vorticity magnitude, (b) 2D slice of the snapshot in (a) showing the director streamlines, (c) Pseudocolor plots of the vorticity magnitude of the velocity-field at the same instant, and (d) 2D slice of the snapshot in (c) showing the velocity streamlines.

in figure 3.7(b) makes this more prominent. Here one clearly observes a noisy yet ordered motion and also there are no defects. However, the vortices and saddles which constitute the velocity field still continue to be present here, as observed in figure 3.7(c).

3.1.5 Vorticity PDFs: $R < R_1$ vs $R > R_1$

Figure 3.8 shows the standardised probability distribution function (PDF) for the x component of the vorticity $\boldsymbol{\omega}^u$ of the velocity field, where $\boldsymbol{\omega}^u = \nabla \times \boldsymbol{u}$. For the

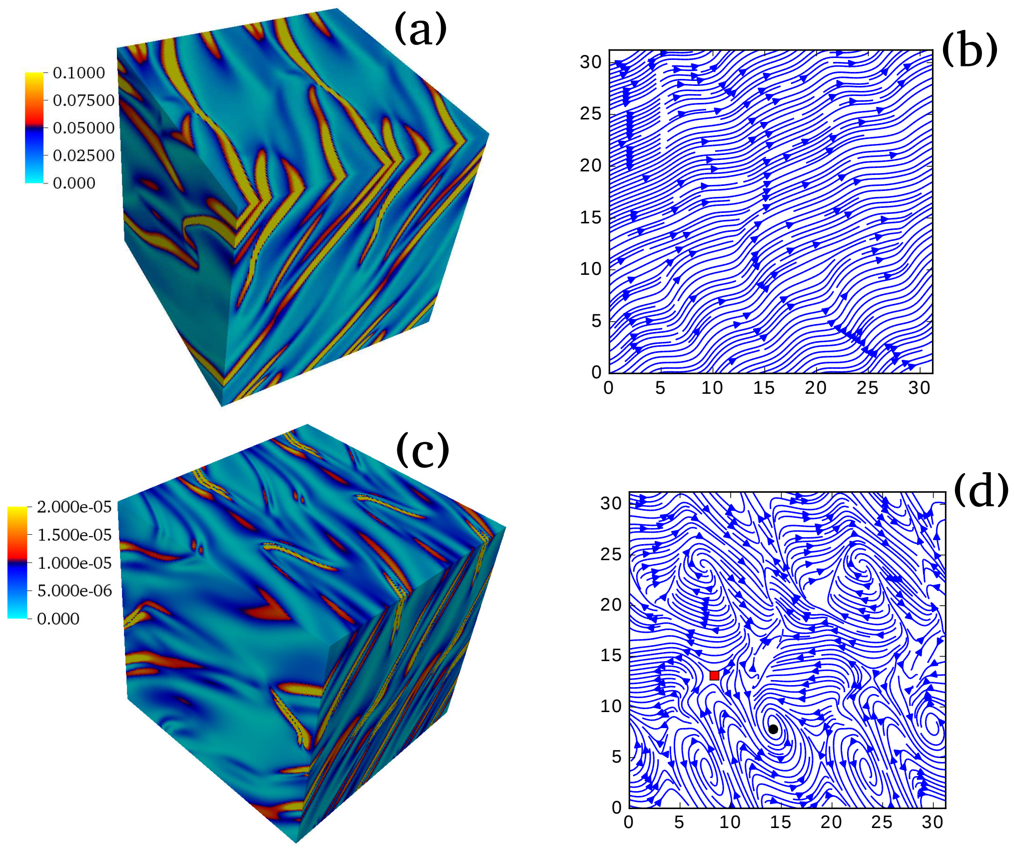

Figure 3.7: Steady-state snapshot of turbulence for $R > R_1$ ($R = 4$, run SPP2 in Table 3.1): (a) Pseudocolor plots of director-vorticity magnitude, (b) 2D slice of the snapshot in (a) showing the director streamlines, (c) Pseudocolor plots of the vorticity magnitude of the velocity-field at the same instant, and (d) 2D slice of the snapshot in (c) showing the velocity streamlines.

velocity field we observe that the tails of the vorticity PDFs depart from Gaussianity for both $R < R_1$ and $R > R_1$, indicating the presence of fine-scale coherent structures. The non-Gaussian departure is greater for $R > R_1$ which, we presume, is due to a more intense dynamics of extreme bursts of vorticity and strain-rates at the small-scales, which occur amidst the 'structured' state consisting of vortices and saddles. The normalized PDFs of the director vorticity $\boldsymbol{\omega}_p = \nabla \times \boldsymbol{p}$ is shown in figure 3.9. Here for both $R > R_1$ and $R > R_1$ we observe sub-Gaussianity at lower vorticity values and a widening at larger values, both these deviations being higher for $R > R_1$. Thus our main conclusion here is the turbulence for $R > R_1$ is more non-Gaussian and thus more intermittent than the one for $R < R_1$. This sug-

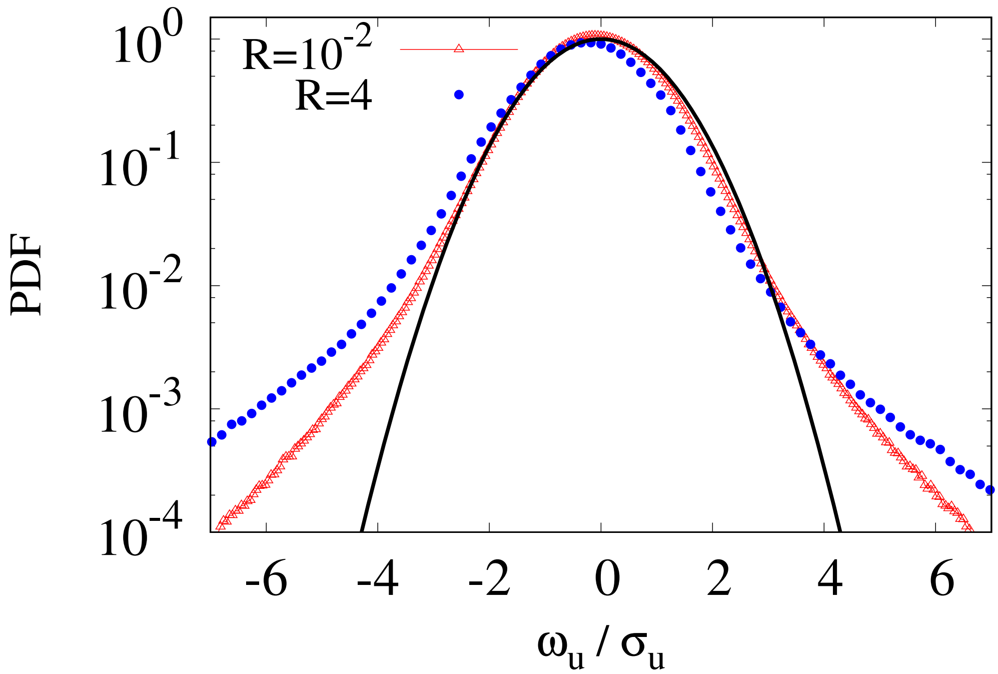

Figure 3.8: Standardised Probability distribution function of vorticity in the the turbulent steady state for $R < R_1$ ($R = 0.01$, run SPP2 in Table 3.1) shown as red lines with triangles vs $R > R_1$ ($R = 2$, run SPP2 in Table 3.1) shown as blue circles. Black line shows the standard normal curve. The x-axis is scaled w. r. t. the RMS value $\sigma_u = \langle \omega_u^2 \rangle$.

gests that the random propagations of fluctuations and moving shock-boundaries amidst an ordered flock, which characterizes the phase-turbulence for $R > R_1$, acts as more violent bursts of extreme-events than the ones generated by the defect dynamics for $R < R_1$. Also the ordered structure of the turbulence for $R > R_1$ is an indicative of phase correlations, which has been established to be a cause of non-Gaussian statistics in nonequilibrium systems [5].

3.1.6 Nonequilibrium phase transition

We now assemble the results on previous sections to unravel an inertia induced phase transition (IIPT). We investigate the morphology and statistical properties of the orientation and flow emerging from the instabilities discussed above. Figure 3.10 shows the typical flow structures observed in our DNS with increasing R

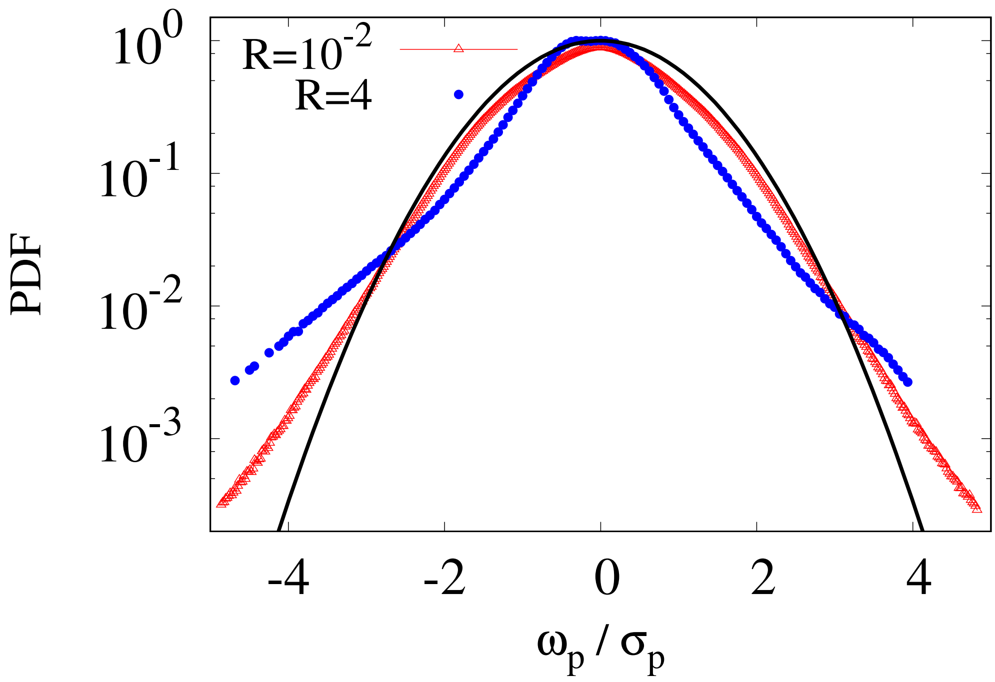

Figure 3.9: Probability distribution function of director vorticity in the the turbulent steady state for $R < R_1$ ($R = 0.01$, run SPP2 in Table 3.1) shown as red lines with triangles vs $R > R_1$ ($R = 2$, run SPP2 in Table 3.1) shown as blue circles. Black line shows the Standard Gaussian curve. The x-axis is scaled w. r. t. the RMS value $\sigma_p = \langle \omega_p^2 \rangle$.

in the statistically steady state. For $0 < R < R_1$, we observe hedgehog defects. The inter-defect spacing grows with increasing R. Unexpectedly, when R increases past the first threshold R_1, a fluctuating but on average aligned state emerges. As we remarked in the Introduction, this is clear numerical evidence that $R = R_1$ marks a nonequilibrium phase transition from a statistically isotropic state to a flock or, in the terminology of spatiotemporal chaos, from defect turbulence to phase turbulence [6, 7, 8]. In the latter state long-wavelength statistical variation of the broken-symmetry variable is present but the amplitude of the order parameter is not destroyed by defects. We have not, however, measured the system-size dependence of the positive Lyapounov spectrum to establish spatiotemporal chaos quantitatively. We now focus on the properties of the nonequilibrium phase transition. In figure 3.11, we plot the magnitude $|\langle \boldsymbol{p} \rangle|$ of the polar order parameter in

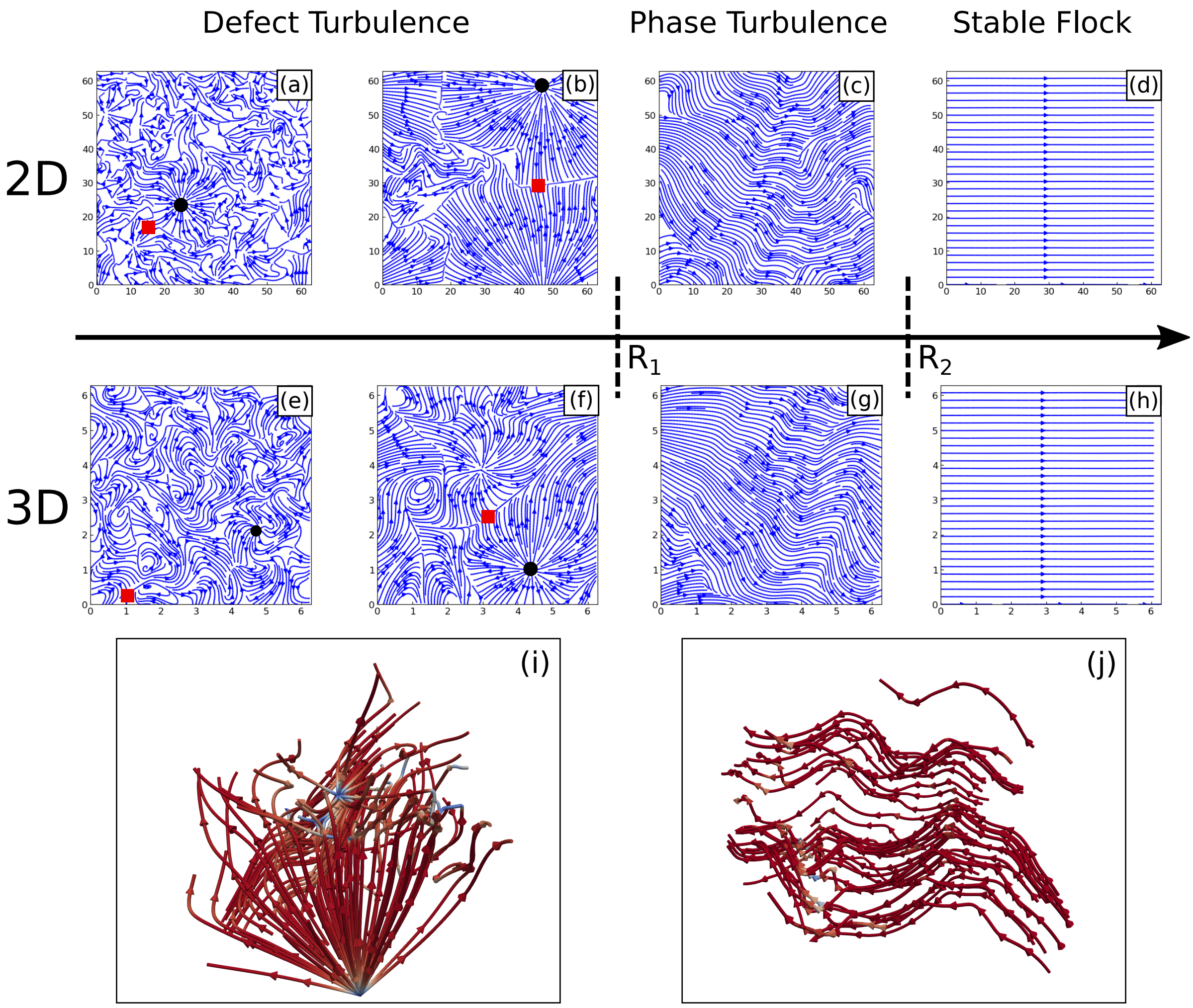

Figure 3.10: Increasing inter-defect distance as function of R. Order parameter streamlines for 2D (run SPP4): (a) $R = 0.1$, (b) $R = 0.25$, (c) $R = 2$, and (d) $R > 12$; streamlines in $y = 0$ plane for 3D (runs SPP1 and SPP3): (e) $R = 0.02$, (f) $R = 0.0625$, (g) $R = 1.25$, and (h) $R > 12$. Typical hedgehogs are marked with filled black circles and red squares indicate saddles. (i) Zoomed in view of the three-dimensional order parameter streamlines showing the complex patterns between a hedgehog-saddle-hedgehog configuration in (f). (j) Three-dimensional nearly ordered configuration in the phase turbulence regime in (g).

the statistically steady state with increasing R, where angle brackets $\langle\cdot\rangle$ denote spatio-temporal averaging. For $R < R_1$, $|\langle \boldsymbol{p} \rangle|$ is consistent with zero. We observe an onset of polar order once R increases beyond $R_1 \equiv 1 + \lambda$. However, a detailed finite-size scaling analysis needs to be undertaken to find the correct scaling near

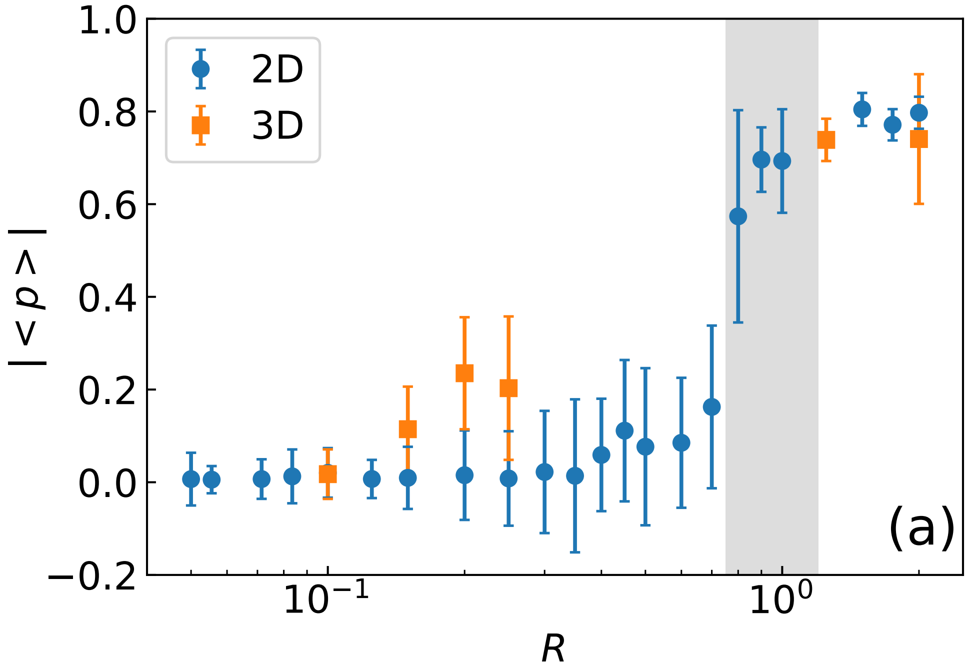

Figure 3.11: Variation of the order parameter $|\langle \boldsymbol{p} \rangle|$ with R for our 2D and 3D simulations (see Table 3.1), with the shaded region indicating the transition regime around $R = R_1$ as predicted by the linear stability analysis. For each of the data point, the spatio-temporal average is calculated from ~ 80 statistically independent realizations and the unit standard deviation about the average is shown as the error-bar.

the critical region. In the defect-turbulence regime, we study the steady-state longitudinal correlation function $C(r) = \langle \boldsymbol{p}_r(\boldsymbol{x}) \cdot \boldsymbol{p}_r(\boldsymbol{x} + \boldsymbol{r}) \rangle / \langle \boldsymbol{p}_r(0)^2 \rangle$, scaled to unity for $\boldsymbol{r} = 0$, where $\boldsymbol{p}_r = \boldsymbol{p} \cdot \hat{\boldsymbol{r}}$. We plot the correlation function $C(r)$ versus r in figure 3.12 and evaluate the correlation length by fitting an exponential decay $\exp(-r/\xi)$ to the tail of $C(r)$ [1]. We see that the correlation functions for different values of $R < R_1$ fall on a single curve plotted against r/ξ. Moreover, from Fig. 3.13 ξ grows and possibly diverges as $R \to R_1$; our limited data points are consistent with an exponent of unity.

[1]The value of ξ obtained from the fit is comparable to the one obtained using the definition $\xi \equiv \int_0^{\mathcal{L}/2} C(r) dr$

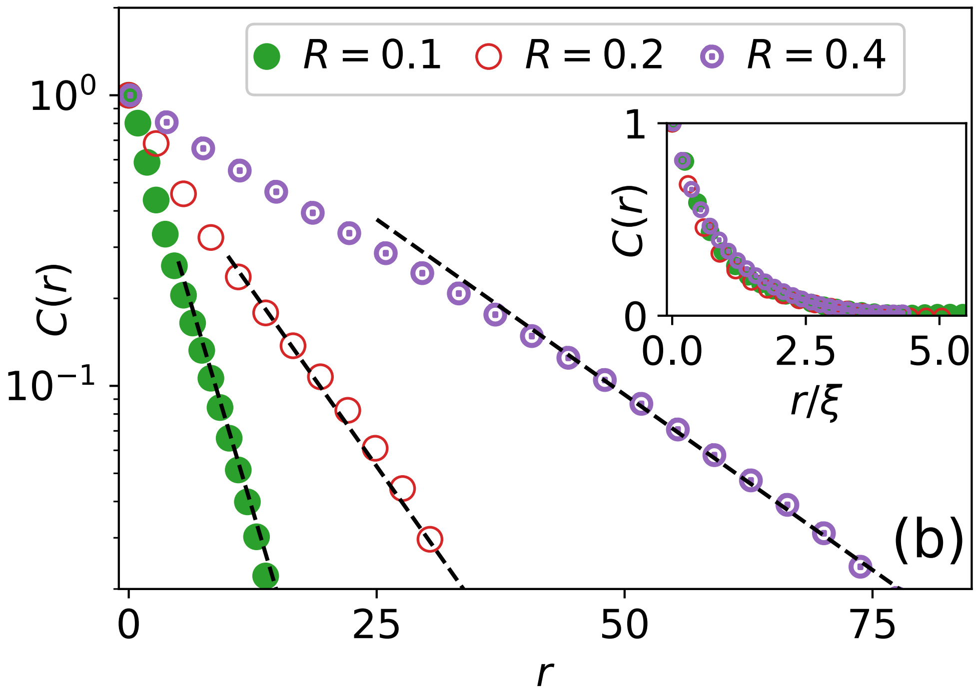

Figure 3.12: Semilog plot of the correlation function $C(r)$ versus r for $R = 0.1, 0.2,$ and 0.4 ($R < R_1$, run SPP4). The dashed line indicate the exponential fit. Inset: Collapse of steady state longitudinal correlation function (LCF) when distance is scaled with the correlation length.

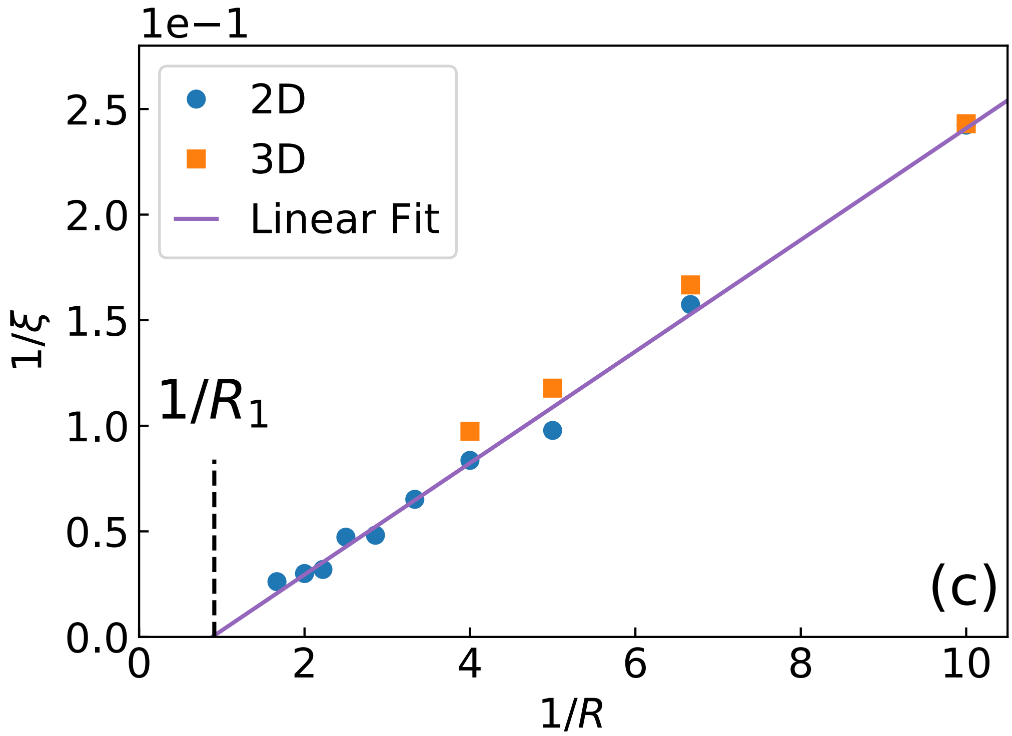

Figure 3.13: Plot of inverse correlation length $1/\xi$ versus $1/R$. Continuous purple line shows the linear fit to 2D data. Note that from the intercept of the linear fit on the horizontal axis we conclude that the correlation length diverges around $R \approx R_1$.

3.1.7 Energy spectrum

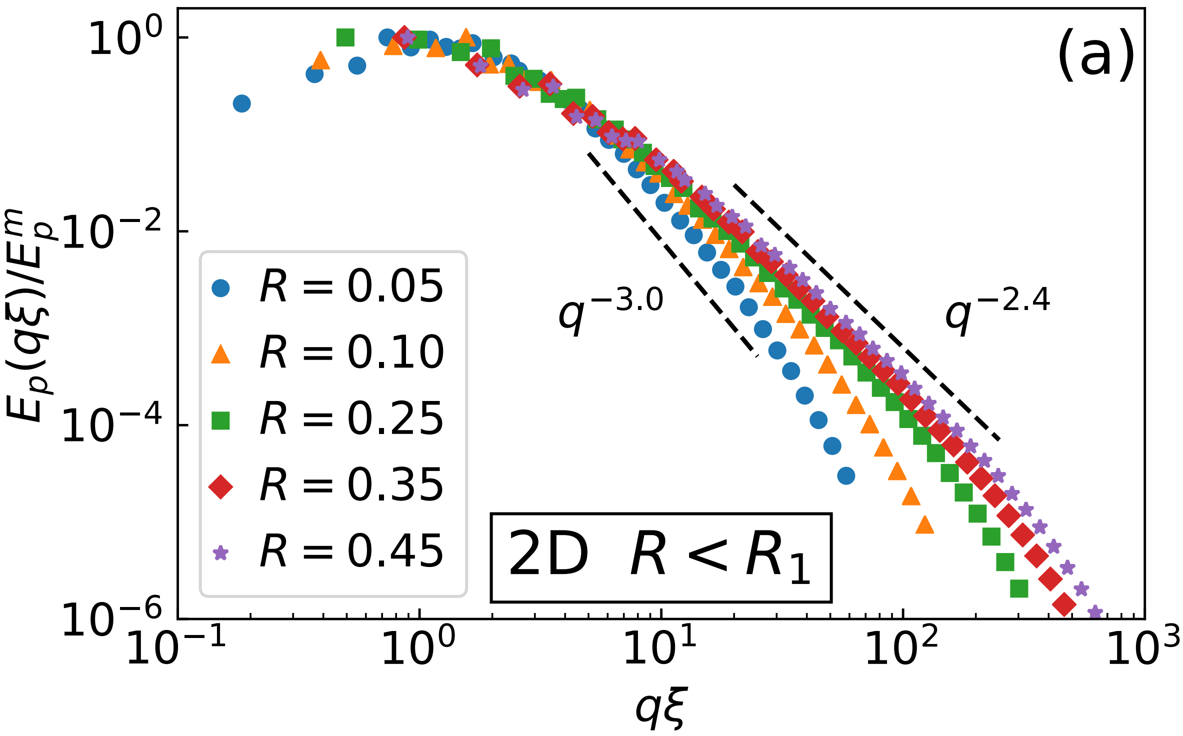

Figure 3.14: Order parameter energy spectrum $E_p(q)$ for different values of R for two-dimensional active suspension [runs SPP4]. For $R < R_1$ and $q\xi > 1$, we observe $E_p(q) \sim q^{-2.9}$ for small R and the slope marginally decreases to $q^{-2.4}$ as R approaches R_1.

Guided by the practice in hydrodynamic turbulence, we define the shell-averaged energy spectra

$$
\begin{aligned}
E_u(q) &= \sum_{q-1/2 \leq \boldsymbol{m} < q+1/2} |\boldsymbol{u}_{\boldsymbol{m}}|^2, \text{ and} \\
E_p(q) &= \sum_{q-1/2 \leq \boldsymbol{m} < q+1/2} |\boldsymbol{p}_{\boldsymbol{m}}|^2,
\end{aligned}
\tag{3.7}
$$

where $\boldsymbol{u}_m$ and $\boldsymbol{p}_m$ are the Fourier coefficients of the velocity $\boldsymbol{u}$ and order parameter $\boldsymbol{p}$ fields. The behaviours of $E_p(q)$ and $E_u(q)$ for a range of values of R are displayed in Figs. 3.14, 3.15, 3.16, 3.17 and Figs. 3.18 and 3.19. We observe that for $R < R_1$, the spectrum peaks around $q\xi \sim 1$. For $q\xi > 1$, $E_p(q) \sim q^{-\Delta}$ with $\Delta = 3$. We observe a gradual decrease in the exponent Δ from 3 to 2.4 as R approaches R_1. We emphasize that the quoted exponent values are empirically determined by

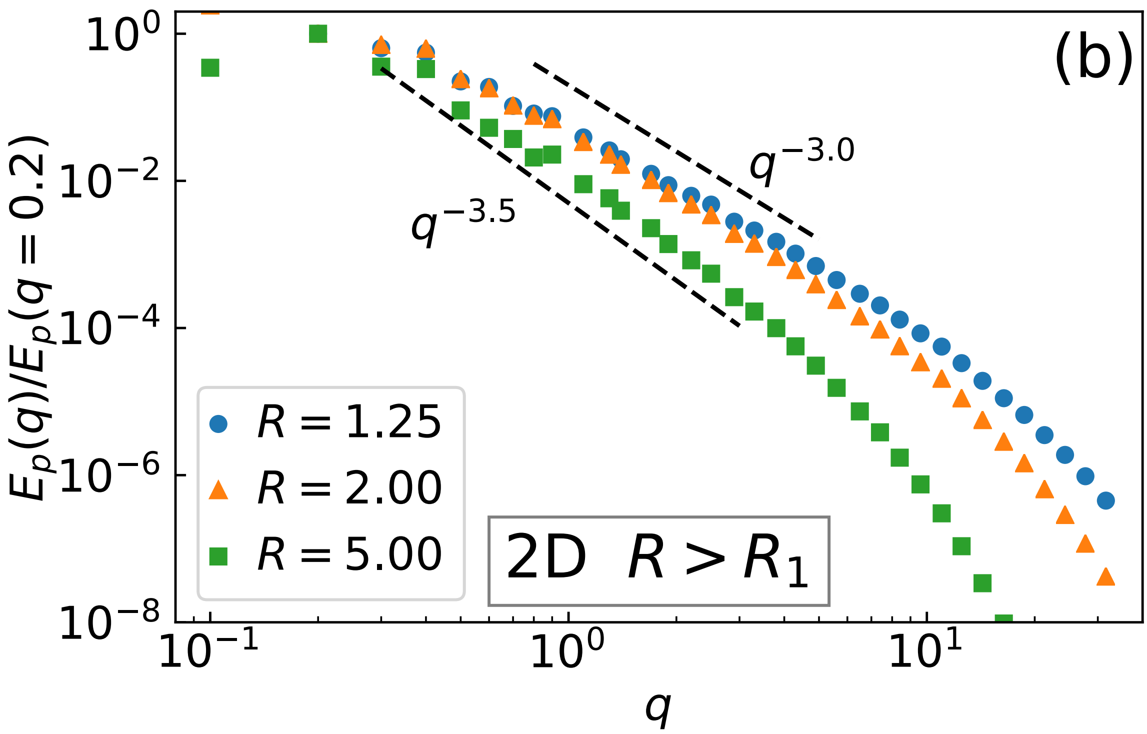

Figure 3.15: Order parameter energy spectrum $E_p(q)$ for different values of R for two-dimensional active suspension [runs SPP4]. For $R_1 < R < R_2$, $E_p(q) \sim q^{-3}$ for $R = 1.25$ and the slope increases to $q^{-3.5}$ for $R = 5$.

conservatively selecting a dynamic range of wavenumbers away from the smallest $\sim 1/L$ and the largest, viz., $q_K \equiv 2\pi/\ell_K$ where elasticity dominates. In the phase-turbulence regime, $R_1 < R < R_2$, we observe $E_p(q) \sim q^{-3}$ for R close to R_1. As R approaches R_2, the effect of fluctuations decrease and we observe a systematic steepening of the slope (Δ). In (3.1) we expect the dominant balance to be between acceleration and activity as the Reynolds number obtained by comparing the advective and viscous terms, based on the root-mean-square hydrodynamic velocity, is small ($\mathrm{Re} \equiv \rho u_{rms}\xi/\mu \leq 0.5$) [2]. We therefore expect for small q, $\omega u_q \sim \sigma_0 q E_p(q)$. Using $\omega \sim v_0 q$ [see Eq. (3.3)] we get, $E_u(q) \sim (\sigma_0/v_0)^2 E_p(q)^2$. The plot in figure 3.18 shows good agreement between $E_u(q)$ obtained from our DNS and the prediction above for small q. For large $q > 2\pi/\ell_\sigma$, we expect viscous dissipation to be dominant and therefore, similar to dissipation range in hydrodynamic turbulence, we expect

[2] We have verified that the results of our DNS do not change if the advective nonlinear term in Eq. (3.1) is absent.

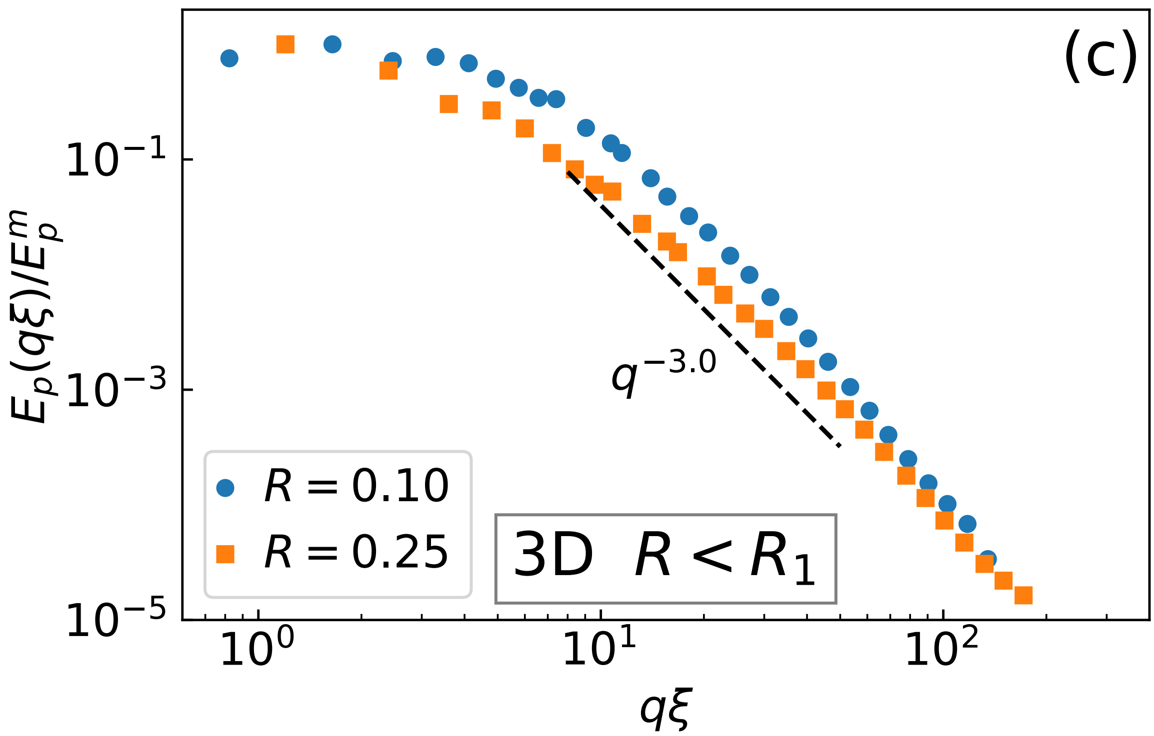

Figure 3.16: Order parameter energy spectrum $E_p(q)$ for different values of R for three dimensional active suspension [runs SPP3]. For $R < R_1$ and $q\xi > 1$, we observe $E_p(q) \sim q^{-2.9}$ for small R and the slope marginally decreases to $q^{-2.4}$ as R approaches R_1.

an exponential decay in the energy spectrum $E_u(q) \sim \exp(-ak^{\delta})$ [9, 10]. From our numerical simulations, we find $\delta = 1$.

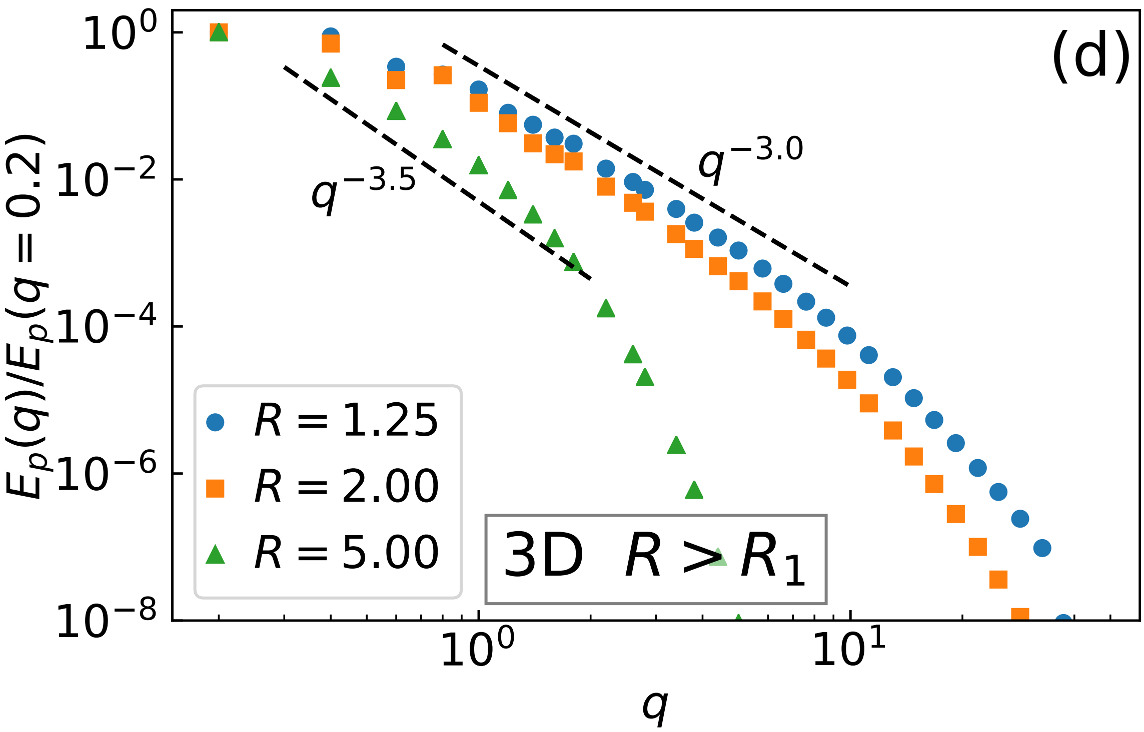

Figure 3.17: Order parameter energy spectrum $E_p(q)$ for different values of R for three dimensional active suspension [runs SPP3]. $E_p(q) \sim q^{-3}$ for $R = 1.25$ and the slope increases to $q^{-3.5}$ for $R = 5$.

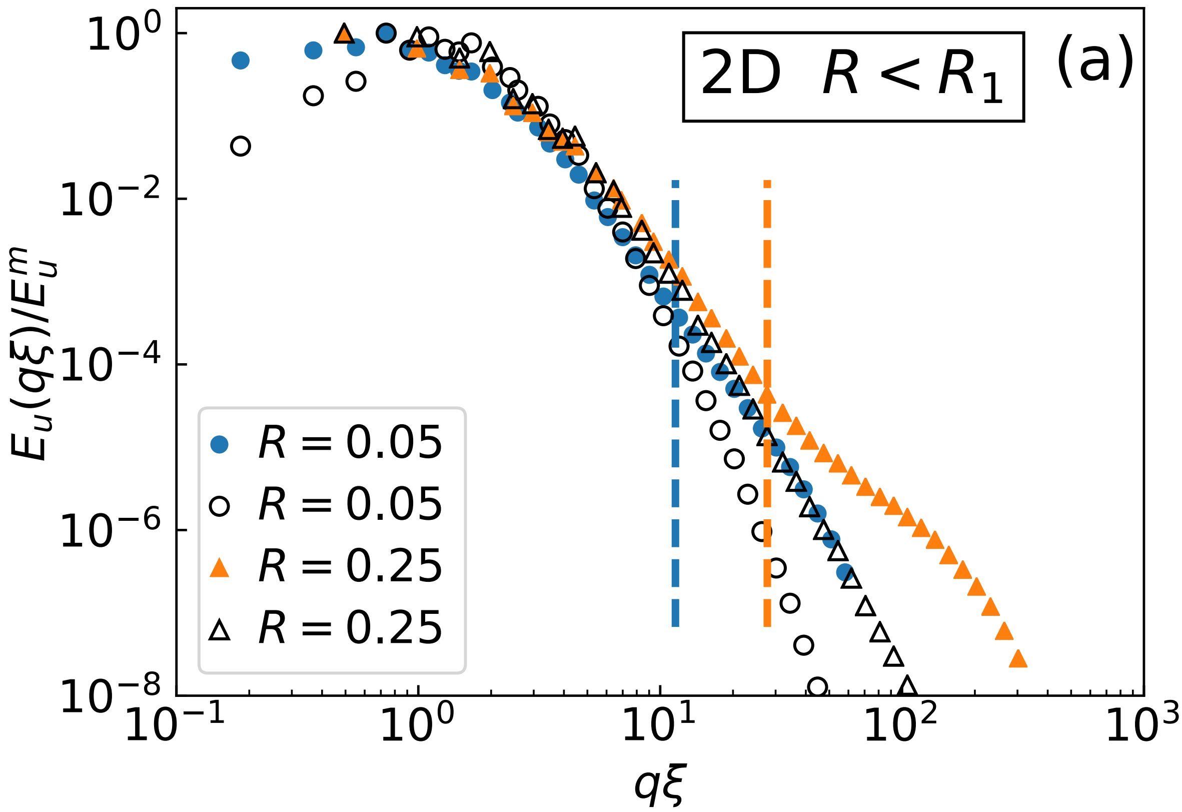

Figure 3.18: Kinetic energy spectrum $E_u(q)$ for different values of R for 2D active suspension[runs SPP4] for $R < R_1$. Similar to order parameter spectrum we observe power-law behavior for $1 < q\xi < q_\sigma\xi$, where $q_\sigma \equiv 2\pi/\ell_\sigma$. For small-$q$, we find a good agreement between the energy spectrum and the prediction $E_u(q) \sim [E_p(q)]^2$ (unfilled symbols). For different values of R, dashed vertical lines (with same color as markers) are drawn at $q = q_\sigma$.

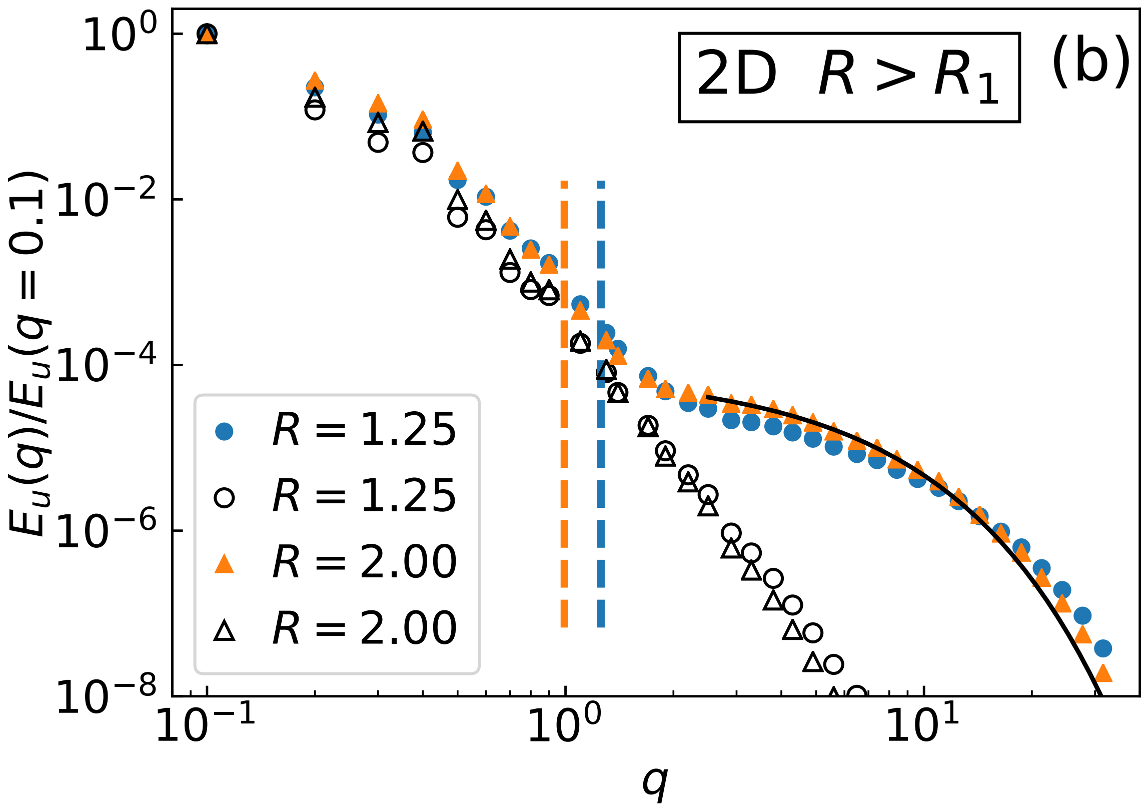

Figure 3.19: Kinetic energy spectrum $E_u(q)$ for different values of R for 2D active suspension[runs SPP4] $R > R_1$. Similar to order parameter spectrum we observe power-law behavior for $1 < q\xi < q_\sigma\xi$, where $q_\sigma \equiv 2\pi/\ell_\sigma$. For small-$q$, we find a good agreement between the energy spectrum and the prediction $E_u(q) \sim [E_p(q)]^2$ (unfilled symbols). For $R > R_1$ and large-q ($q > q_\sigma$) the energy spectrum shows an exponential decay $E_u(q) \sim \exp(-0.29q)$ (black line). For different values of R, dashed vertical lines (with same color as markers) are drawn at $q = q_\sigma$.

3.1.7.1 A note on grid convergence

Having discussed the phase transition dynamics we now address the optimal grid resolution requirement for a particular value of R. This is a challenging computational issue for our problem for the reason described as follows: For the defect turbulence at $R < R_1$, the correlation length imposes the characteristic length scale ξ upon the system as we discussed in the previous section. As R is increased towards values closer to R_1, this characteristic length-scale increases. This demands larger computational box-sizes to correctly capture the correlation length, and simultaneously fine enough grid-spacing in order to adequately resolve the small-scale dynamics for length-scales $\ell < \xi$. On the other hand the phase turbulence for $R > R_1$ is defect-free, but here the large-scale ordered dynamics requires large computational box sizes with adequate grid-spacing to resolve the small-scale noisy fluctuations. Considering all these criteria we find that that for a box-size $\mathcal{L} = 10\pi$ the optimal grid-resolution is $N = 320$ for $R < R_1$ and 160 for $R > R_1$, as shown in the power-spectra in figures 3.20 (a) and (b). We thus present all our computational results at resolutions equal to or higher than this. An adequate representation of the nonequilibrium phase transition using only three-dimensional simulations is thus computationally expensive for us. We therefore present most of our results in two dimensions, in view of the fact that this doesn't alter our essential statistical conclusions, as demonstrated in the previous section.

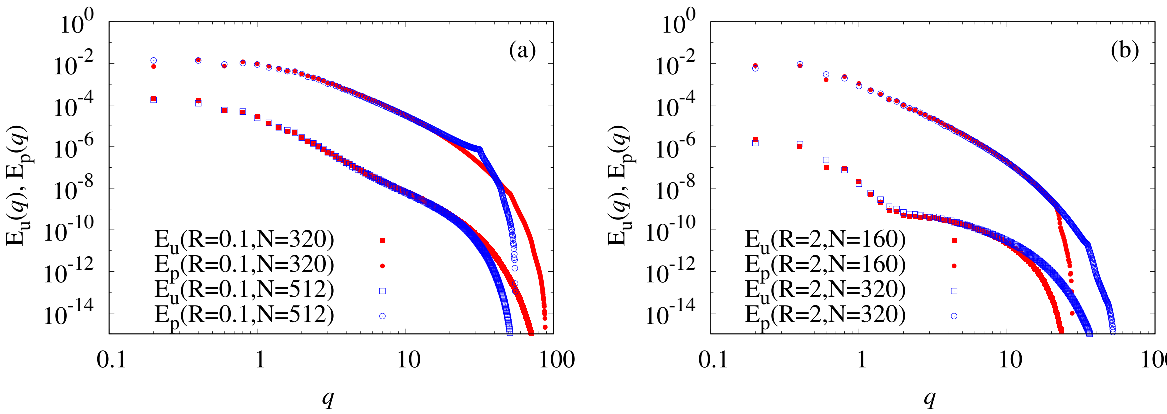

Figure 3.20: Grid convergence of numerical results for the steady-state power spectrum of the velocity and order parameter fields in the turbulent steady state, shown for (a) $R = 0.1$ and (b) $R = 2$ (SPP3 in Table 3.1).

3.2 Extensile versus contractile turbulence

In the last chapter we have discussed that extensile suspensions are dominantly unstable to twist-bend distortions whereas contractile suspensions are always unstable to splay distortions. We now compare the turbulence in an extensile versus contractile suspension with identcal R and thus an almost identical range of unstable modes. In figure 3.21 we show the dispersion curves for the extensile (dashed line) and the contractile (continuous line) system.

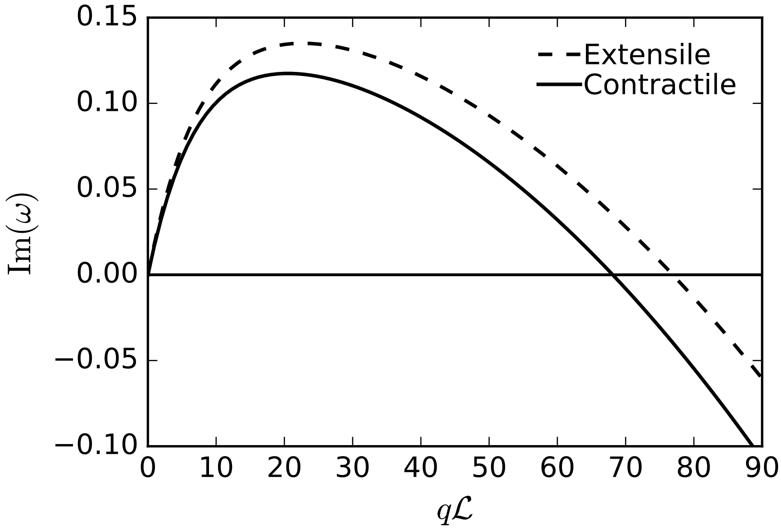

Figure 3.21: Dispersion curves for the growth rate of the most unstable modes in extensile vs contractile systems, for $\phi = 55°$. Parameters for both correspond to $R = 0.005$ (SPP1 in Table 3.1)

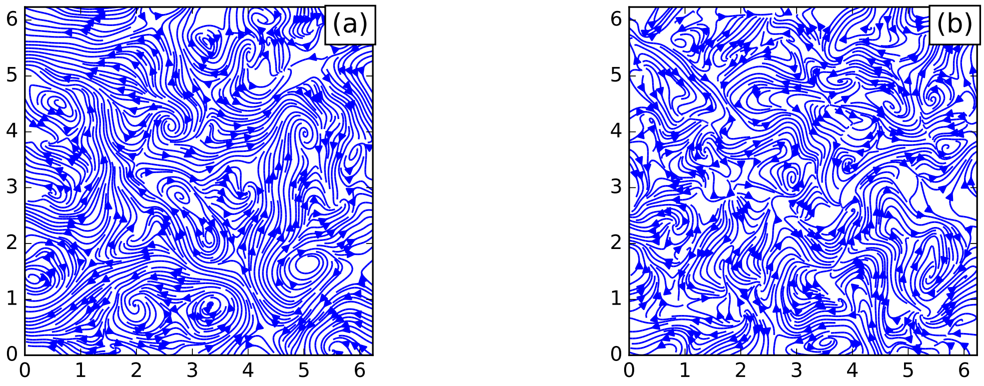

Figure 3.22: (a) Velocity streamlines and (b) Order parameter streamlines for extensile suspension projected on $z = 0$ plane for $R = 0.005$ (SPP1 in Table 3.1).

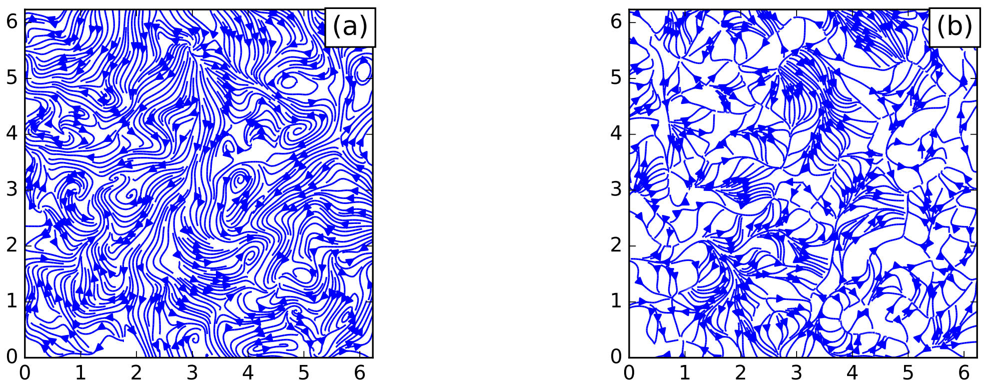

Figure 3.23: (a) Velocity streamlines and (b) Order parameter streamlines for contractile suspension projected on $z = 0$ plane for $R = 0.005$ (SPP1 in Table 3.1).

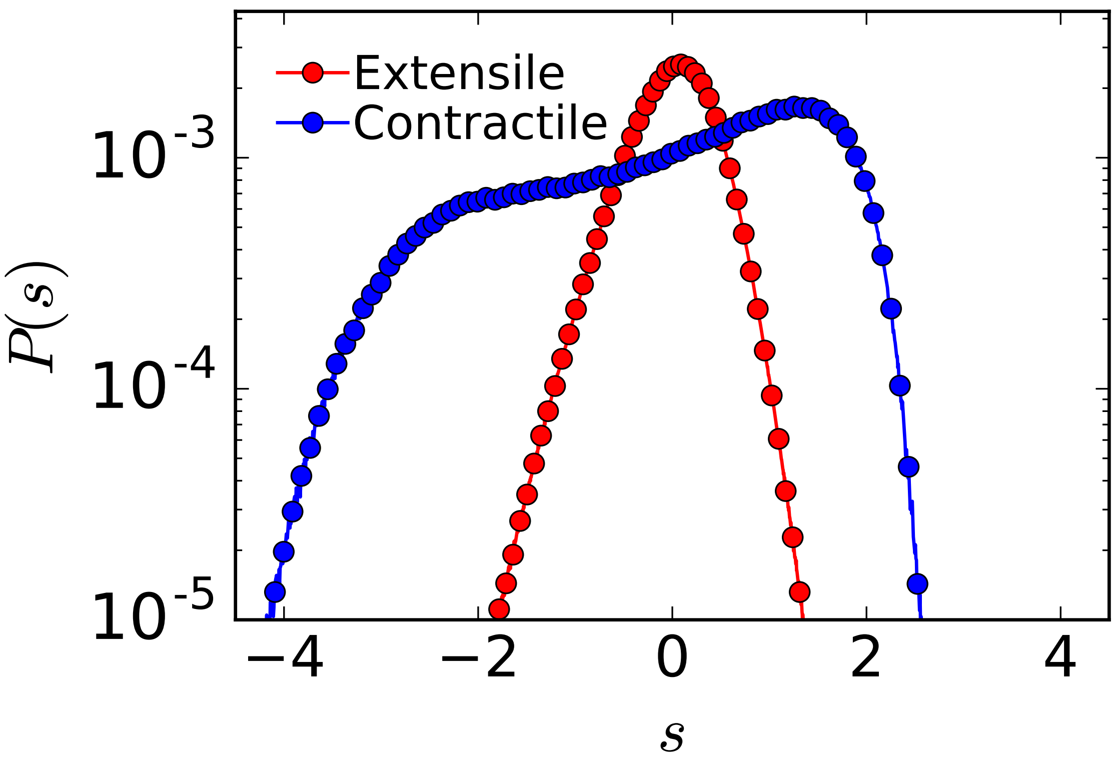

Figure 3.24: Splay PDFs for extensile vs contractile turbulence. Extensile data corresponds to $R = 0.005$ (SPP1 in Table 3.1).

3.2.1 Distortion Statistics

We show the PDF of splay distortions ($s = \nabla \cdot \boldsymbol{p}$) for the extensile system (red dots) vs contractile system (blue dots) in figure 3.24. We find that the contractile turbulence has a richer content of splays than the extensile system. In figure 3.25 we compare the PDF of twist distortions $t = \boldsymbol{p} \cdot (\nabla \times \boldsymbol{p})$ between the two. We observe that extensile turbulence has prominently higher content of twists. The explanation for this is rooted in the linear stability results described in the previous chapter. Recall that the most unstable modes for the extensile systems are the twist-bend modes. On the other hand contractile systems are only splay unstable. Thus the dominant failure modes also show up as the most abundant form of distortion in the corresponding turbulence. This qualitatively explains the form of the PDF.

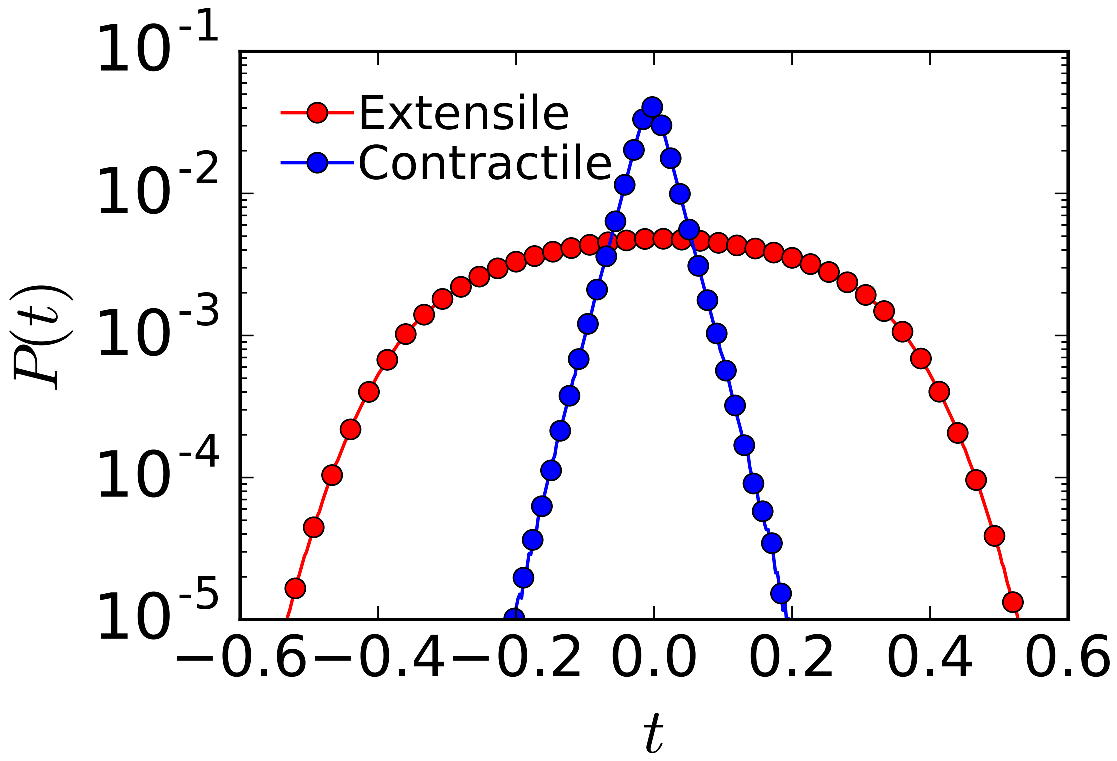

Figure 3.25: Twist PDFs in extensile vs contractile turbulence. Extensile data corresponds to $R = 0.005$ (SPP1 in Table 3.1).

3.2.2 Topological structures

A quantitative way of characterizing topologically invariant structures (which remain unaltered by coordinate transformation) in turbulence is to calculate the joint PDF of the invariants of the velocity gradient tensor[11, 12]. The basic principle involved in the computation of these strucure is as follows: for a three dimensional vector field $\boldsymbol{f}$ the eigen-values of the gradient tensor $A_{ij} = \partial f_i/\partial x_j$ at any point gives idea on the local flow structure around that point. In three dimensions, the characteristic equation for the eigenvalue η has the general cubic form:

$$\eta^3 + s\eta^2 + Q\eta + R = 0. \tag{3.8}$$

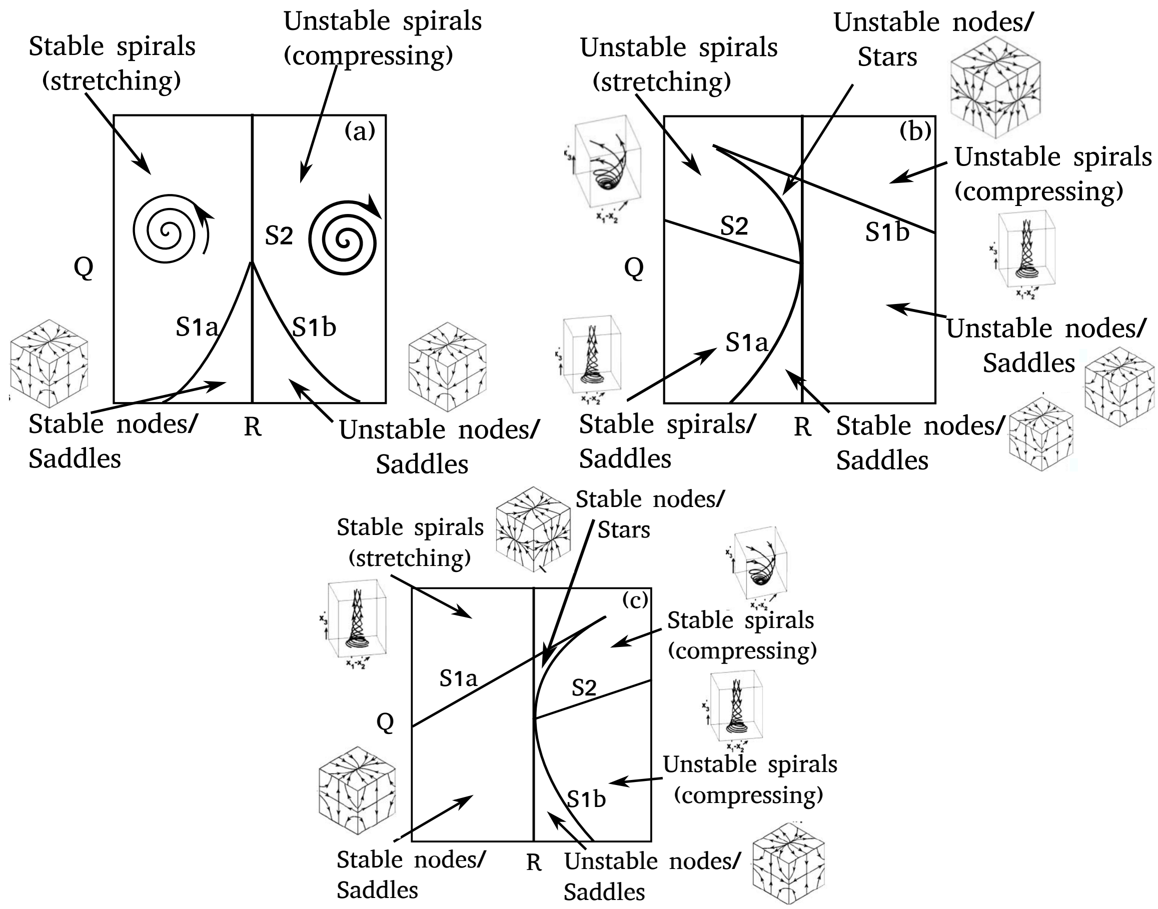

Figure 3.26: Schematic representation of $Q-R$ diagrams:(a)$s=0$,(b)$s>0$, and (c) $s<0$.

The coefficients s,Q and R in Eq. (3.8) are the three topological invariants. These are defined as:

$$s = tr(A) = \eta_1 + \eta_2 + \eta_3, \tag{3.9}$$

$$Q = \frac{1}{2}(s^2 - \mathbf{tr}(A^2)) \tag{3.10}$$

$$R = \frac{1}{3}(s^3 - 3sQ - \mathbf{tr}(A^3)) \tag{3.11}$$

Note that the first invariant s is the splay as discussed above. The local values of s, Q and R determine the signs of the real and/or imaginary components of the roots (eigenvalues) η and hence the local flow structure. The zones of real and complex roots can be distinguished by the discriminant of Eq. (3.8) which can be splitted

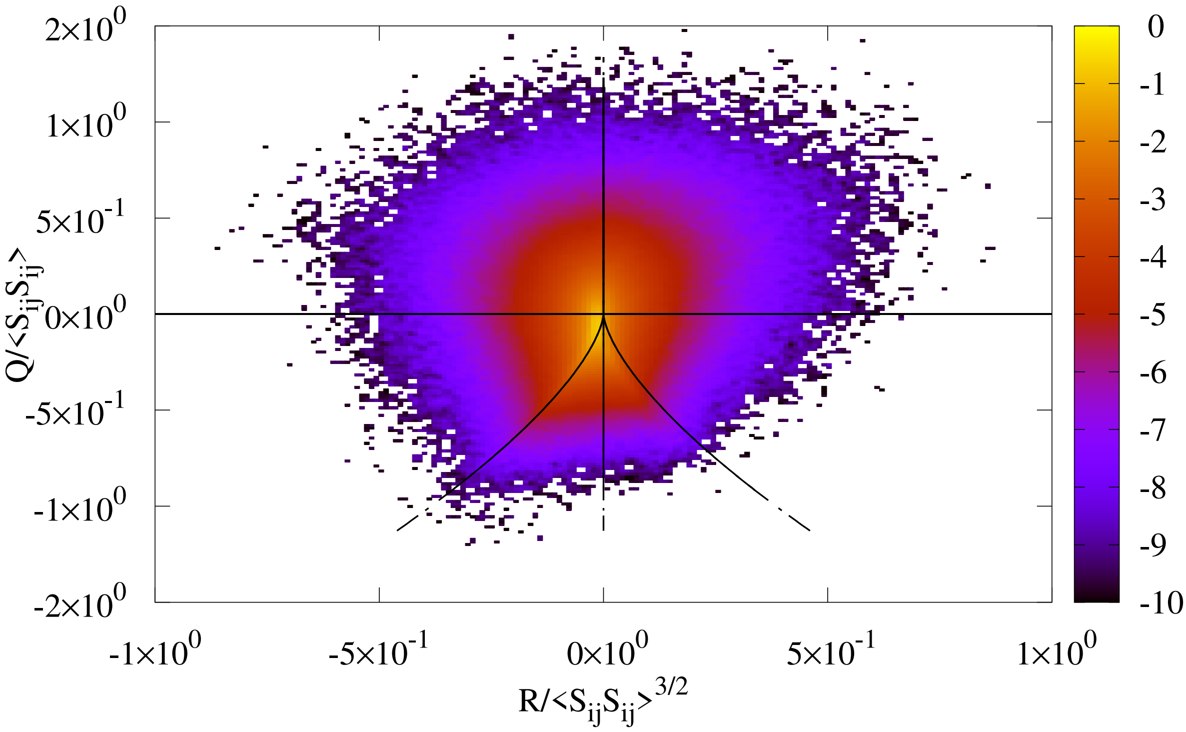

Figure 3.27: $Q - R$ plot of the velocity field for extensile turbulence. Parameters: $R = 0.005$ (SPP1 in Table 3.1).

into two surfaces $S1a$ and $S1b$ having the following equations:

$$S1a : 1/3s(Q - 2/9s^2) + 2/27(s^2 - 3Q) + R = 0 \tag{3.12}$$

$$S1b : 1/3s(Q - 2/9s^2) - 2/27(s^2 - 3Q) + R = 0 \tag{3.13}$$

In the region of complex roots, the purely imaginary ones can be defined by the surface $S2$ which has the equation:

$$R + Qs = 0 \tag{3.14}$$

Thus one can obtain a detailed idea on the distribution of topological structures from the joint probability distribution functions of s, Q and R alongwith the discriminants $S1a$, $S1b$ and $S2$. A schematic representation of the various topological structures corresponding to all possible values of s, Q and R is shown in figure 3.26.

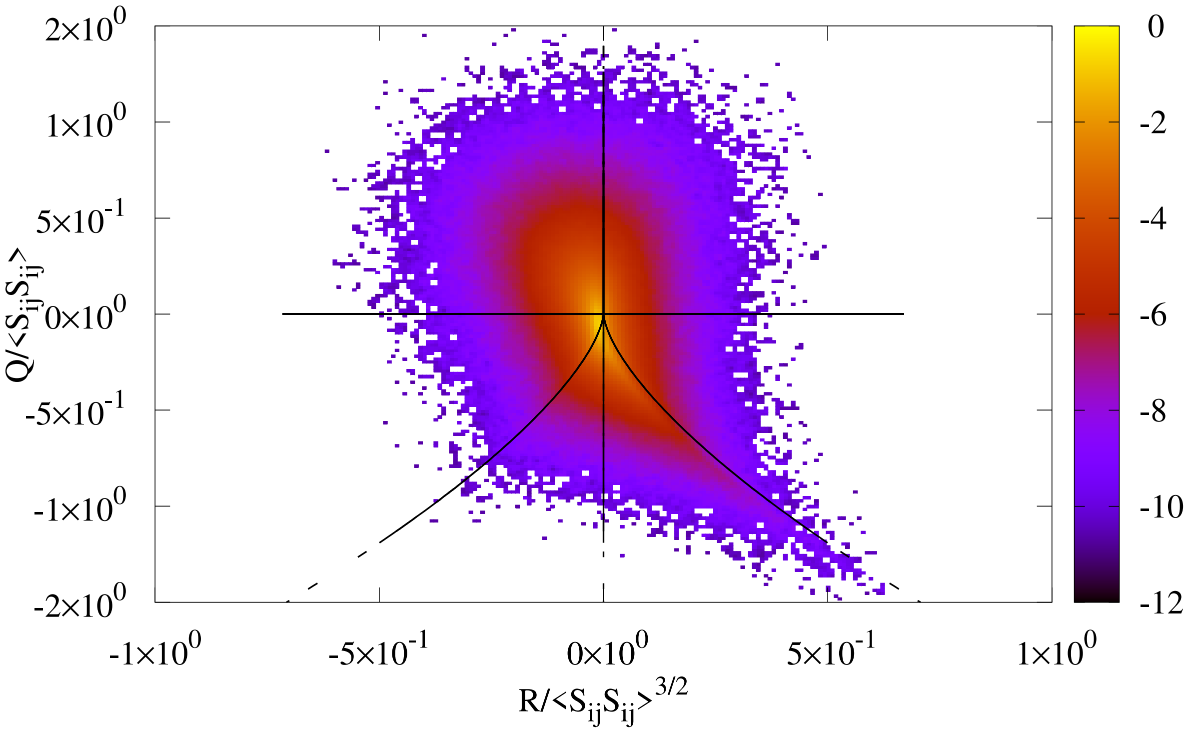

Figure 3.28: $Q - R$ plot of the velocity field for contractile turbulence. Parameters: $R = 0.005$ (SPP1 in Table 3.1) with active stress sign reversed.

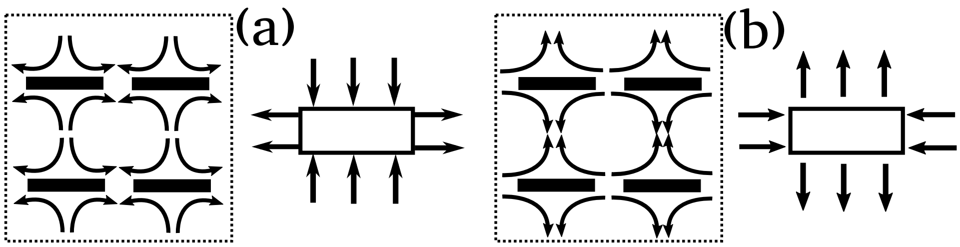

Figure 3.29: Schematic diagram illustrating how (a) the flow generated by a collection of extensile active particles experiences uniaxial strain, and (b) the flow generated by a collection of contractile active particles experiences biaxial strain.

3.2.2.1 Velocity

For the active suspension the velocity field is incompressible, thus $s = 0$. Hence the topological structures are completely described by the joint statistics of Q and R as depicted in figure 3.26(a). We plot the joint PDFs of Q and R for the ve-

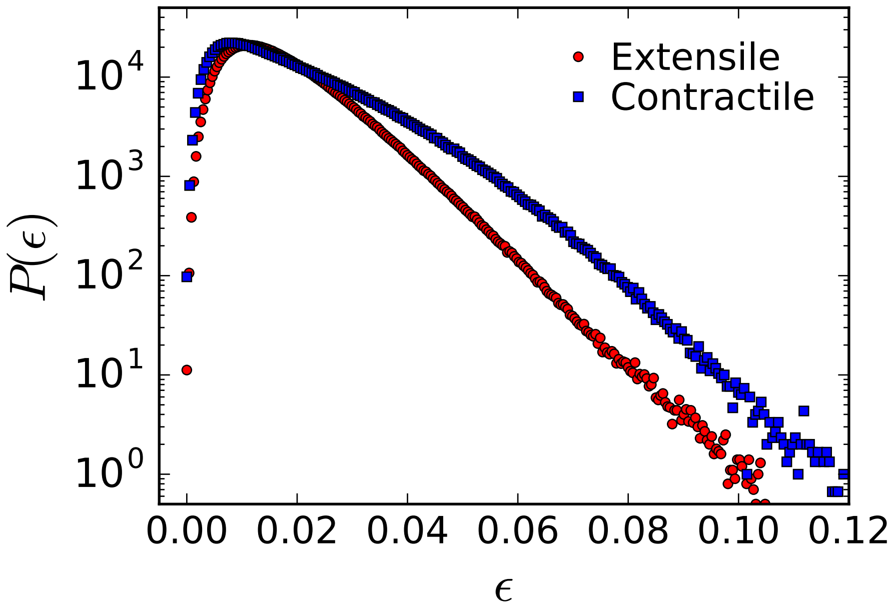

Figure 3.30: K.E. dissipation in extensile versus contractile suspensions for $R = 0.005$ (SPP1 in Table 3.1).

locity field of the extensile system in figure 3.27 and the contractile system in figure 3.28. For both we see that there are respectable proportions in all quadrants similar to the underdeveloped turbulence discussed in [13]. The majority of the areas are enclosed between the $S1a$ and $S2$ for $R < 0$ and between $S1b$ and $S2$ for $R > 0$. This suggests that spiral vortices constitute majority of the flow-structures, which is clearly evident from their representative visual snapshots in figures 3.22(a) and 3.23(a). There is also slight bias towards bottom-left quadrant ($Q < 0, R < 0$) for the extensile system and towards the bottom-right quadrant ($Q < 0, R > 0$) in the contractile system. This indicates that the velocity field in extensile systems are predominantly strained uniaxially, leading to tubular structures, whereas in the contractile system the velocity field mainly experiences biaxial strain. We qualitatively explain this by the schematic diagrams in figures 3.29(a) and (b). The direction of the flow generated by a collection of extensile active particles indicates that the longer axis (along body length) experiences extensile force whereas the transverse axis faces contractile force. Assuming the flows generated by each particle is axisymmetric, this clearly implies uniaxial

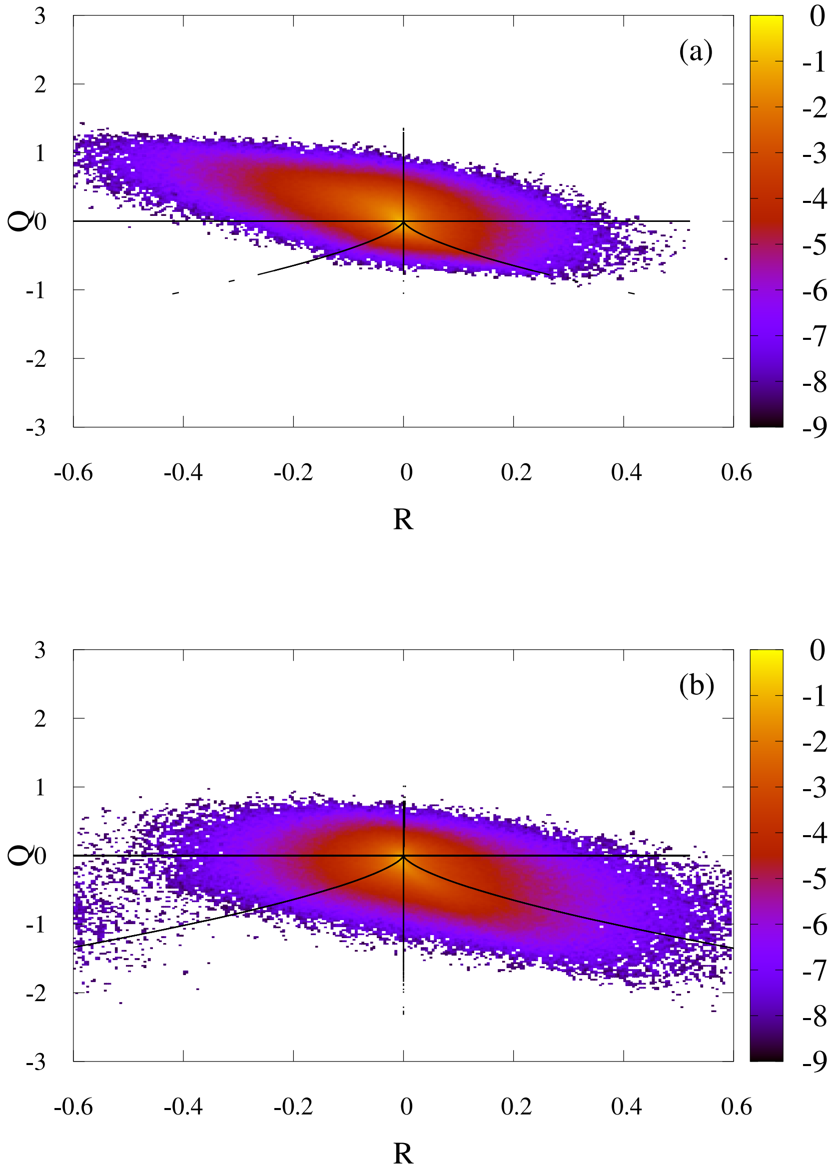

Figure 3.31: $Q - R$ plot of the director field for extensile turbulence for (a) $s > 0$ and (b) $s < 0$. $s1a$ and $s1b$ are drawn for $s = 0$. Parameters: $R = 0.005$ (SPP1 in Table 3.1).

strain in three dimensions. The same logic applied on a collection of contractile swimmers explains the biaxial strain on the velocity field in three dimensions. Further, the relatively longer tail of the contractile system in the region $Q < 0$ is an indicative that its dynamics is more dissipative than the extensile system. To further support this, we compare the time averaged PDF of kinetic energy disspi-

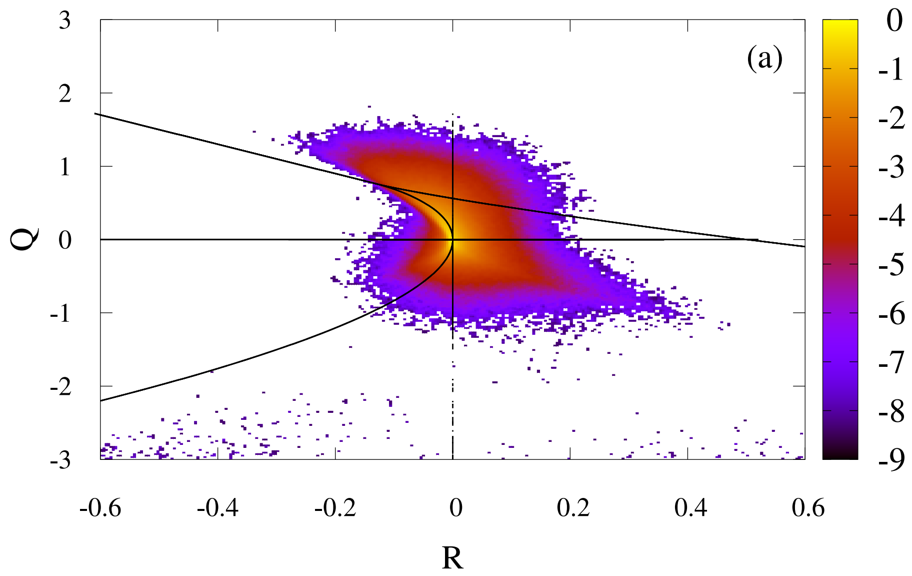

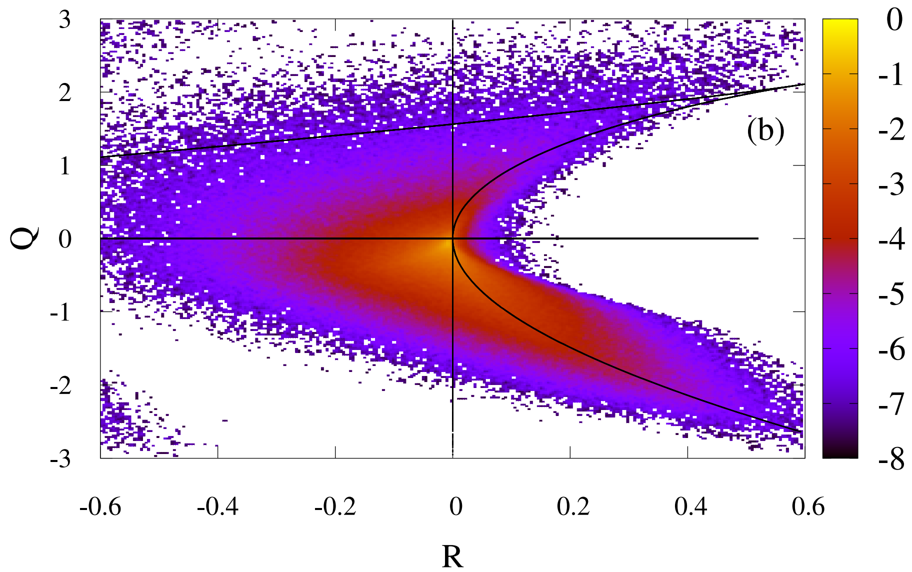

Figure 3.32: $Q - R$ plot of director field for contractile turbulence for (a) $s > 0$ and (b) $s < 0$. $s1a$ and $s1b$ are drawn for $s = 1.5$ in (a) and $s = -2.5$ in (b), corresponding to the modes of the splay curve in figure 3.24. Parameters: $R = 0.005$ (SPP1 in Table 3.1) with active stress sign reversed.

ation rate ϵ between the extensile versus contractile system. Here $\epsilon = 2\nu\langle S : S\rangle$ where ν and S are respectively the kinematic viscosity and the symmetric component of the velocity gradient tensor as defined before. This is shown in figure 3.30, where the extensile system is marked by red circles and the contractile system by blue squares. Clearly we notice higher dissipation rates for the contractile system, thus confirming that the velocity field dynamics of the contractile suspension is more dissipative than the extensile.

3.2.2.2 Polar order

Unlike the velocity field, the gradient tensor $\nabla \boldsymbol{p}$ of the polar order parameter field has non-zero compressibility s. Thus its topological structures are adequately described in terms of the three invariants s, Q and R. Here we study the cumulative PDFs of Q and R in regions with $s > 0$ and $s \leq 0$ and interpret them using the guidelines from figures 3.26(b) and (c) respectively. In figures 3.31 (a) and (b) we respectively show the $Q - R$ distributions for the regions with $s > 0$ and $s \leq 0$ for an extensile system. The discriminant lines $S1a$, $S1b$ and $S2$ for both are drawn for $s = 0.01$ which is the modal value of s as observed in figure 3.24. We see that the regions with $s > 0$ have majority of the area in the top left quadrant, signifying the prominent presence of unstable spirals and unstable source-like structures, which are present in the form of hedgehog defects. An almost equally significant area lie in the 1st and 4th quadrants, signifying the presence of saddle-like structures. The $Q - R$ distributions for regions with $s < 0$ shows that majority of the area lies on the 3rd and 4th quadrants, with a greater proportion in the 4th quadrant. This implies that these regions mainly have saddles, stable nodes and unstable spirals, the last one being present in more significant amounts. For the contractile system, the $Q - R$ distributions for the regions with $s > 0$ and $s \leq 0$ are shown in figures 3.32(a) and (b) respectively. For $s > 0$, The discriminant lines $S1a$, $S1b$ and $S2$ are drawn for $s = 1.5$ which is the modal value for $s > 0$ as observed in figure 3.24. Likewise, for $s < 0$, The discriminant lines $S1a$, $S1b$ and $S2$ are drawn for $s = -2.5$ after which the $P(s)$ vs s curve in figure 3.24 falls off steeply $s \leq 0$. Here we see that the regions with $s > 0$ mostly have stable source-like structures unlike spirals for the extensile. The reason is: contractile turbulence prefers only splay-like structures whereas extensile turbulence can support both bend-twist and splay-like structures, as already explained in our stability results in the previous chapter and also while discussing distortion pdfs in the previous section of this chapter. Thus the director turbulence in extensile systems supports both spirals, which have non-zero curvature and hence are bend-like distortions, and also sources which are splay-like distortions. On the other hand, the director turbulence in contractile systems donot permit spiral-like structures. Thus the dominant structures here are only source-like. The regions with $s < 0$ have saddles and unstable nodes, but the top is biased towards the right, indicating the presence of stable nodes. Note the difference here with 3.31(b) for the extensile system where the top was biased to the left, indicating spirals (which are not allowed here).

3.3 Conclusion

We have presented our computational results on turbulence in compressible active suspensions. In extensile systems we highlight two distinct phases of active turbulence in polar self-propeled particle suspensions-an isotropic defect turbulence and a phase turbulence. We characterize the transition which occurs between these two phases as the relative dominance of the inertial effects of self-propulsion starts to gain importance over active forces. We also show the fundamental differences between extensile and contractile turbulence and show that the allowed topological structures are different between these two. It would be interesting to test these findings in experiments.

Appendix

Pseudospectral Method (PSM)

We discuss the implementation of the pseudospectral method on a one-dimensional nonlinear PDE having the general form:

$$\frac{\partial u}{\partial t} = -\frac{\partial u^2}{\partial x} + f(u) \tag{3.15}$$

on a cubic domain of length $\mathcal{L} = 2\pi$, with the initial condition is $u(x,0) = u_0(x)$. Here $f(u)$ denotes a function linear in u.

Implementing PSM

1. Calculate FFT of $u(x)$: $\hat{u}_q = \int_{\mathcal{L}} u(x)e^{-iqx}dx$, where q ranges from -N/2+1 through 0 to N/2 on a set of grid points 1,2,....,N.

2. Set $\hat{u}_q = 0$ for $q > q_\mathrm{a}$ where q_a = N/3. This is the 2/3rd rule of de-aliasing.

3. Evaluate the linear function in the spectral plane $\hat{f}(u)$.

4. Take iFFT $u(x) = \int_{-q_a}^{q_a} \hat{u}_k e^{iqx} dq$

5. Evaluate the non-linear function in the real plane $\frac{\partial u^2}{\partial x}$. Then calculate its Fourier transform $\left[\frac{\partial u^2}{\partial x}\right]_q$.

6. Time evolve $\hat{u}_q$ in the spectral plane: $\frac{d\hat{u}_q}{dt} = -\left[\frac{\partial u^2}{\partial x}\right]_q + \hat{f}(u)$.

Aliasing error

Say we omit step (2) above. Then step (4) above implies, in the spectral plane, the convolution $\int_l \int_m \hat{u}_l \hat{u}_m e^{i(l+m)x} dl dm$ where $l \in [-km : km]$ and $m \in [-km : km]$; $km = N/2$. Thus, where $|l + m| > N/2$(maxm. spectral resolution),the kernel of the convolution evaluated is $\hat{u}_l \hat{u}_m e^{iNx} e^{i(l+m-N)x}$, where $e^{iNx} = e^{iNn\delta x} = e^{iNn(2\pi/N)} = e^{i2\pi n} = 1$ (since n is ALWAYS an integer), when $l + m > N/2$. Thus the Fourier amplitude of waveno. $l+m$ adds up to the amplitude of $l+m-N$. Same argument goes when $l + m < -N/2$ where the spurious waveno. read is $l + m + N$.

De-aliasing by 2/3rd rule

Lets consider the spectral domain $k \in [-N/2, N/2]$. Let $Ka \in [0 : N/2]$ = cutoff waveno. to avoid Aliasing. Let j, s be two wavenos. s.t. $0 \leq j, s \leq Ka$, and $j + S > N/2$ and hence gets mapped back to $j + s - N$ (reason explained above). We choose the limit Ka such that their maximum possible value of the combination $j + s$ (i.e.$2Ka$, when both $j = s = Ka$) maps back behind $-Ka$, so that the range $[-Ka, Ka]$ is free from spurious wavenos. This implies the following ineqality to hold: $2Ka - N < -Ka$, i.e. $3Ka < N$. Hence $Ka < N/3$ Thus, while computing the ifft of $\hat{u}$, the waveno. components $> N/3$ are set to 0 to avoid aliasing. Now $N/3 = (2/3)(N/2) = (2/3)k_{max}$. This is the $2/3$rd rule of de-aliasing.

4th order Central Differencing

Following are the fourth order central finite-differencing stencils used for discretizing the first and second derivatives:

$$
\begin{aligned}
f_i' &= -\frac{1}{12} f_{i-2} - \frac{2}{3} f_{i-1} + \frac{2}{3} f_{i+1} + \frac{1}{12} f_{i+2} \\
f_i'' &= -\frac{1}{12} f_{i-2} + \frac{4}{3} f_{i-1} - \frac{5}{2} f_i + \frac{4}{3} f_{i+1} - \frac{1}{12} f_{i+2}
\end{aligned}
$$

Slaved Adams-Bashforth for time marching

We illustrate the application of this method for an equation of the form:

$$\frac{df}{dt} = -af + g(t) \tag{3.16}$$

Multiplying both sides by the integrating factor we have, between t and $t+\delta t$:

$$e^{a(t+\delta t)} f(t+\delta t) - e^{at} f(t) = \int_{t}^{t+\delta t} e^{as} g(s) ds \tag{3.17}$$

Similarly between t and $t-\delta t$ we have:

$$e^{at} f(t) - e^{a(t-\delta t)} f(t-\delta t) = \int_{t-\delta t}^{t} e^{as} g(s) ds \tag{3.18}$$

Adding Eqs. (3.17) and (3.18) we finally have:

$$f(t+\delta t) = e^{-2a\delta t} f(t-\delta t) + e^{-a(t+\delta t)} \int_{t-\delta t}^{t+\delta t} e^{as} g(s) ds \tag{3.19}$$

Replacing the integral in the 2nd term in Eq. (3.19) by the Adams-Bashforth scheme we finally have:

$$f(t+\delta t) = e^{-2a\delta t} f(t-\delta t) + \frac{(1-e^{-2a\delta t})}{a} \left[(3/2) f(t) - (1/2) f(t-\delta t)\right] \tag{3.20}$$

Bibliography

[1] *Spectral Methods in Fluid Dynamics*, *Springer Series in Computational Physics*, edited by C. Canuto, M. Y. Hussaini, A. Quarteroni, and T. A. Zang (Springer, New York, 1988).

[2] S. Cox and P. Matthews, J. Comput. Phys. **176**, 430 (2002).

[3] R. A. Simha and S. Ramaswamy, Phys. Rev. Lett. **89**, 058101 (2002).

[4] S. P. Thampi, R. Golestanian, and J. M. Yeomans, Phil. Trans. R. Soc. A **372**, 20130366 (2014).

[5] M. Wilczek, D. G. Vlaykov, and C. C. Lalescu, in *Progress in Turbulence VII*, edited by R. Örlü, A. Talamelli, M. Oberlack, and J. Peinke (Springer International Publishing, Cham, 2017), pp. 3–9.

[6] D. Egolf and H. Greenside, Phys. Rev. Lett. **74**, 1751 (1994).

[7] C. Jayaprakash, F. Hayot, and R. Pandit, Phys. Rev. Lett. **71**, 12 (1993).

[8] H. Chaté and P. Manneville, *Chapter on Phase turbulence in Turbulence* (Springer, Boston, MA, 1995).

[9] L. M. Smith and W. C. Reynolds, Phys. Fluids A **3**, (1991).

[10] U. Frisch, *Turbulence: The Legacy of A. N. Kolmogorov* (Cambridge University Press, Cambridge, 1995).

[11] M. S. Chong, A. E. Perry, and B. J. Cantwell, Physics of Fluids A: Fluid Dynamics **2**, 765 (1990).

[12] S. Suman and S. S. Girimaji, Journal of Turbulence **11**, (2010).

[13] R. Gomes-Fernandes, B. Ganapathisubramani, and J. Vassilicos, Journal of Fluid Mechanics **756**, 252–292 (2014).

[14] M. C. Marchetti and T. N. Liverpool, in *Cell Motility*, edited by P. Lenz (Springer-Verlag, Berlin, 2007).

[15] L. Giomi, M. C. Marchetti, and T. B. Liverpool, Phys. Rev. Lett. **101**, 198101 (2008).

Chapter 4

Population front dynamics in motile bacteria: role of active turbulence

In this chapter we discuss a practical consequence of active turbulence, namely its effect on the dynamics of bacterial colony growth. A shorter version of this chapter was published in Physical Review E.

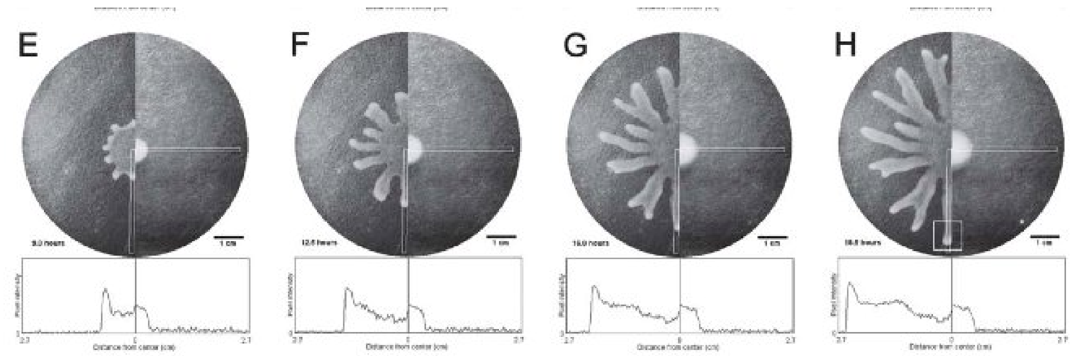

Figure 4.1: Effect of collective motion on the colony growth of *P. aeruginosa PA14* (Fauvart et al. [1]). Left half of each figure shows the growth of wild-type species (capable of collective motion) whereas right half shows the growth of a mutant whose collective motion is hindered.

Bacterial colony spreading on a petri dish is a classical problem in the fields of population biology [2]. In non-motile bacteria the spreading occurs as a combined effect of reproduction and steric repulsions among the individual members [3].

Typically the doubling time of an individual is around an hour, and it takes around 3-4 days for the colony to spread appreciably so that the morphological patterns become observable. Motile bacteria, on the other hand, are seen to perform turbulent-like collective motion at high concentrations, which occurs at a time-scale of a few seconds [4, 5]. Here we explore the effects of this collective motion in motile bacteria on their population dynamics. Figure 4.1 illustrates the vivid difference in the dynamics of colony growth between a non-motile colony and one executing swarming motion, as observed experimentally in [1]. To the best of our knowledge, the colony growth of a motile bacteria in the turbulent phase of collective motion still remains to be explored. Here we use the active-turbulence model by Wensink et al. [4] and couple it with the Fisher equation [6, 7, 8] which is quite an established model for colony growth of non-motile species. We present two minimalistic models to investigate the interplay between population growth and coherent structures arising from turbulence. Using direct numerical simulation of the proposed models we find that turbulence has two prominent effects on the spatial growth of the colony: (a) the front speed is enhanced, and (b) the front gets crumpled. Both these effects, which we highlight by using statistical tools, are markedly different in our two models. We also show that the crumpled front structure and the passive scalar fronts in random flows are related in certain regimes.

4.1 Introduction

Motile bacteria (e.g., *Bacillus subtilis*) colonies form spectacular patterns as they spread on the surface of a Petri dish [8, 9, 10, 11, 12, 13]. The exact pattern depends on a variety of bio-physical conditions such as nutrient and agar concentration [8], motility [9] etc. In a nutrient-rich environment, on a soft or hard agar plate, homogeneous spreading is observed. On a soft-agar plate, at low bacteria densities, spreading happens because bacteria perform run-and-tumble motion [8]. On a hard agar plate, on the other hand, dense colonies of non-motile bacteria spread because individuals push each other as they reproduce [12].

At moderate densities bacteria perform collective motion to form swarms [4, 14]. Such swarming colonies form a variety of patterns such as nearly homogeneous, concentric rings, and dendritic branches [1, 14, 15, 16]. More recent studies have revealed that at high concentrations, bacterial suspensions can show collective motion which strikingly resembles fluid turbulence [4, 17, 18]. The size and speed of typical collective structures is found to be an order of magnitude larger than the speed and size of a bacterium. Remarkably, similar to fluid turbulence the bacteria velocity field shows power-law correlations. Not surprisingly, therefore, recent studies have used Navier-Stokes like equations to successfully model the velocity field of a turbulent bacterial suspension [4, 19].

Earlier numerical studies have modelled colony morphologies by using coupled reaction-diffusion type equations [20, 21]. Homogeneously spreading colonies of non-motile bacteria have been successfully modelled using the Fisher equation Eq. (4.1).

$$\frac{\partial c}{\partial t} = D\nabla^2 c + \mu c \left(1 - \frac{c}{Z}\right). \tag{4.1}$$

Here $c(\boldsymbol{x}, t)$ denotes the concentration of a bacterial colony, μ is the reproduction rate, D is the diffusivity that models the motion that arises because bacteria push each other as they grow and reproduce, and Z is the carrying capacity that we set to 1. Several studies have successfully used modified forms of Eq. (4.1) to study growth of bacteria in different nutrient and agar conditions on a Petri dish. The Fisher equation and its variants have also been used to study competition between two species [11, 12, 20, 22]. Here, $c(\boldsymbol{x}, t)$ should be interpreted as the volume fraction of one of the two colonies. The Fisher equation coupled to the Navier-Stokes equation has also been used successfully to study the coupling between hydrodynamics and chemistry [23, 24].

How does the collective motion of bacteria modify the spreading of a colony? For swarming vortex morphotype colonies [25], modelling the collective velocity field is essential to observe the correct spreading pattern [26, 27]. However, to the best of our knowledge, there are still no experimental studies on the growth of colonies in the recently found regime of bacterial turbulence. In this paper we undertake, for the first time, an exploratory study to investigate the role of turbulent-like collective motion on colony spreading. Following the classical work of Fisher [6], we assume abundance of nutrients and homogeneous environment.

We present two minimalistic models to numerically investigate the spreading of a dense bacterial suspension that performs turbulent-like collective behaviour. Our study shows that the collective motion: a) speeds up the spreading of a colony, and b) the colony front gets crumpled as it propagates. The crumpling at the frontiers is qualitatively similar to the plankton patterns on the ocean surface, the difference being that in dense bacterial suspensions stirring is internal, whereas background flow advects plankton [28, 29, 30].

The rest of the paper is organised as follows. We first introduce the models that we use to study the spreading of colony. Next we give an overview of the numerical method that we use. We then discuss the results obtained from our numerical simulations. We conclude by providing a discussion of our results.

4.2 Model

The generalized hydrodynamic description of an unbounded system of self propeled particles in a bulk fluid [31] is given by Equations (4.2), (4.3) and (4.4) which govern the time evolutions of the hydrodynamic velocity $\boldsymbol{u}$, polar order $\boldsymbol{p}$ and concentration c.

$$\rho(\partial_t \boldsymbol{u} + \boldsymbol{u}\cdot\nabla\boldsymbol{u}) = -\nabla P + \mu\nabla^2\boldsymbol{u} + \nabla\cdot(\boldsymbol{\Sigma}^a + \boldsymbol{\Sigma}^r), \tag{4.2}$$

$$\partial_t \boldsymbol{p} + (\boldsymbol{u} + v_0\boldsymbol{p})\cdot\nabla\boldsymbol{p} = \lambda \mathrm{S}\cdot\boldsymbol{p} + \boldsymbol{\Omega}\cdot\boldsymbol{p} + \Gamma\boldsymbol{h} + \ell\nabla^2\boldsymbol{u}, \text{ and} \tag{4.3}$$

$$\partial_t c + \nabla\cdot[(\boldsymbol{u} + v_1\boldsymbol{p})c] = 0. \tag{4.4}$$

For dense bacterial suspensions the concentration fluctuations become negligible. For such systems the two-dimensional limit of the system of Equations (4.2) and (4.3) on a substrate are derived [32] using the following approximations:

- Stokesian velocity field, which is expressed as a balance between the active and viscous forces.

- Thin-film approximation on the coordinate system $(\perp, z)$, where $\perp$ denotes the coordinates along the substrate surface and z is along the film-height. The gradients along substrate are assumed negligible compared to those along the thickness, i.e. $\partial_\perp << \partial_z$.

- The effective description of the system is reduced to two dimensions by averaging the variables along the film thickness h. The new two-dimensional variables are thus: $\overline{\boldsymbol{u}}, \overline{\boldsymbol{p}}(\perp, t) = \frac{1}{h}\int_0^h \boldsymbol{u}, \boldsymbol{p}(\perp, z, t)dz$.

- In the z-averaged description, the force generated by the apolar active stresses are at least of $O(h)$ or higher and are thus subdominant over the polar stress, which are of zero-orders in h, where $h << 1$. This can be directly observed for a channel-flow profile for the polar order.

The equations for the z averaged velocity and the polar order thus boil down to:

$$\Gamma_1 \overline{\boldsymbol{u}} = v\overline{\boldsymbol{p}} - \nabla P - \Lambda \frac{\partial F}{\partial \overline{\boldsymbol{p}}} \tag{4.5}$$

$$\partial_t \overline{\boldsymbol{p}} = \Lambda \overline{\boldsymbol{u}} - \frac{\delta F}{\delta \overline{\boldsymbol{p}}} \tag{4.6}$$

where $\Gamma_1 \sim \mu$, $v \sim \gamma$ and $\Lambda \sim \ell$. The stability of the homogeneous polar ordered state is sensitively dependent on the relative sign of the coefficients v and Λ. One has a stable polar ordered state when both these are of the same sign, i.e. when the active forces and the aligning forces of the velocity gradients act along the same direction.

An alternative model for bacterial suspensions at high concentrations is done by Wensink et al.[4], where, instead of taking the thin-film limit, the following assumptions are made:

- At high concentrations the polar order and the velocity are strongly correlated and can thus be described by only by an incompressible velocity field.

- The velocity field follows a modified incompressible hydrodynamic equation of the form:

$$\frac{\partial \boldsymbol{u}}{dt} = -\boldsymbol{u} \times \boldsymbol{\omega} - \nabla P + \nabla \cdot \Sigma + (\alpha(c) - \beta|\boldsymbol{u}|^2)\boldsymbol{u} \tag{4.7}$$

  The active stress Σ has the form:

$$\Sigma = A_1 \boldsymbol{u}\boldsymbol{u} + A_2(\nabla \boldsymbol{u} + (\nabla \boldsymbol{u})^T) + A_3 \nabla^2 (\nabla \boldsymbol{u} + (\nabla \boldsymbol{u})^T) \tag{4.8}$$

  The term $\sim (\alpha(c) - \beta|\boldsymbol{u}|^2)\boldsymbol{u}$ favours a polar-ordered flock in absence of other forces. The active stress terms, from left to right, contribute the following:

the first term leads to a non-unity coefficient for velocity self-advection, the second one leads to a negative diffusion term which generates instability over a band of wavenumbers, the third one imposes an upper threshold for the unstable wavenumbers by contributing a fourth-order gradient term with a positive coefficient.

The equation for the velocity field is thus:

$$\frac{\partial \boldsymbol{u}}{dt} = \lambda \boldsymbol{u} \times \boldsymbol{\omega} - \nabla P + (\alpha(c) - \beta|\boldsymbol{u}|^2)\boldsymbol{u} + \Gamma(c)\nabla^2 \boldsymbol{u} - \Gamma_2 \nabla^4 \boldsymbol{u}. \tag{4.9}$$

The coefficient λ of the self-advection term $\boldsymbol{u} \cdot \nabla \boldsymbol{u}$ is in general non-unity because of the reason described above, and thus breaks the Galilean invariance [33]. The velocity magnitude $|\boldsymbol{u}| = \sqrt{\alpha(c)/\beta}$ in absence of all the gradient terms in Eq. (4.9). $|\boldsymbol{u}| = 0$ for $(\alpha(c) \leq 0, \beta > 0)$ and $|\boldsymbol{u}| > 0$ otherwise. The negative diffusion term $\sim \Gamma(c)$ is the strength of the small scale stirring, and $\Gamma_2 (< 0)$ causes damping of the higher wavenumbers. The reader is notified here that one can recover a term exactly similar to the active forcing $v\boldsymbol{p}$ in Eq. (4.5) by taking a thin-film averaging of the negative diffusion term $\Gamma(c)\nabla^2 \boldsymbol{u}$ in Equation (4.9), and assuming that $\boldsymbol{u} \equiv \boldsymbol{p}$. The nonequilibrium steady state of Eq. (4.9) has been shown to display the presence of turbulent-like structures of collective motion, whose statistics agrees well to experiments on bacteria. Therefore we use this as our model for bacterial turbulence.

Because of the collective motion, the bacterial suspension also gets advected by the velocity field $\boldsymbol{u}$. This is easily modelled by supplementing Eq. (4.1) with an advection term. The modified equation for the evolution of the concentration field is

$$\frac{\partial c}{\partial t} + \boldsymbol{u} \cdot \nabla c = D\nabla^2 c + \mu c(1 - c). \tag{4.10}$$

The equations that we use fall broadly under the Toner-Tu class of hydrodynamic equations for soft-active matter. Coefficients $\alpha(c)$ and $\Gamma(c)$ model the effect of bacterial concentration on the collective motion. As we are interested in planar growth of a colony on a Petri dish like surface, we study dynamics in two-dimensions.

Below we present two possible choices of ($\Gamma(c)$,$\alpha(c)$) which are of experimental relevance.

- Model A, $\Gamma(c) \equiv \Gamma$ and $\alpha(c) \equiv \alpha$. We use Model A to study the invasion of one bacterial colony into another. We assume that both the colonies have indistinguishable swimming capabilities and are in turbulent phase. For this model, it is more appropriate to think of c as the concentration of the invading species.

- Model B, $\Gamma(c) \equiv \Gamma c$ and $\alpha(c) \equiv \alpha c$. We use Model B to study spreading of a bacterial colony on a surface. Our choice $\alpha(c) = \alpha c$ and $\Gamma(c) = \Gamma c$ ensures that $\boldsymbol{u} = 0$ when $c = 0$.

4.3 Numerical Simulations

We use a square domain $\mathcal{D}$ with each side of length $L = 32\pi$ and discretize it using $N^2 = 2048^2$ collocation points. We numerically integrate Eq. (4.10) using a second order explicit finite-difference scheme for spatial derivatives and Euler method for time integration [30]. To ensure incompressibility, we write Eq. (4.9) in vorticity-streamfunction formulation Eq. (4.11) and numerically integrate it using using a pseudo-spectral method [40].

$$\frac{\partial \omega}{\partial t} = \lambda \nabla \times (\boldsymbol{u} \times \omega) + \nabla \times (\alpha(c) - \beta |u|^2)\boldsymbol{u} + \nabla \times [\Gamma(c) \nabla^2 \boldsymbol{u}] + \Gamma_2 \nabla^4 \omega. \quad (4.11)$$

Here, $\psi(\boldsymbol{x}, t)$ is the streamfunction, $\boldsymbol{u} = \hat{z} \times \nabla \psi$, and $\nabla^2 \psi = \omega$.

We set $\alpha = 1$, $\beta = 0.5$, $\Gamma = -0.045$, $\Gamma_2 = |\Gamma|^3$, and $\lambda = 3.5$ so that the velocity correlation statistics are consistent with that of a quasi-2D *B. subtilis* suspension [4].

In Figs. 4.2 and 4.3 we show a typical snapshot of the vorticity field and the corresponding energy spectrum obtained by direct numerical simulation of Eq. (4.9) with $\Gamma(c) \equiv \Gamma$ and $\alpha(c) \equiv \alpha$. Note that the exponents of $5/3$ for low wave numbers and $-8/3$ for high wave numbers are consistent with Ref. [4].

We initialise c as

$$c(x, y, t = 0) = \begin{cases} 1, & \text{if } x \leq L/100 \\ 0, & \text{otherwise} \end{cases}$$

and study its evolution for varying diffusivity D and growth rate μ.

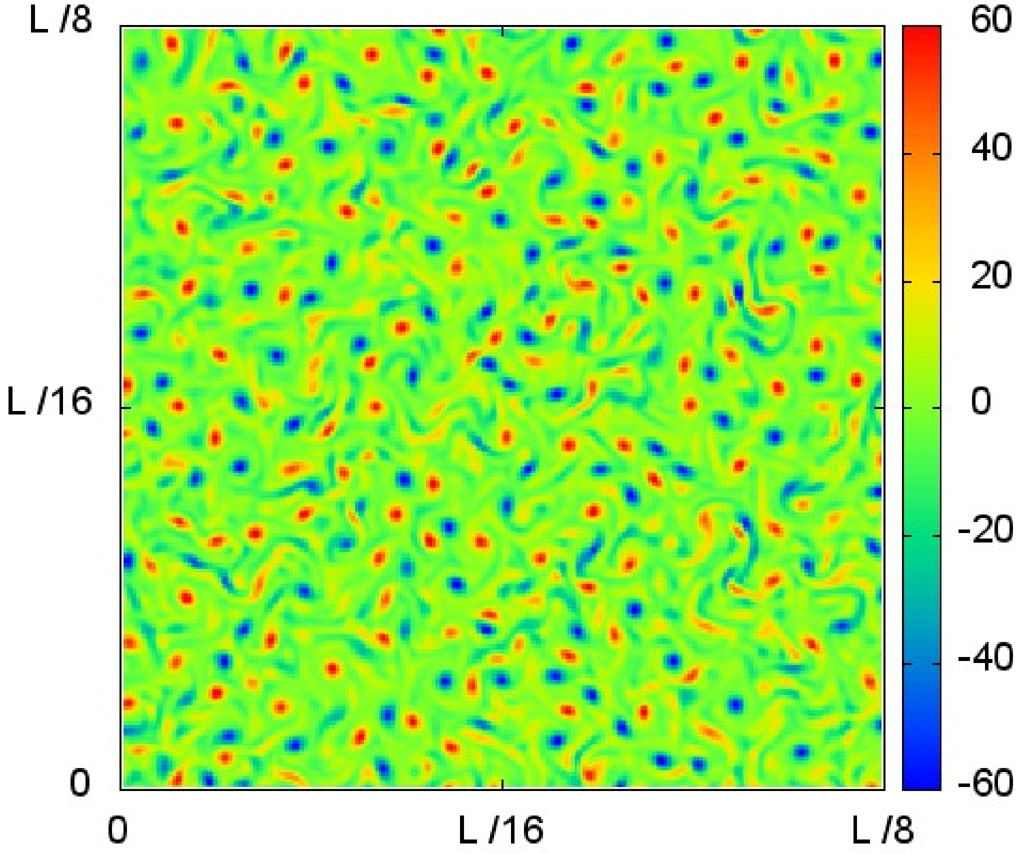

Figure 4.2: The pseudo-color plot of the steady state vorticity field over a section of our simulation domain obtained from DNS of Eq. (4.9) with $\alpha(c) = \alpha$ and $\Gamma(c) = \Gamma$.

4.4 Results

In absence of the velocity field $\boldsymbol{u}$, concentration front of width $\sim 8\sqrt{D/\mu}$ propagates from left to right with a speed $\sim 2\sqrt{D\mu}$ (Fisher velocity) [2, 6, 7]. What happens when bacteria perform collective motion that resembles turbulence?

Using Model A and Model B, we now systematically characterize the properties of colonies performing turbulence like collective motion. We study how bacterial turbulence modifies the spatio-temporal structure of the spreading/invasion of a colony. We conduct measurements in the spatio-temporal window where the front moves with a constant velocity and is $L/3$ distance away from the left and right boundaries.

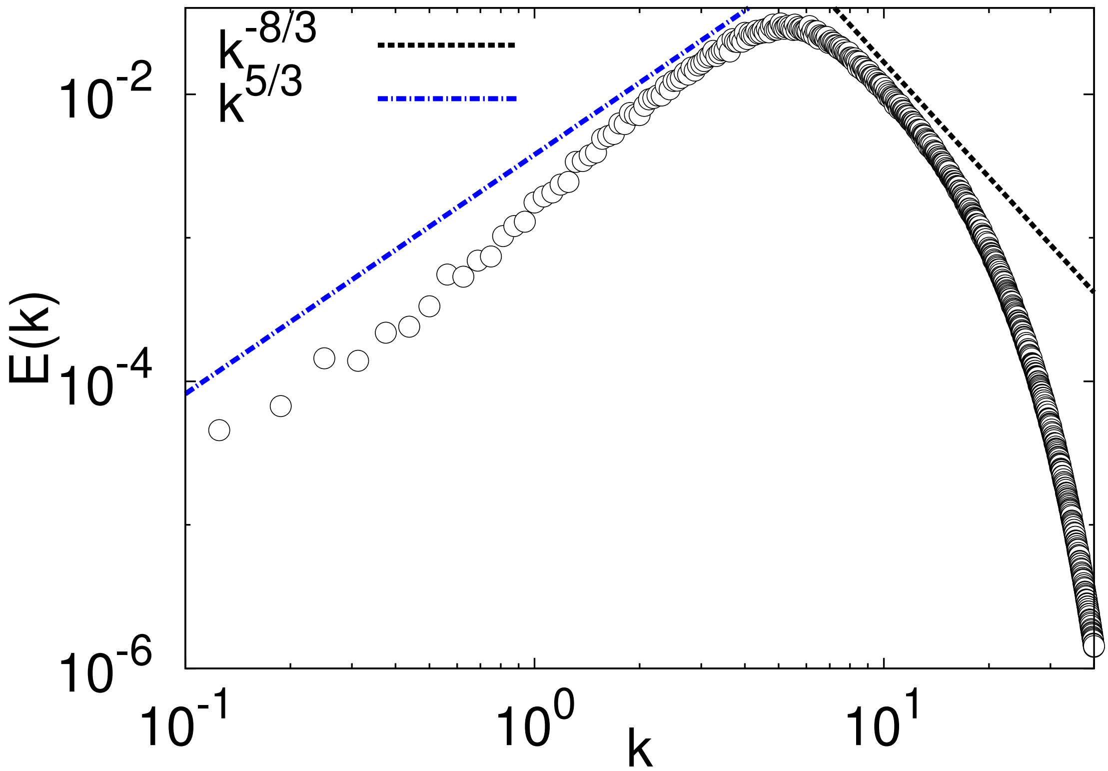

Figure 4.3: The corresponding kinetic energy spectrum $E(k) = \sum_{k'} |u^2_{k'}|$ where $k' \in [k-1/2, k+1/2]$. The peak of the spectrum occurs around $k_m = 6$. In agreement with previous studies we observe a $k^{5/3}$ scaling (blue dash-dot) for $k < k_m$ and a $k^{-8/3}$ scaling (black dash) for $k > k_m$.

4.4.1 Front propagation in Model A

Using Model A, we investigate the invasion of a motile colony with a selective advantage μ into another motile colony. In Figure 4.4 we show typical snapshots of the concentration profile for the representative values of diffusivity D and growth rate μ. The interface becomes rough because of the advecting velocity field $\boldsymbol{u}$. The interface roughness increases on reducing D and μ. In particular for a fixed D, the undulations of the concentration front become more compact on increasing μ. On the other hand, for a fixed μ, undulations of concentration front are enhanced on reducing D. Physically, a large value of D implies that the motion because of bacteria pushing each other overwhelms the collective behavior. In this regime, as observed in Fig. 4.4, we indeed find that collective motion has very minor effect on the front. We quantify these observations in the following sections.

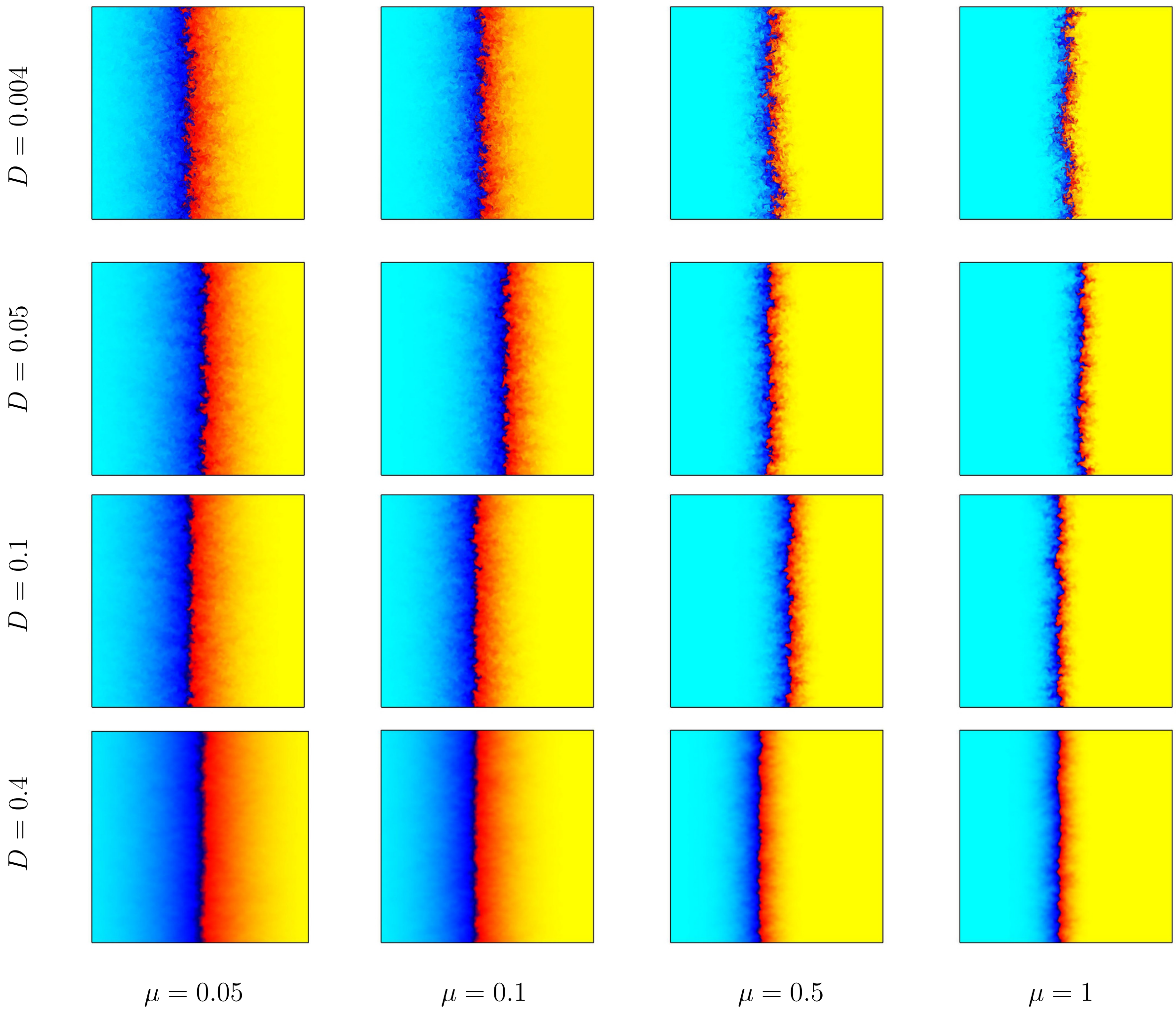

Figure 4.4: Pseudocolor plots of the concentration fields for Model A for representative values of D and μ. To emphasize the front structure, we show a square window of side length $\approx L/4$. Blue indicates regions of high concentration ($c \geq 0.5$) and yellow indicates regions of low concentration.

4.4.2 Front propagation in Model B

We use Model B to investigate spreading of a motile colony with doubling time μ. In Figure 4.5 we show typical snapshots of the concentration field for the representative values of diffusivity D and growth rate μ. Here again, presence of collective motion leads to roughing of the interface. However, unlike Model A, in Model B velocity is present only where bacteria concentration is non-zero. This leads to formation of finger like patterns in Model B that are absent in Model A for same values of D and μ (compare Figs. 4.4 and 4.5).

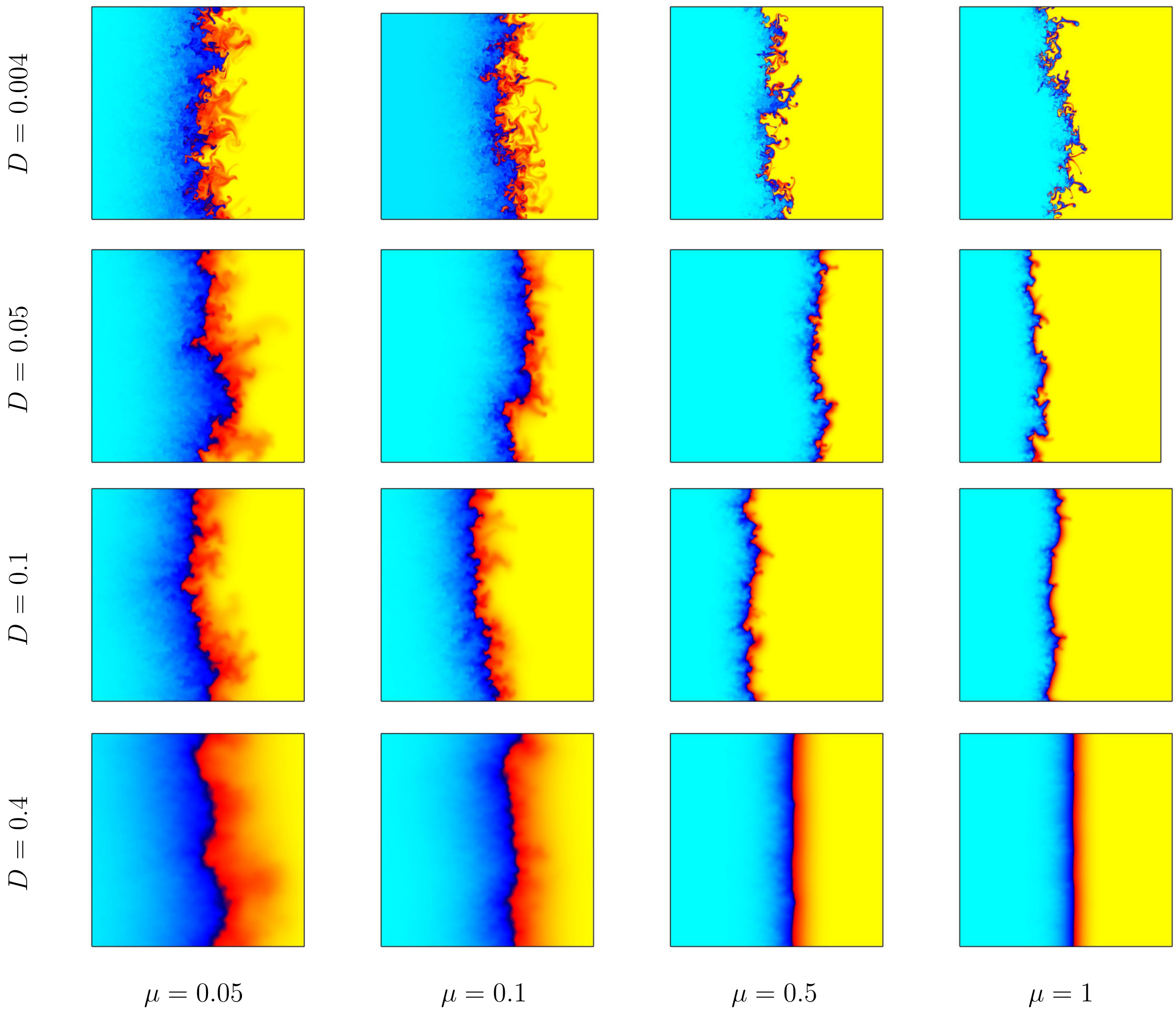

Figure 4.5: Pseudocolor plots of the concentration fields for Model B for representative values of D and μ. We only show a square window with each side $\approx L/4$ to emphasise the front-structure. Blue indicates regions of high concentration ($c \geq 0.5$) and yellow indicates regions of low concentration. Note that interface undulations in Model B are larger in comparison to Model A (see Fig. 4.4).

4.4.3 Eddy diffusivity for Model A

Using the procedure outlined in Ref. [23] we now briefly describe the methodology to obtain the eddy diffusivity for Model A. Assuming very small variations of the concentration field perpendicular to the direction of front propagation, we decompose these as $c(x, y) = \bar{c}(x) + c'(x, y)$. Here overline indicates averaging over y direction $\overline{f}(x) \equiv \frac{1}{L}\int_0^L f(x, y)\mathrm{d}y$ and dashed quantities represent the magnitude of variations from the y-averaged value as a result of turbulent fluctuations. It

$D \backslash \mu$	0.05	0.1	0.5	1.0
0.004	0.20	0.21	0.18	0.18
0.05	0.19	0.19	0.19	0.18
0.1	0.17	0.18	0.18	0.16
0.4	0.10	0.10	0.11	0.11

Table 4.1: Numerical estimate of turbulent diffusivity $D_t \equiv \overline{v_x c'}/\partial_x \overline{c}$ for different values of D and μ obtained from our direct numerical simulations.

should be noted that these variations themselves have zero mean. Because the velocity field is homogeneous and isotropic $\overline{v} = 0$. From Eq. (4.10) we obtain the equations for $\overline{c}$ and c':

$$\frac{\partial \overline{c}}{\partial t} = -\partial_x \overline{\boldsymbol{F}} - \mu \overline{H} + \mu \overline{c}(1-\overline{c}) + D\partial_{xx}\overline{c}; \tag{4.12}$$

$$\frac{\partial c'}{\partial t} = \mu c'(1-2\overline{c}) - \nabla \cdot (\boldsymbol{v}\overline{c} + \boldsymbol{v}c') + \partial_x \overline{\boldsymbol{F}} -\mu(c'^2 - \overline{H}) + D\nabla^2 c'. \tag{4.13}$$

Here $H = c'^2$ and $\boldsymbol{F} = \boldsymbol{v}c'$ are respectively the autocorrelation and flux of the turbulent fluctuations in the concentration field. We describe their time evolution here. From our numerical simulations, we find that $\overline{H}$ is negligible. We further assume: (a) the turbulence time-scales are smaller than the scales associated with the front so that the time-variation of the turbulent fluctuations in the velocity field can be ignored in the evolution equation for $\boldsymbol{F}$; (b) isotropic velocity field $\boldsymbol{vv} = v^2\mathbb{I}$; (c) tau approximation $\overline{\boldsymbol{uu}\cdot\nabla c'} = \overline{\boldsymbol{u}c'}/\tau$ [23]. Then from Eq. (4.13) we find that $\overline{\boldsymbol{F}}$ boils down to a scalar quantity $\overline{F}$ obeying the following equation:

$$\frac{\partial \overline{F}}{\partial t} = -v^2 \partial_x \overline{c} - \frac{\overline{F}}{\tau_F}. \tag{4.14}$$

Here $\frac{1}{\tau_F} = \frac{1}{\tau} - \mu(1-2\overline{c})$, τ_F is the relaxation time for $\overline{F}$ [23], and $\mathbb{I}$ is the identity matrix. Assuming that $\overline{F}$ does not vary over the front propagation time-scales, using Eq. (4.14), we get the Fickian form $\overline{F} = -D_t\partial_x\overline{c}$ where $D_t = -\tau_F v^2$ and $v = v_{rms}/\sqrt{2}$. Because the Fisher front propagates along the horizontal (x) direction, the variations along the vertical (y) direction have been neglected. We, therefore, estimate the eddy diffusivity for our simulations as $D_t = \overline{v_x c'}/(\partial_x\overline{c})$ where, v_x is the horizontal component of the velocity. The numerical estimate of D_t for various values of D and μ are tabulated in Table 4.1. We find that D_t varies between $0.1-0.2$ and is very close with the eddy-diffusivity estimate $D_t = v_0/k_m \approx 0.17$ that we use in the main text.

4.4.4 Front speed: Model A versus Model B

We now investigate the speed of the concentration front for the two models. The front-speed is calculated as

$$\mathcal{V}_f = \frac{d}{dt}\left[\frac{1}{L}\int c(\boldsymbol{x},t)dxdy\right]. \tag{4.15}$$

We have verified that in absence of $\boldsymbol{u}$, $\mathcal{V}_f = 2\sqrt{D\mu}$. As turbulence enhances the effective diffusivity of a scalar (e.g., temperature), in the same way we expect that presence of motility (bacterial turbulence) would enhance bacterial diffusivity D and hence $\mathcal{V}_f$. In Fig. 4.6 we plot $\mathcal{V}_f$ versus D for the two models for $\mu = 0.05, 0.1, 0.5,$ and 1. It is clear that front speed for Model A is larger than Model B. This is because for Model A both the species are motile and hence $\boldsymbol{u}$ is non-zero and of same magnitude everywhere whereas, for Model B, $\boldsymbol{u}$ is non-zero only where $c \neq 0$. For Model A, we can estimate the turbulent diffusivity as $D_t = v_0/k_m \approx 0.17$ where, $v_0 \equiv \sqrt{\Gamma^3/\Gamma_2} = 1$ is the characteristic velocity of the turbulent flow [4]. Thus the front-speed in presence of turbulence for Model A can be estimated as $2\sqrt{\mu(D+D_t)}$ which is in close agreement with the result of our DNS (see Fig. 4.6). In the limit $D \to 0$, the front speed is completely determined by turbulent diffusivity $\mathcal{V}_f \sim 2\sqrt{D_t\mu}$. This explains the roughness of the interface at lower values of D. On the other hand, when $D \gg D_t$, collective motion is irrelevant and $\mathcal{V}_f \sim 2\sqrt{D\mu}$ for the two models.

4.4.5 Multivalued nature of the propagation front

As a result of underlying turbulence, the front structure gets distorted. From Figs. 4.4 and 4.5 it is clear that at the interface, $c(\boldsymbol{x}) \approx 0.5$. We define $N_I \equiv \langle\sum_{(i,j)} \delta[c(x_i, y_j, t) - 0.5]/N\rangle$ as a preliminary estimator of the front structure. Here $0 \leq (i,j) < N$ are the Cartesian grid indices in our simulation domain $\mathcal{D}$, and $0 \leq \langle\cdot\rangle$ indicates temporal averaging. Thus for a front without overhangs $N_I = 1$

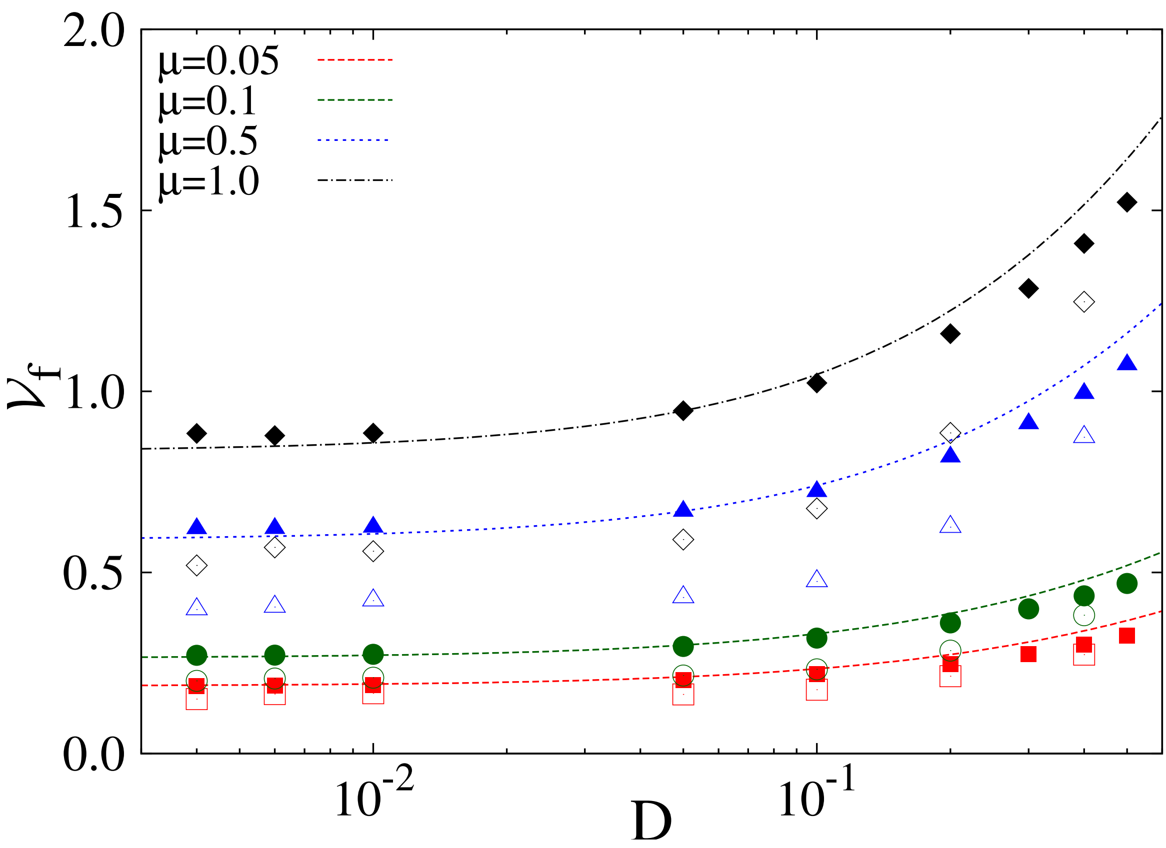

Figure 4.6: Turbulent front speed $\mathcal{V}_f$ versus diffusivity D for $\mu = 0.05$ (square), $\mu = 0.5$ (circle), $\mu = 0.1$ (triangle), and $\mu = 1.0$ (diamond) for Model A (filled symbols) and Model B (empty symbols). Dashed lines show the corresponding front speed estimated by eddy diffusivity approximation $\mathcal{V}_f = 2\sqrt{(D + D_t)\mu}$ with $D_t = 0.17$ for Model A.

whereas, $N_I = N$ if $c = 0.5$ over the entire domain. The plot in Fig. 4.7 shows that at large values of D, $N_I = 1$ indicating the smooth nature of the front. On reducing D, N_I keeps on increasing monotonically indicating the enhanced roughness of the front. We do not observe any significant difference in N_I between Model A and Model B except for very small value of D. This qualitative dependence does not change on varying μ. We would like to point that for small values of D, N_I is larger for Model A in comparison to Model B. This is because in Model A turbulence is present over the entire domain and leads to enhanced stirring and formation of small-scale structures. The enhanced small-scale structure is also consistent with our earlier observations about larger front speeds $\mathcal{V}_f$ for Model A in comparison to Model B (Section 4.4.4, Fig. 4.6).

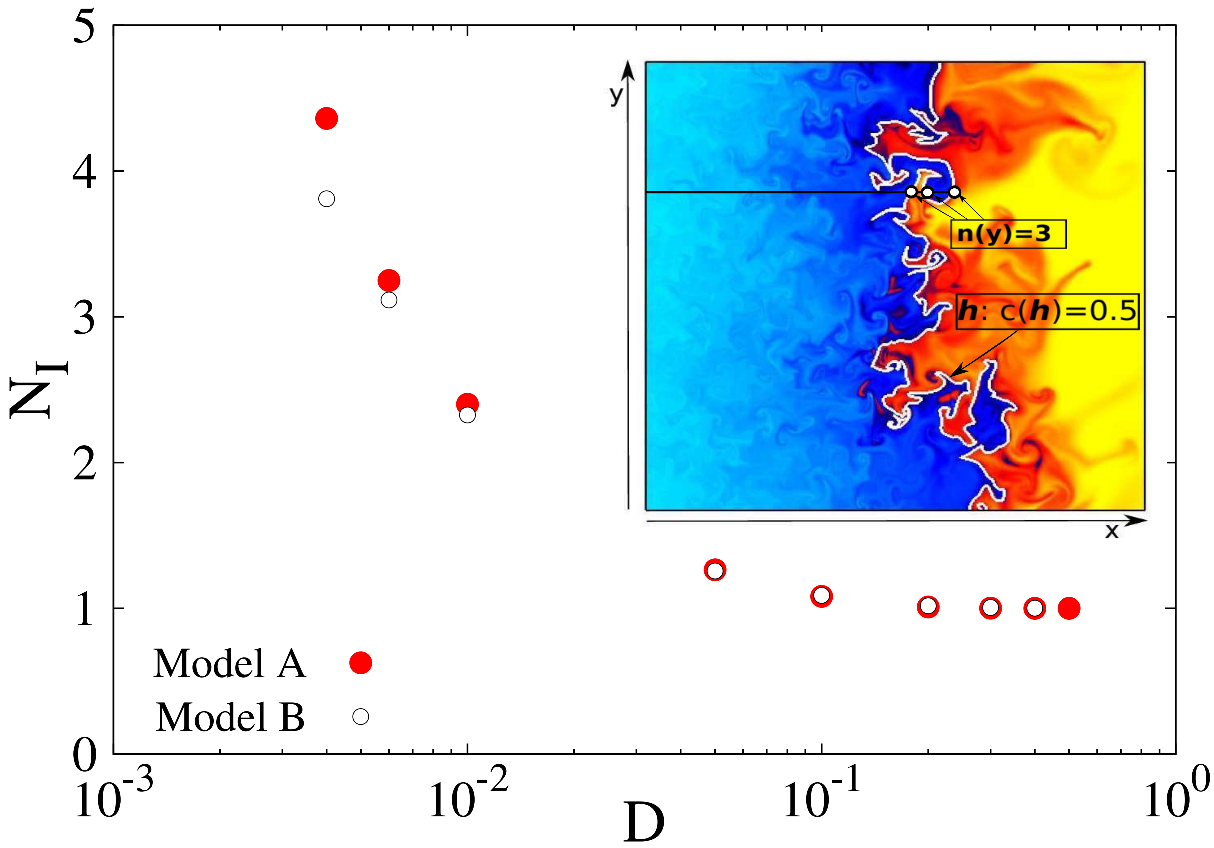

Figure 4.7: Average number of intersections (N_I) as a function of the diffusivity D for $\mu = 0.05$. For $D > 0.1$ front is essentially single valued. We do not observe any significant dependence of N_I on μ (not shown here). The inset shows a zoomed in snapshot of the concentration field along with the $c = 0.5$ hull $\boldsymbol{h}$ (white curve) obtained by using BRWA for $D = 0.004$ and $\mu = 0.05$. Because of the underlying turbulence, the hull $\boldsymbol{h}$ is multivalued at several locations.

From visual inspection (see Figs. 4.4 and 4.5) it is clear that although Model A and Model B have similar values of N_I, the size of interface undulations are significantly different for the two models (see Figs. 4.4 and 4.5). To quantify these differences, we first need to identify a front in the concentration field $c(\boldsymbol{x}, t_0)$ at a time instant t_0. We use the biased random walk algorithm (BRWA) [41] to identify a locus of points (or a hull) $\boldsymbol{h}_i \equiv (x_i, y_i)$ such that $c(\boldsymbol{h}_i, t_0) = 0.5$ where the hull index $0 \leq i \leq N_h$ and $0 \leq (x_i, y_i) \leq L$ are the Cartesian points in our simulation domain $\mathcal{D}$. Connecting the points of the hull, we get a continuous curve that starts at the bottom of the domain $y = 0$ and ends at the top $y = L$. Figure 4.7(inset) shows a representative plot of the $c = 0.5$ hull overlaid on the pseudocolor plot of the concentration field.

4.4.5.1 Hull width

We start our analysis by calculating the hull width $\sigma_h = \langle [\frac{1}{N_h}\sum_{i=0}^{N_h} x_i^2 - (\frac{1}{N_h}\sum_{i=0}^{N_h} x_i)^2]^{1/2} \rangle$ (standard deviation of the x-coordinate of the hull). Here, $\langle [\cdot] \rangle$ indicates temporal averaging. In figure 4.8, we plot σ_h as a function of $2\sqrt{D\mu}$ (the intrinsic front velocity in absence of collective motion) for the two models. When the typical turbulent velocity $v_0 \ll 2\sqrt{D\mu}$, the intrinsic diffusion dominates over turbulence and the two models behave in the same way. On the other hand for $v_0 \gg 2\sqrt{D\mu}$, σ_h for Model B is larger than Model A. This is consistent with our observation about presence of large plume like structures in Model B (see Figs. 4.4 and 4.5).

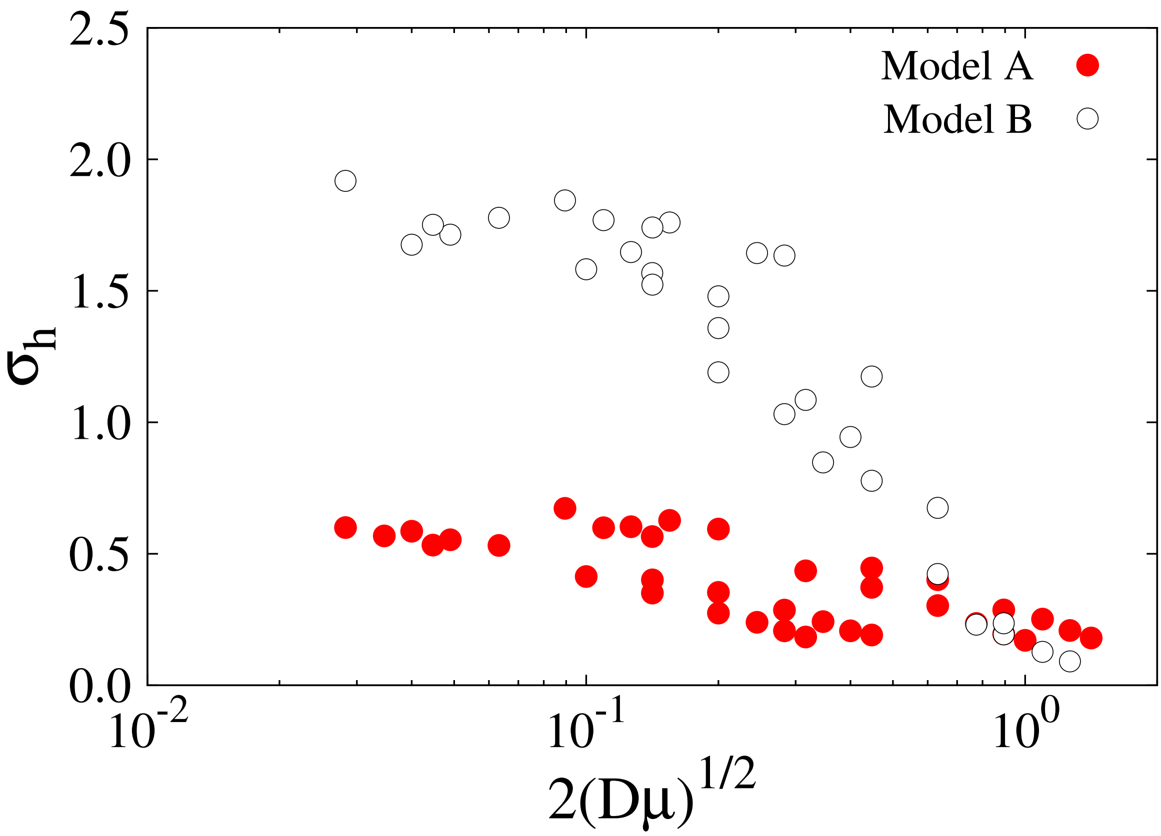

Figure 4.8: Standard deviation σ_h of the front height with respect to its mean position as function of $2\sqrt{D\mu}$. Note that for $v_0 \ll 2\sqrt{D\mu}$, σ_h is dramatically different for the two models indicating presence of large plume like structures in Model B.

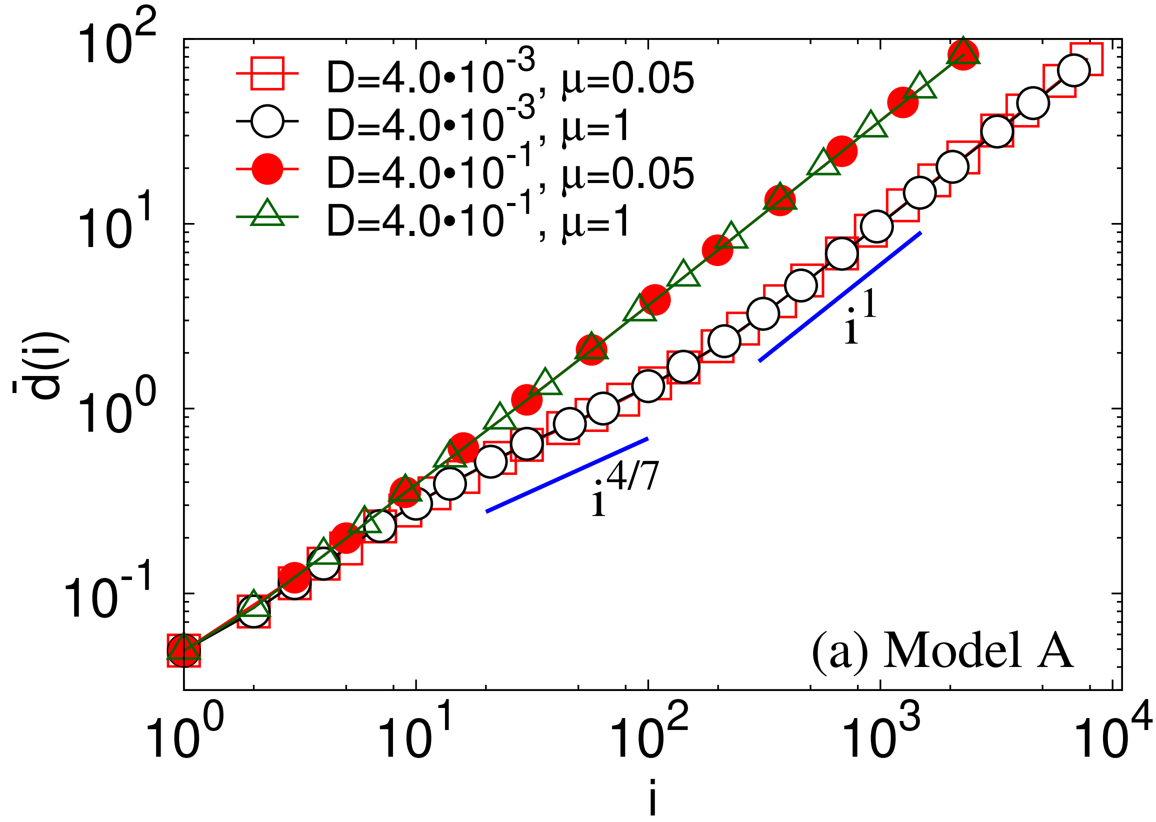

Figure 4.9: Average distance between points $\overline{d}(i)$ versus distance index i plotted on log-log axes for Model A for different values of D, and μ.

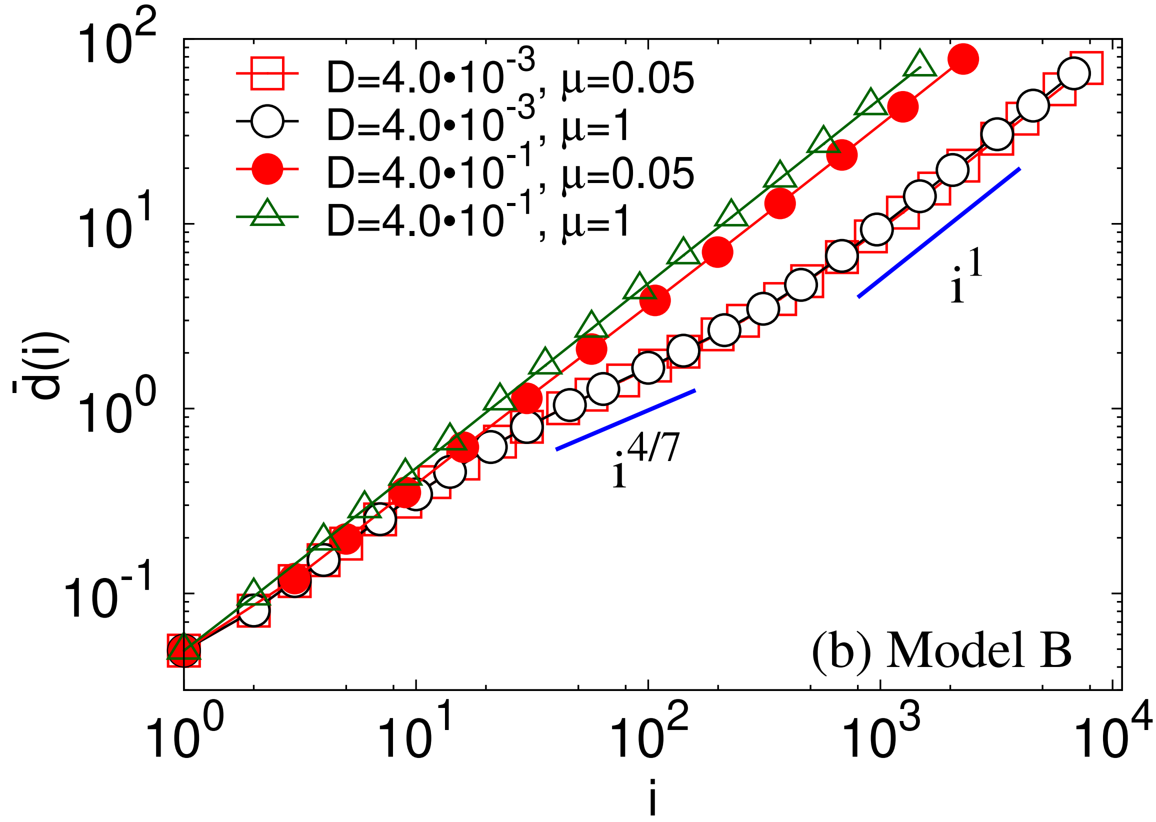

Figure 4.10: Average distance between points $\overline{d}(i)$ versus distance index i plotted on log-log axes for Model B for different values of D, and μ.

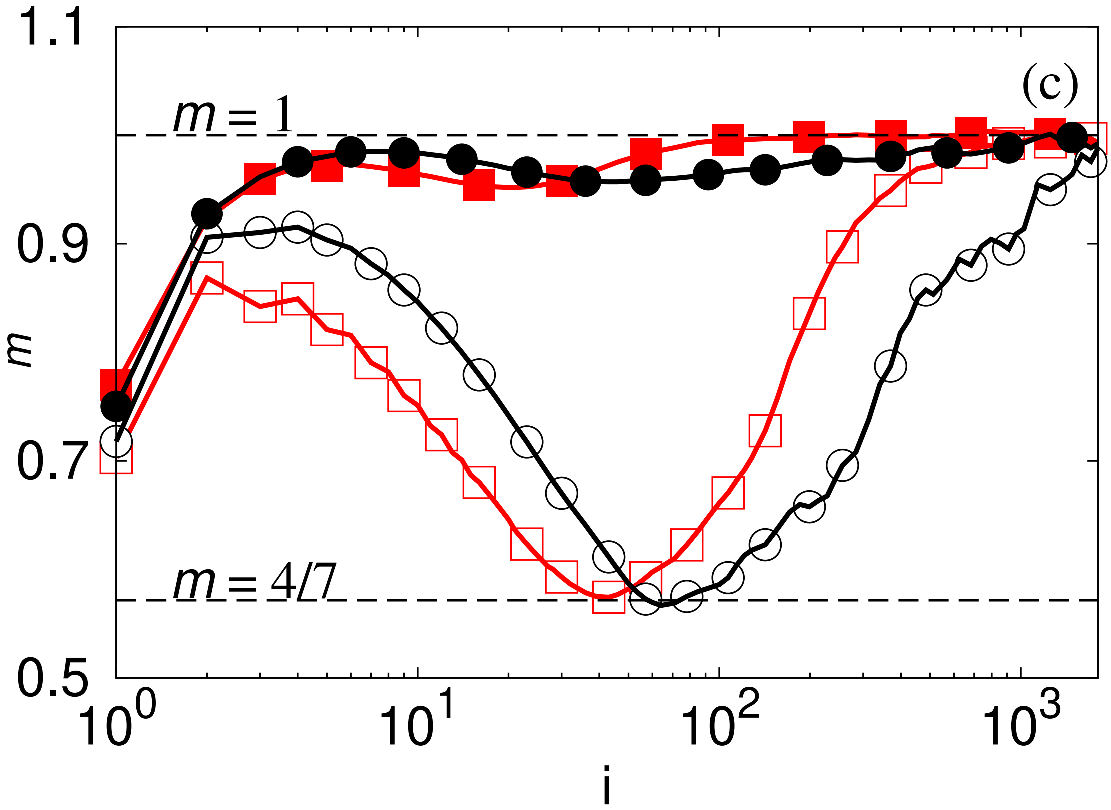

Figure 4.11: Semilog plot of the local slope m for Model A [$D = 4 \cdot 10^{-3}$ (red empty square), and $D = 4 \cdot 10^{-1}$ (red filled square)] and Model B [$D = 4 \cdot 10^{-3}$ (black empty circle), and $D = 4 \cdot 10^{-1}$ (black filled circle)] at fixed $\mu = 5 \cdot 10^{-2}$. Horizontal dashed lines indicate $m = 4/7$ and $m = 1$.

4.4.5.2 Hull fractal dimension

We now study the fractal dimension of the hull using an equispaced polygon method [41]. Consider a hull consisting of a sequence of points $(x_0, y_0), (x_1, y_1).....(x_{N_h}, y_{N_h})$, the average distance between points separated by i steps is:

$$\bar{d}(i) = \sum_{j=0}^{N_h - i} d_j(i)/(N_h - i + 1). \tag{4.16}$$

Here, $0 \leq i \leq N_h - 1$ and $d_j(i) = \sqrt{(x_j - x_{j+i})^2 + (y_j - y_{j+i})^2}$. For a fixed number of steps i, the average distance and the fractal dimension are related as $\bar{d}(i) \propto i^{1/d_f}$ [41]. In Figs. 4.9 and 4.10 we plot $\bar{d}(i)$ versus i for different values of D and μ for the two models. For large values of D, independent of μ and except for very small scales, we find that $\bar{d} \propto i$ i.e., the front is essentially flat $d_f = 1$. For small values of D, presence of bacterial stirring leads to front undulations. We find we find a decade long scaling range with $\bar{d}(i) \propto i^{4/7}$ or $d_f = 7/4$ around the typical eddy scale ($\bar{d} \approx 2\pi/k_m$) and $\bar{d}(i) \propto i$ for $i \gg 2\pi/k_m$. Note that $d_f = 7/4$ also for purely diffusive fronts [42]. Thus, $d_f = 7/4$ further supports our modeling of bacterial turbulence by an effective diffusivity. To highlight the difference between Model A and Model B, in Fig. 4.11, we plot the local slope $m \equiv \mathrm{d}\log\bar{d}/\mathrm{d}\log i$ versus i. As discussed earlier, we find that for large D, $m \to 1$. However, for small D we observe that the region with $4/7$ scaling for model A appears at a slightly earlier stage than model B. We believe this is because in model A the bacterial stirring is present on both sides of the front whereas for model B it is only present in regions with $c = 1$. Similar cross over from $d_f \simeq 7/4$ to $d_f = 1$ has also been observed in earlier studies on front propagation in 2d microscopic simulations of diffusing particles [42], stochastic Fisher-Kolmogorov-Petrovsky-Piskunov (sFKPP) equation [43], and in vegetation fronts [41]. We would like to point out that in the case of sFKPP, the front undulations are driven by stochastic forcing that models fluctuations in the size of the bacteria population [12, 22] whereas, in our study collective motion of the bacteria causes front undulations and also sets up the scale at which cross over in d_f takes place.

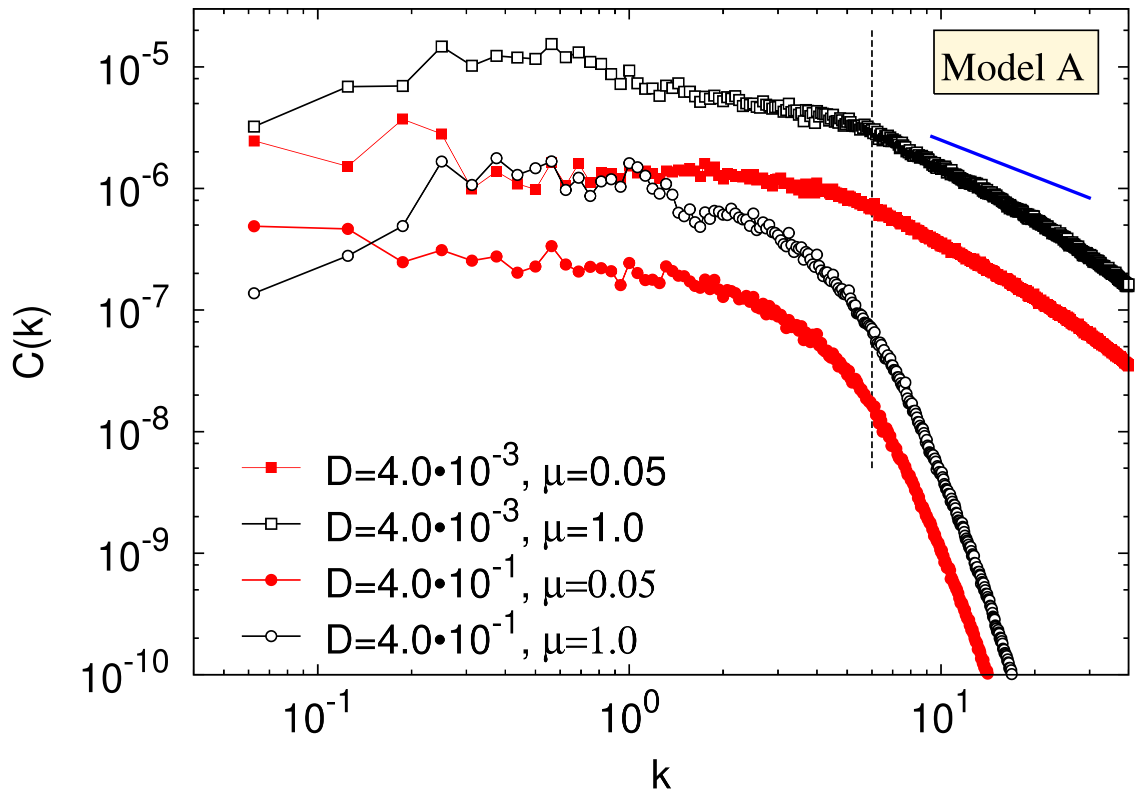

Figure 4.12: Concentration spectra for Model A for varying diffusivity $D = 0.004$, and 0.4, and $\mu = 0.05$, and 1.0. The blue line indicates the Bachelor scaling k^{-1} and the vertical dashed line indicates k_m.

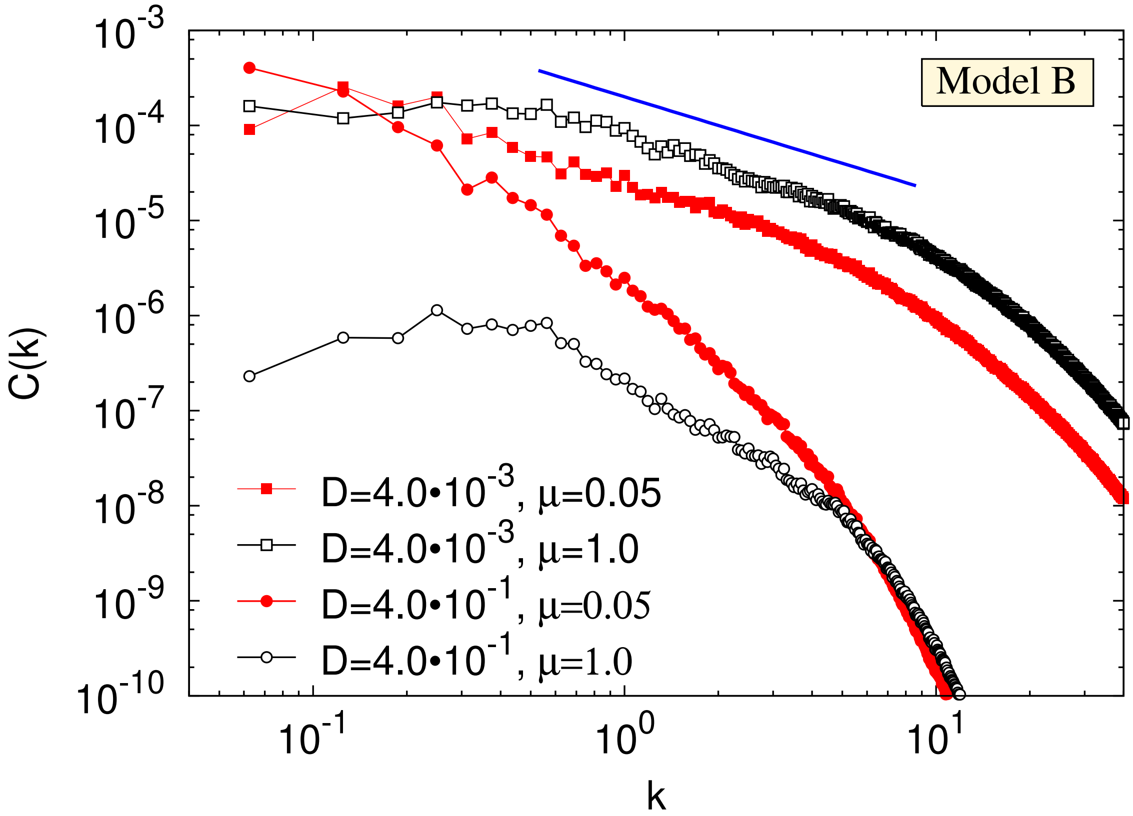

Figure 4.13: Concentration spectra for Model B for varying diffusivity $D = 0.004$, and 0.4, and $\mu = 0.05$, and 1.0. The blue line indicates the Bachelor scaling k^{-1} and the vertical dashed line indicates k_m.

4.5 Concentration Spectrum

To further quantify the statistical properties of the undulating interface, we now study the spectrum of fluctuations in the concentration field arising from bacterial turbulence. This is expressed as : $C(k) = \sum_{k-1/2\leq k'\leq k+1/2}|c_k'^2|$ where, $c' = c - (\int c dy)/L$. The plots in Fig. 4.12 and Fig. 4.13 shows $C(k)$ versus k for Model A and Model B.

$C(k)$ *for Model A* [Fig. 4.12]— The spectrum is flat and does not show any scaling behaviour for $k < k_m$. For $k > k_m$ and large $D = 0.4$, diffusion is dominant and the spectrum falls off sharply. At small $D = 0.004$, interface modulation because of turbulence becomes dominant and we observe a small regime showing $C(k) \sim k^{-1}$ scaling. The k^{-1} scaling appears because at small scales the undulations because of stirring are similar to that of a passive-scalar stirred by random flow which shows the k^{-1} Bachelor scaling [44, 45].

$C(k)$ *for Model B* [Fig. 4.13]— Here the spectral properties are more intriguing. For $D = 0.4$ and $\mu = 1.0$, the amplitude variations are of the same order as model A, but we observe a k^{-1} regime for $k < k_m$. For small D and $\mu = 0.05, 1.0$, we observe that both large and small scale undulations are present (see Fig. 4.5). This shows up as an extended k^{-1} scaling regime in the Fourier space. The intermediate case with $D = 0.4$ and $\mu = 0.05$ is the most intriguing. We observe presence of large scale undulations but no small scale plume like structures or finger like patterns (Fig.4.5). The $C(k)$ spectrum for this case is much steeper than k^{-1} and the spectral content is close to the $D = 0.004, \mu = 0.05$ case for $k < k_m$ and is close to the $D = 0.4, \mu = 1.0$ case for $k > k_m$.

4.6 Conclusion

We proposed two minimalistic models to study colony front propagation in dense colonies of motile bacteria performing turbulence like collective motion. We study two scenarios: (a) invasion of one colony over the other (Model A) and (b) spreading of colony on a petri dish (Model B). We find that presence of collective turbulence like motion always enhances the front propagation speed. We highlight the similarities and the differences between the two models.In particular, Model B allows for large scale undulations which are absent in Model A. We quantify the fractal structure of the front and show that the fractal dimension of the front around the stirring scales is $d_f = 7/4$. Finally we also show that, for certain parameter values, the concentration fluctuations arising from bacterial turbulence are similar to those of passive scalar stirred by a random flow. Earlier experiments have investigated spreading of dense colonies of non-motile bacteria or of motile bacteria that form swarms. We hope that our simulations would stimulate new experimental studies on the spreading of colonies in the newly found regime of bacterial turbulence.

Appendix

Biased random walk algorithm(BRWA)

This is an algorithm for approximating the edge of a hull-surface. The algorithm described here is applicable only for a connected hull surface. For the bacterial front this is the locus of points with $c = 0.5$. Let the original hull-edge be represented by a series of points 1-N as shown by the green line in Figure 4.14. The marker starts at the lowermost point on the hull at the bottom of the domain. At every step it iteratively checks the four immediate neighbors for a hull-surface point, in the order left-front-right-back, the initial direction being always measured w.r.t. the last move. The marker moves a step towards the direction at which it first identifies a hull-surface point. The algorithm terminates when the marker reaches the top row, i.e. when all the points along the hull surface have been covered at least once.

Hull Fractal dimension

Fractal dimension provides a statistical index to understand the complexity of a surface by comparing how the details captured in a pattern changes with the scale

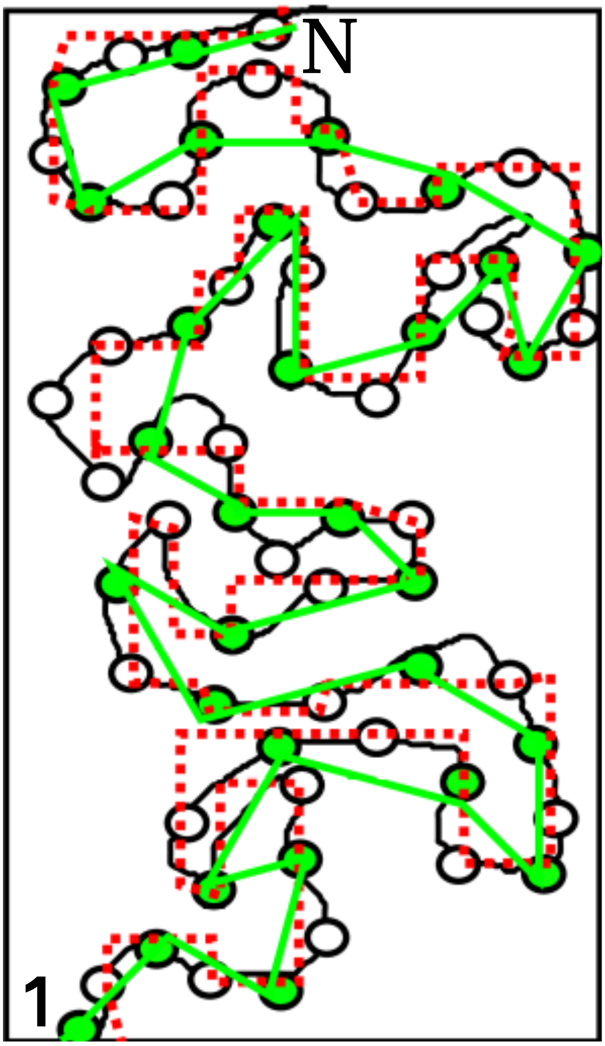

Figure 4.14: Schematic description of a hull surface [41] consisting of points marked (x_0, y_0)-(x_N, y_N). The black line indicates the original surface and the red-dashed line indicates the one approximated by Biased Random Walk Algorithm. The green line represents the polygon-approximated hull surface.

at which it is measured. For the hull surface described above, we use the equispaced polygon method for determination of the fractal dimension. The principle is as follows: We choose a set of intervals i for counting points along the hull surface. Thus for a surface consisting of N points, the possible values of i ranges from 1 to $N-1$. For each such index i, one approximates the hull-surface by a polygon drawn by joining points at interval i, as shown by the green line in Figure 4.14. For each such polygon one then calculates the average pairwise distance $\overline{d}(i)$, where the averaging is taken throughout the hull surface. The hull fractal dimension d_f is obtained from the exponent of the variation of $\overline{d}(i)$ with i; thus $\overline{d}(i) \propto i^{1/d_f}$.

Bibliography

[1] M. Fauvart *et al.*, Soft Matter **8**, 70 (2012).

[2] J. D. Murray, *Mathematical Biology I: An Introduction, vol. 17 of Interdisciplinary Applied Mathematics* (Springer, New York, NY, USA, 2002).

[3] S. Atis, B. T. Weinstein, A. W. Murray, and D. R. Nelson, Phys. Rev. X **9**, 021058 (2019).

[4] H. H. Wensink *et al.*, Proc. Nat. Acad. Sc. **109**, 14308 (2012).

[5] C. Dombrowski *et al.*, Phys. Rev. Lett. **93**, 098103 (2004).

[6] R. Fisher, Ann. Eugenics **7**, 335 (1997).

[7] A. Kolmogorov, I. Petrovsky, and N. Piscounoff, Moscow Univ. Bull. Math. **1**, 1 (1937).

[8] J.-i. Wakita *et al.*, J. Phys. Soc. Jpn. **63**, 1205 (1994).

[9] E. Ben-Jacob *et al.*, Nature **368**, 46 (1994).

[10] N. Verstraeten *et al.*, Trends Microbiol. **16**, 496 (2008).

[11] A. Beer *et al.*, Proc. Nat. Acad. Sci. **106**, 428 (2009).

[12] K. Korolev, M. Avlund, O. Hallatschek, and D. Nelson, Rev. Mod. Phys. **82**, 1691 (2010).

[13] P. Deng, L. d. V. Roditi, D. van Ditmarsch, and J. B. Xavier, New J. Phys. **16**, 015006 (2014).

[14] D. Kearns, Nat. Rev. Microbiol. **8**, 634 (2010).

[15] A. Czirok, M. Matsushita, and T. Vicsek, Phys. Rev. E **63**, 031915 (2000).

[16] M. Copeland and D. Weibel, Soft Matter **5**, 1174 (2009).

[17] A. Sokolev, I. Aranson, J. Kessler, and R. Goldstein, Phys. Rev. Lett. **98**, 158102 (2007).

[18] A. Sokolev, R. Goldstein, F. Feldchtein, and I. Aranson, Phys. Rev. E **80**, 031903 (2009).

[19] V. Bratanov, F. Jenko, and E. Frey, Proc. Nat. Acad. Sc. **112**, 15048 (2015).

[20] I. Golding, Y. Kozlovsky, I. Cohen, and E. Ben-Jacob, Physica A **260**, 510 (1998).

[21] A. Lacasta *et al.*, Phys. Rev. E **59**, 7036 (1999).

[22] S. Pigolotti *et al.*, Theoretical Population Biology **84**, 72 (2013).

[23] A. Brandenburg, N. E. L. Haugen, and N. Babkovskaia, Phys. Rev. E **83**, 016304 (2011).

[24] A. K. Bhattacharjee *et al.*, J. Chem. Phys. **142**, 224107 (2015).

[25] E. Ben-Jacob, I. Cohen, and D. Gutnick, Annu. Rev. Microbiol. **52**, 779 (1998).

[26] A. Czirok, E. Ben-Jacob, I. Cohen, and T. Vicsek, Phys. Rev. E **54**, 1791 (1996).

[27] E. Ben-Jacob, Contemporary Physics **38**, 205 (1997).

[28] E. Abraham, Nature **391**, 577 (1998).

[29] A. Martin, Prog. Oceanogr. **57**, 125 (2003).

[30] P. Perlekar, R. Benzi, D. Nelson, and F. Toschi, Phys. Rev. Lett. **105**, 144501 (2010).

[31] R. A. Simha and S. Ramaswamy, Phys. Rev. Lett. **89**, 058101 (2002).

[32] A. Maitra *et al.*, arXiv:1901.01069 .

[33] S. Ramaswamy, Annu. Rev. Condens. Matter Phys. **1**, 323 (2010).

[34] E. Bertin, M. Droz, and G. Gregoire, Phys. Rev. E. **74**, 0221011 (2006).

[35] S. Mishra, A. Baskaran, and M. C. Marchetti, Phys. Rev. E. **81**, 0619161 (2010).

[36] M. C. Marchetti *et al.*, Rev. Mod. Phys. **85**, 1143 (2013).

[37] J. Toner, Y. Tu, and S. Ramaswamy, Annals of Physics **318**, 170 (2014).

[38] X. Yang, D. Marenduzzo, and M. C. Marchetti, Phys. Rev. E **89**, 012711 (2014).

[39] A. Doostmohammadi, S. P. Thampi, and J. Yeomans, Arxiv:1601.04489v1 (2016).

[40] P. Perlekar, S. Ray, D. Mitra, and R. Pandit, Phys. Rev. Lett. **106**, 154501 (2011).

[41] M. T. Gastner, B. Oborny, D. Zimmermann, and G. Pruessner, The American Naturalist **174**, E23 (2009).

[42] B. Sapoval, M. Rosso, and J. F. Gouyet, J. Phys. Lett. **46**, L149–L156 (1985).

[43] A. Lemarchand, I. Nainville, and M. Mareschal, Europhysics Letters **36**, 227 (1996).

[44] G. K. Batchelor, J. Fluid Mech. **5**, 113 (1959).

[45] R. Kraichnan, Phys. Fluids **11**, 945 (1968).

Chapter 5

Conclusions

In this thesis we have revealed, through theoretical and computational studies, some remarkable phenomena in the hydrodynamics of polar active suspensions. A major motivation for the current study is to understand the roles of polarity (i.e. the ability to locomote) of the active particles and suspension inertia on the collective dynamics. We have used elementary analysis tools from the theory of hydrodynamic stability to identify threshold values of parameter combinations for which the system is stable to spontaneous distortions of the polar order parameter to angular perturbations. Our analytical theory, numerical simulations and statistical analyses have uncovered a novel flocking transition upon crossing one of the threshold values. Our linear stability analysis has further shown that when the concentration field is non-conserved and therefore slaved to the slow order parameter and hydrodynamic velocity fields, contractile suspensions are always unstable to pure splay distortions, whereas they are always linearly stable when the polar order parameter is divergenceless owing to incompressibility of the concentration. Another motivation of this thesis is to explore the effects of collective motion on the colony spreading in motile bacteria. We have shown that turbulent-like collective motion always enhances the propagation speed of colony growth front; the turbulent front structure is crumpled up and shows interesting statistical properties. We now individually explain the conclusions from each chapter and possible future directions.

5.1 Linear stability of polar active suspensions

We have shown that inertia drives a nonequilibrium phase transition in polar active suspensions, from a defect-disordered state to an ordered and statistically stable flock. We have done an exhaustive analysis of the stability of the uniaxial polar-ordered state in an active suspension, by taking into account the effects of suspension inertia and the leading order polar terms. We have shown that the governing control parameter is R which is the ratio of the inertial effects of self-propulsion to the scale of active stress as measured by the mean force-dipole density, and displays two thresholds R_1, R_2 obtained from linear stability analysis. This dramatic advance in the theory of flocks in fluid, whose instability [1] can now be seen as simply the Stokesian limit of a rich phase diagram, should stimulate a new wave of experiments on swimmers at nonzero Reynolds number. The design of controlled experimental systems for this purpose is therefore an important challenge. For $R < R_1$ we show a linear dependence of perturbation growth-rate on wavenumber q as $q \to 0$, which connects smoothly at higher wavenumbers to the classical Stokesian instability [1] of active suspensions. Linear instability persists for $R_1 < R < R_2$, which should cover most of the parameter space, because we expect $R_2 \gg R_1$, but the disturbance growth-rate at low wavenumbers is diffusive. For $R > R_2$ the polar order is linearly stable. We have shown that inertia cannot prevent the instability of *splay* distortions in *contractile* suspensions. We also highlight the distinct role of three dimensional perturbations in the destabilization of extensile suspensions. The above linear stability conclusions for extensile suspensions remain unchanged for a number-conserving system where the polar order field is incompressible. Incompressible contractile suspensions are however always linearly stable. An important next step, is thus to perform well-resolved numerical simulations on suspensions with an solenoidal polar order parameter field. A primary motive is to observe the effects of nonlinearities on the nonequilibrium steady states.

5.2 Turbulence in polar active suspensions

We have conducted a series of numerical simulations of the governing equations at various R, in order to understand the turbulence-like steady states corresponding to the various instabilites. The nonequilibrium steady state for $R < R_1$ is a turbulence dominated by hedgehog-defects. For $R_1 < R < R_2$ we find that despite the instability, the final stationary state is an ordered, though noisy, flock. We have characterized the phase transition from defect turbulence to phase turbulence by using standard tools from statistical mechanics, and find evidence for a continuous onset of order and a growing correlation length. This phase transition is exclusively for *extensile* suspensions. Important directions for the near future are (i) studies of finite-size scaling and long-wavelength order-parameter correlations for $R > R_1$ to establish the nature of the ordered phase and (ii) the construction of an effective stochastic theory for the long-wavelength modes, as carried out [2] for the Kuramoto-Sivashinsky equation. It is also worthwhile to investigate the defect dynamics in a three-dimensional setting, as has been done for two-dimensional nematic turbulence in [3, 4, 5, 6, 7]. This is a technically challenging job keeping in mind the various difficulties encountered while capturing the complex three-dimensional structure and dynamics of the various disinclinations. Another possible extension is to explore the possibilities of data-driven techniques in capturing the statistical properties of active turbulence. The reader is refered to [8] for a comprehensive study of such techniques applied for traditional fluid turbulence. Meanwhile, we look forward to tests of our theory in experiments and particle-based numerical simulations.

5.3 Role of active turbulence on the colony growth in motile bacteria

This study is motivated to investigate the effects of turbulent-like collective motion in motile bacteria on the morphology and dynamics of colony growth. We proposed two minimalistic models to study colony front propagation in dense colonies of motile bacteria performing turbulence like collective motion. We study two scenarios: (a) invasion of one colony over the other (model A) and (b) spreading of colony on a Petri dish (model B). We find that the presence of collective turbulence-like motion always enhances the front propagation speed. We highlight the similarities and the differences between the two models.In particular, model B allows for large-scale undulations which are absent in model A. We quantify the fractal structure of the front and show that the fractal dimension of the front around the stirring scales is $d_f = 7/4$. Finally, we also show that, for certain parameter values, the concentration fluc- tuations arising from bacterial turbulence are similar to those of passive scalar stirred by a random flow. Earlier experiments have investigated spreading of dense colonies of non-motile bacteria or of motile bacteria that form swarms. We hope that our simulations will stimulate new experimental studies on the spreading of colonies in this regime of bacterial turbulence.

Bibliography

[1] R. A. Simha and S. Ramaswamy, Phys. Rev. Lett. **89**, 058101 (2002).

[2] C. Jayaprakash, F. Hayot, and R. Pandit, Phys. Rev. Lett. **71**, 12 (1993).

[3] S. P. Thampi, R. Golestanian, and J. M. Yeomans, Phys. Rev. Lett. **111**, 118101 (2013).

[4] S. P. Thampi, R. Golestanian, and J. M. Yeomans, EPL (Europhysics Letters) **105**, 18001 (2014).

[5] S. P. Thampi, R. Golestanian, and J. M. Yeomans, Phil. Trans. R. Soc. A **372**, 20130366 (2014).

[6] L. Giomi, Phys. Rev. X **5**, 031003 (2015).

[7] L. Giomi *et al.*, Phil. Trans. R. Soc. A **372**, 20130365 (2014).

[8] K. Duraisamy, G. Iaccarino, and H. Xiao, Annu. Rev. Fluid Mech **51**, 357 (2019).